NANYANG TECHNOLOGICAL UNIVERSITY
SINGAPORE

PHOTOCATALYTIC CEMENTITIOUS MATERIAL FOR SELF-CLEANING AND ANTI-MICROBIAL APPLICATION

ABDUL HALIM HAMDANY

SCHOOL OF CIVIL AND ENVIRONMENTAL ENGINEERING

2018

PHOTOCATALYTIC CEMENTITIOUS MATERIAL FOR SELF-CLEANING AND ANTI-MICROBIAL APPLICATION

ABDUL HALIM HAMDANY

School of Civil and Environmental Engineering

A thesis submitted to the Nanyang Technological University in partial fulfilment of the requirements for the degree of Doctor of Philosophy

2018

Statement of Originality

I hereby certify that the work embodied in this thesis is the result of original research, is free of plagiarised materials, and has not been submitted for a higher degree to any other University or Institution.

. . . .19/08/2019 . . . .

Date

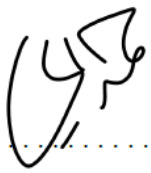

. . . . . .

Abdul Halim Hamdany

Supervisor Declaration Statement

I have reviewed the content and presentation style of this thesis and declare it is free of plagiarism and of sufficient grammatical clarity to be examined. To the best of my knowledge, the research and writing are those of the candidate except as acknowledged in the Author Attribution Statement. I confirm that the investigations were conducted in accord with the ethics policies and integrity standards of Nanyang Technological University and that the research data are presented honestly and without prejudice.

. . .19/08/2019 . . . .

Date Qian Shunzhi

Authorship Attribution Statement

Please select one of the following; *delete as appropriate:

*(A) This thesis **does not** contain any materials from papers published in peer-reviewed journals or from papers accepted at conferences in which I am listed as an author.

. . . .19/08/2019 . . . .

Date

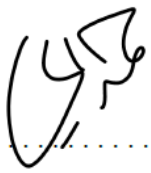

. . . . . .

Abdul Halim Hamdany

ACKNOWLEDGEMENTS

First of all, the author would like to express his greatest gratitude to his supervisor, Assistant Professor Qian Shunzhi, not only for his invaluable supervision and advice but also for sharing his experiences, encouragement and motivation throughout the journey of his PhD program.

The author owes his deepest gratitude to Dr Wei Li and Dr Ding Yuanzhao for their endless assistance and patience in guiding and helping the author on experimental design, chemical synthesis, microbiological related experiments, training for using equipment and report writing.

The author would also like to extend his sincere gratitude to Nanyang Technological University for the NTU research scholarship.

The author would like to thank all colleagues in his group (Weng Yiwei, Lu Bing, Liu Siyu, Dr Zhang Zhigang), Dr Martin Wijaya (CEE), Dr Ronny William (SPMS), and Dr Namyo Salim (CEE) for their comments and helpful discussion. The author also would like to thank all of PhD students in Prof Chen Yuan's group, Mr Cheng from CT Lab, Mr Phua from CT Lab, Ms Lim, Han Khiang from Environmental Lab and technicians that have not been mentioned for all the helps and friendship through these years.

Finally, the author would like to express his utmost gratitude to his family who has given continuous moral support and encouragement to the author.

TABLE OF CONTENTS

SUMMARY

In recent years, titanium dioxide (TiO_2) has become the most popular photocatalyst for environmental purification due to its capability to completely degrade a large variety of organic pollutants. However, an attempt to widen the scope of TiO_2 application is hindered due to wide bandgap of TiO_2 that limits the photoactivation of TiO_2 only under UV irradiation. In addition, previous work on environmental purification usually employed TiO_2 in the form of suspension system for water treatment. Although TiO_2 suspension system provides high surface area for photocatalytic reaction and can minimize mass transfer limitation, the widespread use of TiO_2 is restricted as suspension system has additional separation problems. This study therefore focused on (1) developing visible light activated TiO_2-based photocatalyst for enhanced degradation of organic pollutants under visible light irradiation and (2) immobilization of TiO_2 composite on cementitious materials as supporting media for self-cleaning and antimicrobial application.

The first part of this study was the synthesis of visible light activated graphene based TiO_2 composites by a one-step hydrothermal process. It was found that the combination of GO and TiO_2 exhibited a significant improvement in degradation of methylene blue compared to unmodified TiO_2. GO-TiO_2 displayed an obvious redshift in the absorption edge to higher wavelength region along with strong absorption in the visible light range. Under visible light irradiation, graphene acts as sensitizers to absorb photon. Following absorption, the excited graphene injects electrons into the conduction band of TiO_2; thus, the created electron-hole pairs become well-separated. These processes could significantly suppress the charge recombination and finally increase the photocatalytic activity. On the other hand, the enhancement of adsorption capability also contributes to the increase of photocatalytic activity. This finding is of considerable importance since it suggests that the simple synthesis process still provide remarkable improvement in the photocatalytic activity. In following research, the synthesized catalyst particles will be dispersed in cementitious materials to formulate functional cementitious coating. Finally, their photocatalytic performance in self-cleaning and anti-microbial application will be evaluated.

LIST OF TABLES

LIST OF FIGURES

Chapter 1. Introduction

1.1. Research background

In 2017, World Health Organization (WHO) reports that environmental risks – for example air pollution, contaminated water, lack of sanitation, and poor hygiene – take the lives of 1.7 million children under age 5 years (WHO, 2017). A polluted environment is a deadly one and hence reducing environmental risks could save millions of lives. Technological innovations may address such environmental problems and create an environmentally more sustainable future. Titanium dioxide (TiO_2) has emerged as an excellent photocatalyst for reducing environmental risks. Early works focused on treatment of polluted water using TiO_2 in powder suspension forms (Mills and Le Hunte, 1997, Simonsen, 2014). This method is efficient due to large surface area of the catalyst and the absence of mass transfer limitations. However, the widespread application is limited as the use of suspension has additional separation problems to be recycled from treated water after use, making it time consuming and cost ineffective (Herrmann et al., 1997, Pestana et al., 2015, Rachel et al., 2002).

In order to overcome these problems, many techniques have been proposed for immobilization of TiO_2 on solid support (Fujishima et al., 2007, Rachel et al., 2002). In recent years, there has been increasing interest in using cementitious materials as catalyst supporting media (Chen and Poon, 2009b). The main strategy is to exploit facade of the building in urban areas as catalyst supporting media. The cementitious materials used in building facade offer enormous surface area for photocatalytic reactions (Cassar, 2004). This strategy have a good potential in urban pollution control and at the same time maintain aesthetic of the buildings appearance (Krishnan et al., 2013, Jimenez-Relinque et al., 2017, Yang et al., 2017). Furthermore, incorporating TiO_2 photocatalyst into cementitious materials may be able to keep the cement-based surface sterile by inhibiting the growth of microorganisms through photocatalytic degradation (Guo et al., 2013, Singh et al., 2018). Thus, utilizing cement-based materials as catalyst supporting media potentially transform ordinary cementitious materials into environmentally friendlier products such as air-purifying

pavement, self-cleaning external wall, and anti-bacterial concrete as shown in Figure 1-1 .

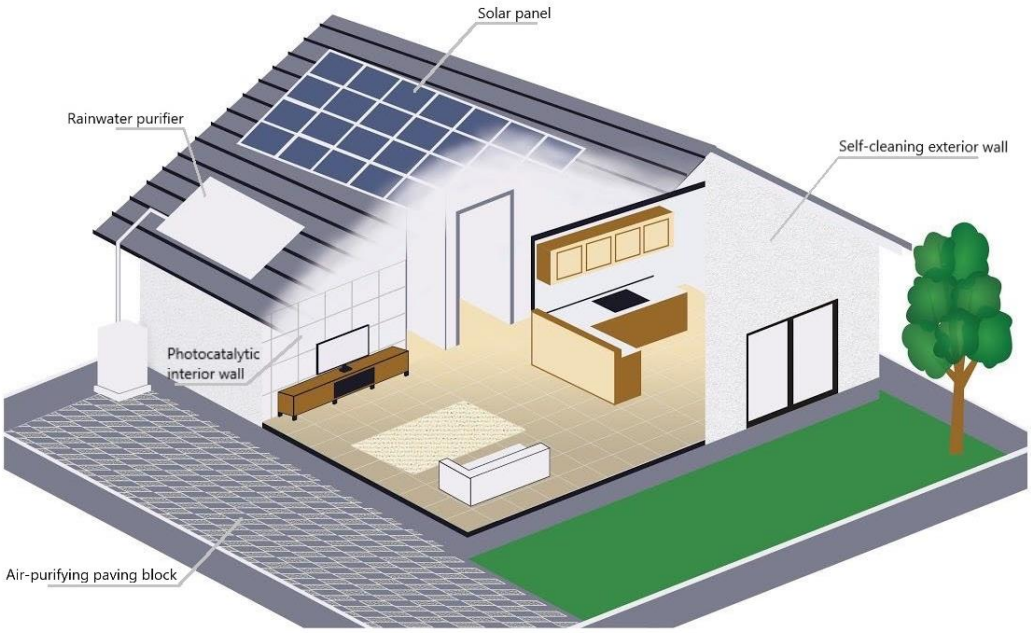

Figure 1-1: Multiple functions of TiO_2 based photocatalyst in cementitious materials (adapted from (Asaka Riken Co.)

1.2. Research motivation

As mentioned earlier, employing cement-based surface as catalyst supporting media greatly enhances its use in practical applications. Various functions such as self-cleaning, air purifying, and anti-bacteria effect potentially can be achieved by cementitious materials containing TiO_2 photocatalysts. Despite of being advantageous and beneficial, the TiO_2 based photocatalytic cementitious materials have several obstacles that hinder its full potential in practical applications. The major challenges include:

- The pristine TiO_2 absorption spectra are limited to the ultraviolet (UV) region due to its wide bandgaps (3.0~3.2 eV). Hence, TiO_2 photocatalyst mainly absorb UV photons for their photocatalysis activation. Whilst it can use natural solar – UV radiation as a promising energy source, there is only a small number of UV photons that can be used to carry out reactions at the TiO_2 surface. In terms of energy, sunlight at Earth's surface is around 52 to 55 percent infrared (700 – 10^6

nm), 42 to 43 percent visible (400 – 700 nm) and 3 to 5 percent ultraviolet (100 – 400 nm). Thus, there is a strong need to develop visible light active photocatalyst.

- Compared with air-purification and self-cleaning applications, little research has been carried out to study anti-bacterial effect of photocatalytic cementitious materials. For this reason, there is a current need in understanding the photocatalytic activity of TiO_2 based cementitious materials for anti-bacterial application. It is hypothesized that cementitious materials containing TiO_2 nanoparticles might affect bacterial initial attachment and growth. Hence, the presence of TiO_2 catalyst can potentially suppress biofilm formation on cement-based surface or keep the surface sterile.

- The efficient adsorption of the contaminants on the surface of the photocatalyst remains an issue yet is an important factor for achieving high degradation rate. This implies that a hybrid of TiO_2 and an adsorbent may exhibit better performance than that of pristine TiO_2. The ability of material to adsorb organic molecules onto its surface may greatly enhance the overall degradation process since it provides a shorter path for charge interaction.

1.3. Objectives

Photocatalytic cementitious material is one of the active research areas in concrete material engineering, and yet it holds the key to broaden the benefit of photocatalysis technologies in practical applications. To develop multifunctional photocatalysis cementitious materials which can be activated by visible light illumination, a clear understanding on the critical parameters and basic mechanisms affecting their photocatalytic performance must be achieved. To this end, a series of research program has been conducted. First, it started by fabricating the visible light activated TiO_2-based photocatalyst through coupling with graphene oxide. Subsequently, the synthesized catalyst particles were dispersed in cementitious materials to formulate functional cementitious coating. Finally, their photocatalytic performance in self-cleaning and anti-microbial was evaluated; further, the influence of some parameters, such as TiO_2 loading content, TiO_2 type, mixing procedure has been optimized. The scope of this research study is described below:

i. Effect of TiO_2 nanostructure on photocatalytic performance
   - To characterize commercial TiO_2 nanoparticles (optical properties and morphology)
   - To detect hydroxyl radical generation
   - To investigate the microstructure of cementitious materials
   - To study the wettability
   - To observe the antibacterial effect under UV light

ii. GO-TiO_2 nanocomposite
   - To synthesize GO-TiO_2 nanocomposite
   - To optimize synthesis conditions for this visible light active photocatalyst
   - To characterize the synthesized product and investigate the physiochemical properties
   - To examine the absorption capability, dye degradation performance, and antibacterial effect

iii. Visible light self-sterilization surface
   - To evaluate the antibacterial efficiency under visible light
   - To investigate the surface hydrophobicity
   - To examine the optical properties

iv. Lightweight ECC for antibacterial application
   - To do microscopic analysis
   - To evaluate mechanical performance
   - To examine the antibacterial activity

The new graphene-TiO_2 based photocatalysts will have much wider light absorption range and radically improved performances under low light intensity conditions. The role of the adsorbent is to improve the adsorption of contaminants, result in competitive process of interfacial charge transfer to and from the target organic molecules. Due to its high degree of microporosity, graphene has great specific surface area and will act as an adsorbent in the photocatalysis. The stability of graphene/TiO_2 is desired for safe usage and photocatalytic activity. It is therefore hypothesized that incorporating novel photocatalyst into cementitious material will contribute to wider application of photocatalyst in construction industry with following advantages:

- Enhanced visible light responsiveness;
- Strong adsorption of contaminants;
- Improved photocatalytic performance.

1.4. Methodology

By optimizing various elementary components and processes, the effective and efficient visible light responsive photocatalytic cementitious material will be obtained. The following research framework, as shown in Figure 1-2, constructs the major steps/research tasks to achieve the described objectives.

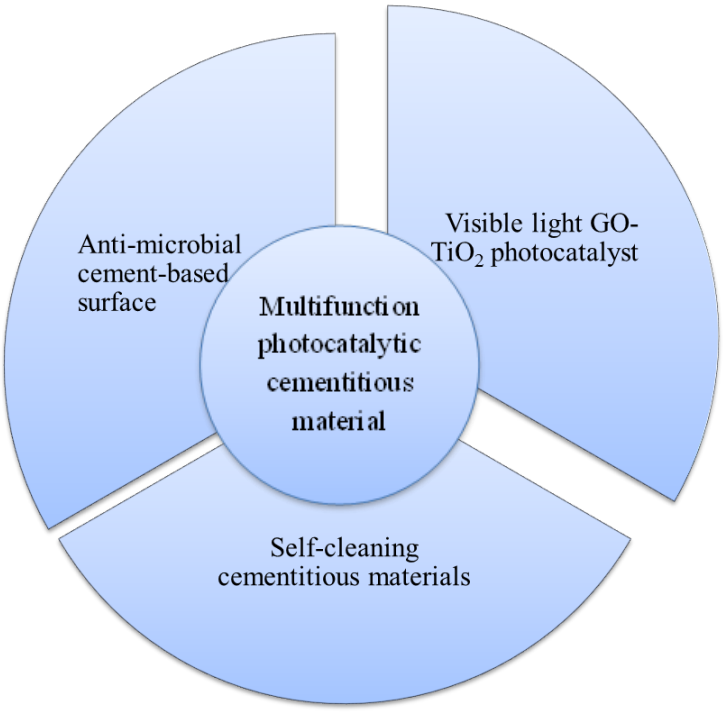

Figure 1-2 Research framework for multifunctional visible light active photocatalytic cementitious materials

In the first part, the effects of incorporating TiO_2 on microstructures of cementitious materials is investigated. In addition, self-cleaning activity and superhydrophilicity of TiO_2-based cementitious materials are assessed. For this reason, the photocatalytic activity of TiO_2 based cementitious materials for anti-bacterial application is also evaluated. It is hypothesized that cementitious materials containing TiO_2 nanoparticles might affect bacterial initial attachment and growth. Hence, the

presence of TiO_2 catalyst can potentially suppress biofilm formation on cement-based surface. Overall, this work can help establish a clear link between the nanostructure of TiO_2, microstructure of TiO_2-based cementitious composites and its photocatalytic performance.

Second part will focus an experimental study to synthesis the visible light activated graphene based TiO_2 nanoparticle composites will be carried out. Commercially available GO and TiO_2 powders from different sources will be used to simplify synthesis processes. This study consists of three consecutive steps. First step is a screening test. In this test, the photocatalytic performance of different commercial TiO_2 nanoparticles will be evaluated. The commercial TiO_2 product that performs the best will be selected for synthesis process. Secondly, the visible light activated graphene/TiO_2 nanoparticle will be synthesized by a simple mixing process. By tailoring the synthesis conditions, their photocatalytic activity under visible light illumination will be optimized. Lastly, the physical-chemical characterization of synthesized photocatalyst will be conducted. Optical property, specific surface area, morphology and surface of the photocatalyst will also be observed.

The third part aims to investigate the photocatalytic efficiency of GO-TiO_2 nanocomposites intermixing with cementitious materials. The factors governing the photocatalytic performance will also be evaluated. The critical parameters for dispersing the TiO_2 particle into cementitious coating will be studied. Furthermore, the procedure for good dispersion of the TiO_2 into cementitious materials in order to improve their photocatalytic performance will be developed. This section reports a study of antibacterial effect of cement-based surface mixed with TiO_2-based composite under visible light irradiation. Cement-based samples mixed with different TiO_2 type such as GO-P25, Krono, and P25 will be used for *Escherichia coli* inactivation.

The last part will incorporate TiO_2 photocatalyst into lightweight ECC materials. This work aims to develop the photocatalytic lightweight engineered cementitious composites (PL-ECC) for antibacterial application. The influence of addition of TiO_2 and different lightweight material on mechanical properties and antibacterial of *Escherichia coli* (*E. coli*) was investigated

1.5. Layout of report

This report comprises 7 chapters. Chapter 1 provides a brief introduction of the research background of photocatalytic cementitious materials and motivation of this study. From a review of current trend and research need on the photocatalytic cementitious materials, objectives and methodology of this work are established. In chapter 2, a literature review on photocatalytic cementitious materials is carried out, which covers related topics such as the basic mechanism of photocatalysis, the applications of photocatalytic cementitious materials and the influence of incorporating photocatalyst into cement mixture on the microstructure of cementitious materials. The results of this work are presented in chapters 3 to 6. Chapter 3 presents the effect of TiO_2 nanostructures on photocatalytic performances in the context of self-cleaning and anti-bacterial application. Graphene-based TiO_2 nanocomposites for enhanced visible light degradation of organic dye and antibacterial effect of *Escherichia coli* is evaluated in chapter 4. Chapter 5 investigates antibacterial potential of cementitious materials containing GO-TiO_2 composites for self-sterilization surface. In the chapter 6, the lightweight Engineered Cementitious Composite for antibacterial application is studied. Finally, in chapter 7, results of the current research work are summarized and the recommendation for future work is presented.

Chapter 2. Photocatalytic cementitious material for eco-efficient construction – a literature review

2.1. Overview

This chapter presents a systematic review of the cementitious composite materials containing TiO_2 photocatalyst. The review aims to present the key findings in photocatalytic cement-based composite materials and identify the areas in which future improvement is needed. This literature review will focus on the basic mechanism of photocatalysis, the applications of photocatalytic cementitious materials and the influence of incorporating photocatalyst into cementitious materials. The efficiency of photocatalytic cementitious materials and the current drawback will also be discussed.

2.2. Principles of photocatalysis

Photoinduced processes governed by light activated TiO_2 have been studied in various ways. Photovoltaic, photocatalysis and photoinduced super hydrophilicity are the examples of photoinduced processes on TiO_2. Although these processes could be utilized for many applications, these processes originate from similar mechanism as shown in Figure 2-1. Semiconductors can absorb the light with energy greater than their bandgap and generate an electron-hole pair. The generated electron-hole pairs can be utilized for creating electric power (photovoltaic process), promoting chemical reaction (photocatalysis process) or altering its surface properties (super-hydrophilicity) (Carp et al., 2004). The use of TiO_2 for facilitating the photocatalytic reaction has been started about decades ago and getting more importance nowadays indicated by huge number of publications (Cassar, 2004, Fujishima and Honda, 1972, Kubacka et al., 2014, Maury and De Belie, 2010, Murata et al., 1999). One of the most active areas in the development of photocatalysis technologies is their application for photodegradation of pollutants.

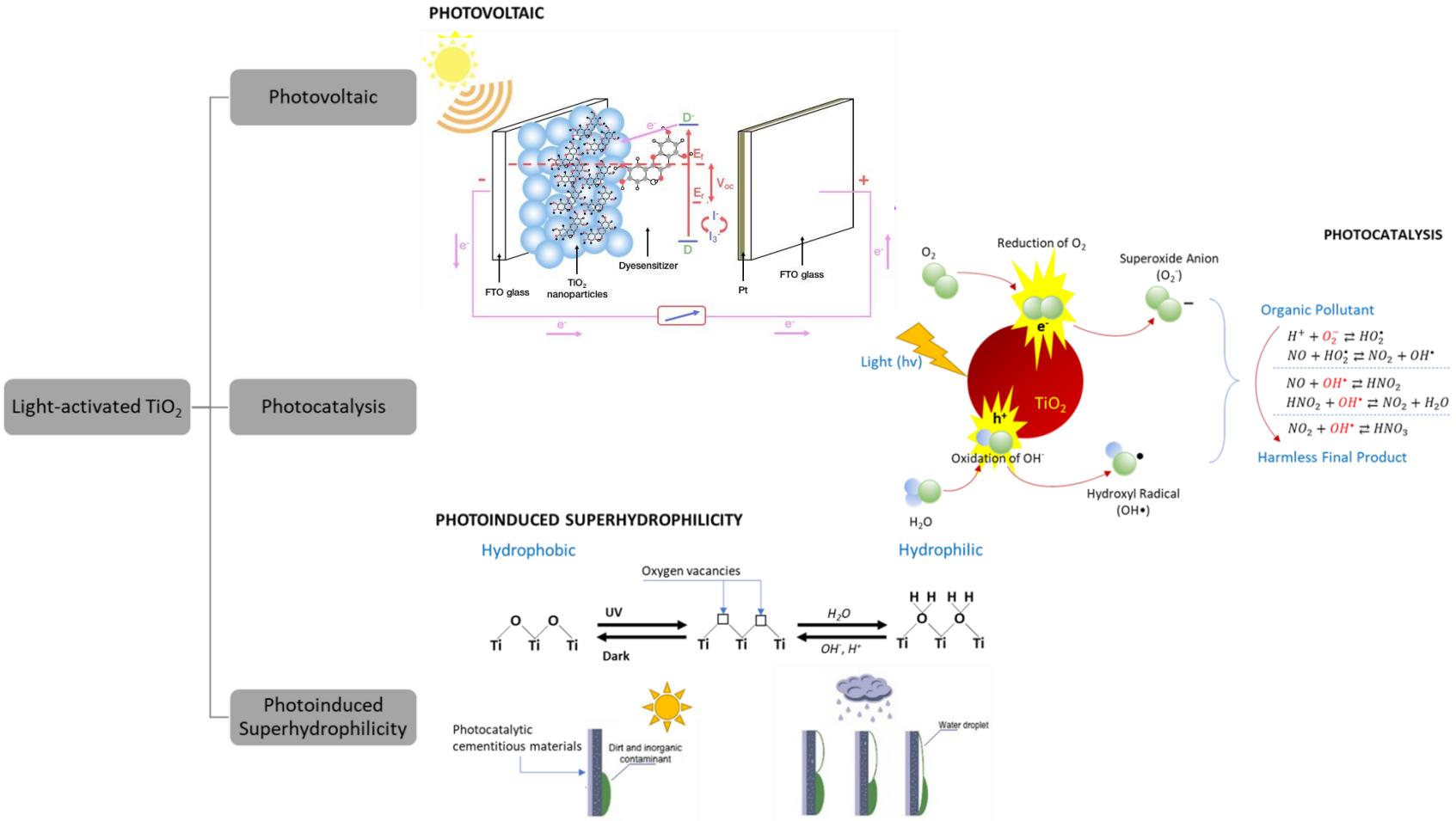

Figure 2-1: Applications of light-activated TiO_2 (Devahasdin et al., 2003, Fujishima et al., 2000, Maurya et al., 2016)

2.2.1. Semiconductor photocatalysis

In semiconductor, the valence band and the conduction band are separated by a bandgap ΔE, a region devoid of energy in a perfect crystal as shown in enlarge section of Figure 2-2. The highest energy band containing electrons is called the valence band (VB); the lowest empty band is called the conduction band (CB) (Miessler et al., 2014). The energy difference between the highest occupied band (the valence band) and the lowest unoccupied band (the conduction band) is called the bandgap, ΔE. By absorbing a photon energy equal to or greater than the band gap, ΔE, of the semiconductor, an electron is excited from the valence band into the conduction band, leaving behind a hole in the valence band (step 1), as shown in enlarged section of Figure 2-2 (Hoffmann et al., 1995). The created electron-hole pair has a sufficient lifetime, in the nanosecond regime, to undergo charge transfer to adsorbed species on the semiconductor surface (Linsebigler et al., 1995). In the absence of the adsorbate, the excited electrons at the conduction band and holes at the valence band can recombine (step 2) and dissipate the input energy as heat.

If suitable electron-hole scavengers or surface defect state is available to trap the electron or hole, recombination is prevented and subsequent redox transfer may occur (Hoffmann et al., 1995). Photogenerated holes can be utilized to oxidize substrates at the semiconductor surface, as illustrated in step 3 of Figure 2-2 (Kamat, 1993). The holes trapped at the TiO_2 surface can react with OH^- to generate OH• radicals. The generated OH• radicals and holes itself are a powerful oxidant. This powerful oxidant can degrade most of organic pollutant completely into harmless final product (e.g. CO_2 and H_2O), as shown in step 5. In addition, the photoexcited electrons can react with electron acceptors adsorbed on the semiconductor surface (step 4). The reduction power of electrons can induce the reduction of molecular oxygen (O_2) to form the superoxide anion (O_2^-). It has been confirmed that the superoxide is almost effective as holes and hydroxyl radicals in the chain reactions for breaking down the organic compounds.

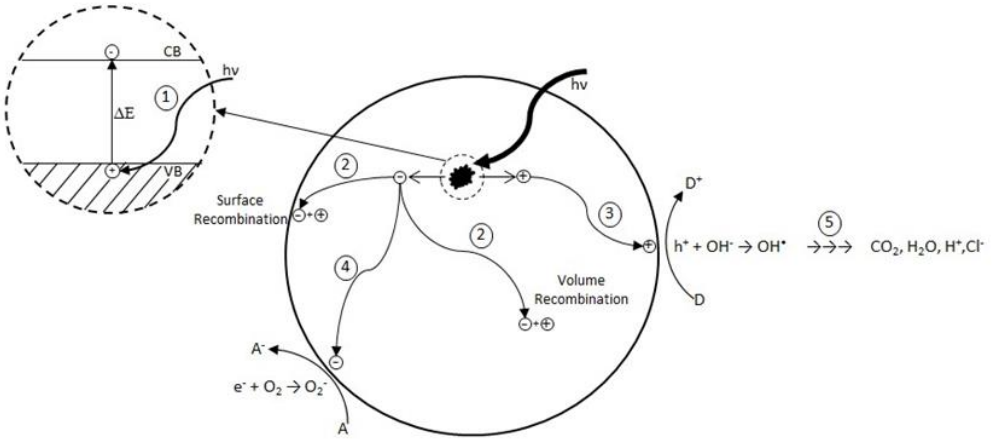

Figure 2-2: Primary steps in photocatalytic mechanisms (Hoffmann et al., 1995, Linsebigler et al., 1995)

Initiating an oxidation and reduction process at semiconductor surface is the principle of photodegradation (Kamat, 1993). Most organic photodegradation reactions utilize the oxidizing power of the holes either directly or indirectly (Hoffmann et al., 1995). During these processes, semiconductor remains intact and the charge transfer to the adsorbed species is continuous (Linsebigler et al., 1995). However, to prevent a build-up of charge, a reducible species should be provided to react with the electrons. In this system, photo-induced molecular transformations or reactions take place at the surface of a catalyst. The relevant photocatalytic processes may occur either at the air-solid-interface or at the liquid–solid interface. Therefore, if the species are pre-adsorbed on the surface, the electron transfer processes could be more efficient.

2.2.2. Bandgap and band-edge position

As the recombination is obviously destructive process for photocatalytic reaction, the efficiency of photocatalysis greatly relies on the competition between the electron transfer processes and recombination process (Mills and Le Hunte, 1997). The ability of semiconductor to undergo photoinduced electron transfer to the adsorbed species is governed by the band energy levels of the semiconductor and the redox potential of the adsorbed species (Linsebigler et al., 1995). The band energy levels of the semiconductor and redox potential of the adsorbed molecule influence the photocatalytic process by controlling the charge transfer process of such surface photochemical reactions (Kamat, 1993, Simonsen, 2014). For that reason, knowing

the band edge positions of semiconductors and redox potential of the adsorbate is useful for indicating the thermodynamic limitations for the photoreactions that can be carried out with the charge carriers (Hagfeldt and Gratzel, 1995).

The band energy positions of several semiconductors is illustrated in Figure 2-3 (Mills and Le Hunte, 1997). In order to photo-reduce a chemical/adsorbed species, the conduction band position of the semiconductor has to be positioned above the relevant reduction level of the chemical species. In order to photo-oxidize a chemical species, the valence band position of the semiconductor has to be positioned below the relevant oxidation level of the chemical species.

As illustrated in Figure 2-3, the bandgap of several semiconductor materials is in the range of 2.2 – 3.2 eV, corresponding to wavelength range from 564 to 388 nm. In photocatalysis, visible light photoactivation (>400 nm) is preferred by choosing low bandgap semiconductors. However, scientific investigations showed that the low bandgap semiconductors are subject to photocorrosion (oxidation of semiconductor) that results in loss of activity after period of time (Simonsen, 2014). In contrast, TiO_2 has been found to be chemically stable and resistant to photocorrosion and yet highly photoactive (Evans et al., 2013, Mills and Le Hunte, 1997).

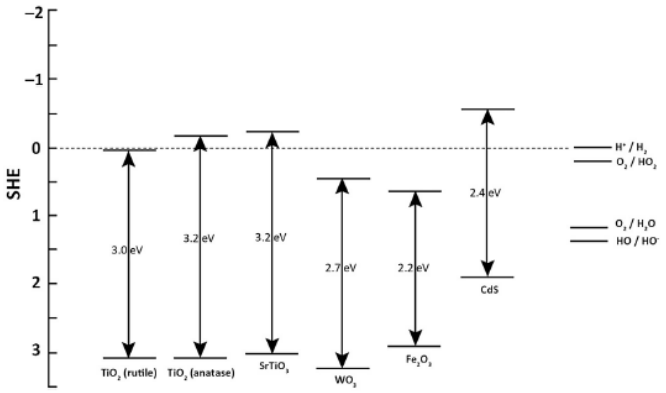

Figure 2-3: Valence and conductance band positions for various semiconductors and relevant redox couples at pH 0 (Simonsen, 2014)

2.2.3. TiO_2 based photocatalyst

TiO_2 naturally occurs in three different types of crystal structure: anatase, rutile, and brookite (Kirk et al., 1991). Two of them, anatase and rutile are commonly used in photocatalysis. As shown in Figure 2-3, the bandgap of anatase is 3.2 eV, while the bandgap energy for rutile is 3.0 eV, which is 0.2 eV narrower than anatase. Lower bandgap materials, rutile, should be preferred as it could absorb photon with smaller energy for photoactivation. However, in the literature, anatase shows higher photocatalytic activity than rutile under UV light irradiation. This is due to more negative conduction band position of anatase than that of rutile (Figure 2-3), resulting in more reactive species formed (Carp et al., 2004).

The scientific concept of TiO_2 photocatalysis was introduced by Fujishima and Honda (1972). They discovered the photocatalytic water splitting in photo-electrochemical cell. Using TiO_2 electrodes in a photo-electrochemical cell, water could be dissociated into its constituent parts, hydrogen and oxygen gases, under ultraviolet (UV) illumination. This discovery triggered much research in understanding the fundamental mechanism and in improving the efficiency of TiO_2 photocatalyst. In recent years, one of the most active areas in the development of photocatalysis technologies is their application for environmental clean-up. However, due to wide bandgap of the TiO_2 material, pristine TiO_2 photocatalyst can only be activated by UV irradiation (Agrios and Pichat, 2005, Fujishima et al., 2008, Linsebigler et al., 1995). Whilst it can use natural sunlight-UV irradiation, sunlight only contain a small amount of UV photon that can be used to carry out reactions at the TiO_2 surface. Therefore, one of the main challenges in improving the performance of TiO_2 photocatalyst is to extend their optical response from UV to visible region.

Improving the optical-response and photocatalytic performance of TiO_2 in the visible light region can be achieved by doping or sensitization as shown in Figure 2-4 (Xiaobo and Mao, 2007). Doping is a kind of bulk chemical modification to alter the chemical composition of TiO_2 but maintain the integrity of TiO_2 crystal structure. This technique substitutes the metal (titanium) or the non-metal (oxygen) component in order to alter the optical properties of TiO_2 nanomaterials. Figure 2-4(b) shows an example of metal doped, V-doped TiO_2 (Umebayashi et al., 2002). A red shift in the

band gap transition was induced by the metal doping of TiO_2. The bandgap of V-doped TiO_2 is lower than pristine TiO_2. It can be photoactivated by visible light irradiation. Visible light absorption of V-doped TiO_2 was due to the transition between valence band and V t_{2g} level.

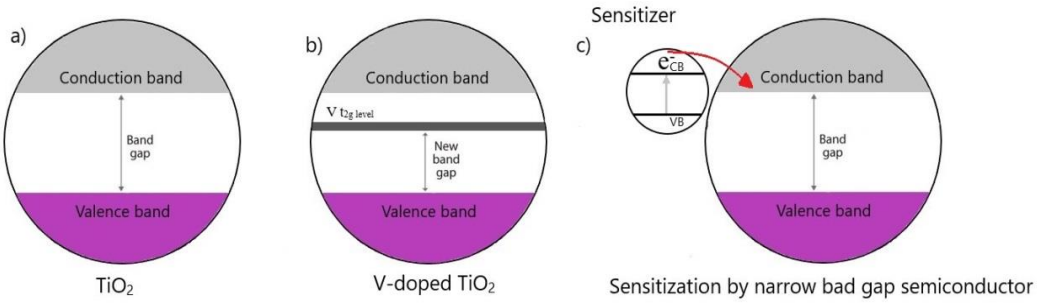

Figure 2-4: (a) Bandgap of pristine TiO_2, (b) Improving TiO_2 optical response by doping method to lower down the bandgap, and (c) Improving TiO_2 activity by sensitizer

An alternative technique is photosensitization, a photochemical process by which a chemical reaction is induced by energy transfer from the light-absorbing sensitizer (Braslavsky, 2007). As shown in Figure 2-4(c), charge transfer from the excited sensitizer to conduction band of TiO_2 is a key step in these processes. The match of energy difference between the oxidation potential of the excited sensitizer and conduction band of the TiO_2 acts as the driving force for the charge injection process (Vinodgopal et al., 1995). The sensitizer for TiO_2 materials can be any materials with lower bandgap, including semiconductors, metals, and organic dyes.

2.2.4. Graphene-based TiO_2 composite

As mentioned earlier, TiO_2 exhibits multiple advantages in its application for photocatalysis. However, the wide bandgaps of pristine TiO_2 hinder its full potential for many applications (Agrios and Pichat, 2005, Linsebigler et al., 1995). The bandgap of TiO_2 lies in the UV region which is only 3-5% of the sunlight energy. Therefore, one of the main challenges in improving the performance of TiO_2 photocatalyst is to extend their optical response from the UV to the visible region.

Surface modifications of TiO_2 with carbonaceous materials such as graphene oxide (GO) have received a great attention due to its excellent photocatalytic performance in the visible light (Cruz-Ortiz et al., 2017, Lettmann et al., 2001, Morales-Torres et

al., 2012, Rastogi and Vaish, 2016). Under visible light irradiation, graphene acts as sensitizers to absorb photon (Chen et al., 2010, Du et al., 2011). Following absorption, the excited graphene injects electrons into the conduction band of TiO_2. Subsequently, the electron is transferred to oxygen adsorbed on the semiconductor surface producing superoxide anion (O_2^-) which can facilitate the degradation of organic components. On the other hand, the enhancement of adsorption capacity also contributes to the increase of photocatalytic activity (Nguyen-Phan et al., 2011, Zhang et al., 2010a). In general, the adsorption capability could be enhanced by increasing GO content. However, the excessive GO content could hinder the adsorption of oxygen on the surface of active site. As a result, in the absence of oxygen, the injected electron at conduction band of TiO_2 could recombine, potentially leading to significant decrease of photocatalytic activity. Hence, it is suggested that there should be an optimum amount of GO in the GO-TiO_2 nanocomposite materials for the efficiency of photodegradation process (Liu et al., 2014, Pastrana-Martínez et al., 2012, Wang and Zhang, 2011).

There is different methods to prepare graphene-based TiO_2 composites, such as simple mixing and sonication (Guo et al., 2011, Zhang and Pan, 2011), sol-gel technique (Ahmadi et al., 2018, Li et al., 2013, Xia et al., 2018), hydrothermal (Li et al., 2014, Wang and Zhang, 2011, Zhang et al., 2010a), and solvothermal synthesis (Ding et al., 2011, Fan et al., 2011). As the simplest route, mixing and sonication is very common method for preparing the composites. However, due to its simplicity, it is not expected to have chemical bonding. As a result, the interaction between the particles in the composites is weak. Stronger bond generated from chemical interaction between GO and TiO_2 can be obtained by sol-gel method and hydrothermal/solvothermal synthesis. The sol-gel technique can be considered as the most widely used method for the preparation of GO-TiO_2 composites. However, it has a number of disadvantage such as quite substrate dependent, costly materials, and time consuming due to slow process of gel formation (Mackenzie, 1988). The last two techniques are the method of producing chemical compounds under controlled temperature and pressure. While hydrothermal usually use aqueous solution as precursor, the solvothermal use non-aqueous precursor. The need of expensive autoclaves is one of the main disadvantages of these methods.

2.3. Photocatalytic cementitious materials

In building industry, extensive work is underway to develop innovative construction material containing TiO_2 photocatalyst. Photocatalysis technologies make the production of construction materials with advanced functions such as self-cleaning, air purifying and self-sterilizing surface feasible (Zhu et al., 2004). Applications include self-cleaning building façade, photocatalytic concrete roads for depolluting of air and anti-bacterial tiles for hospital building interior (Fujishima and Zhang, 2006). Moreover, the applications of photocatalytic construction materials on buildings envelopes, road facilities and tunneling could be beneficial to alleviate the level of environmental pollution. Finally, it can further contribute to control the urban heat island effect in densely populated cities.

For example, the "smog-eating" facade of Manuel Gea Gonzáles Hospital in Mexico was made from white-cement containing TiO_2 photocatalyst to counteract the pollution from thousand automobiles per day. In Bergamo Italy, the photocatalytic concrete blocks has been used for renovating the heavy traffic street, claiming almost 40% of NOx abatement (Ohama and Van Gemert, 2011). In the case of indoor environment, the treatment of city tunnel wall in Rome with photocatalytic paint potentially reduce the NOx pollutants up to 20% under artificial UV light illumination (Guerrini, 2012). The current commercial technologies, such as TX Active® and TioCem® photocatalytic cement containing TiO_2 particles can effectively remove various pollutants, including NO_X, SO_X, NH_3, CO, and volatile organic compounds, by exposing the cement to outdoor UV light.

2.3.1. Air purifying cement-based materials

The application of photocatalytic cementitious materials for air purification purpose has recently received considerable attention because of its potential for controlling pollutant in the urban areas. Photocatalytic cementitious materials have the capability of destroying airborne pollutants emitted by automobiles such as nitrogen oxides (NOx) and volatile organic compounds (VOCs). Murata et al. (1999) have pioneered the development of photocatalytic cementitious materials for air purification. The works demonstrated that the cementitious materials containing TiO_2 particles can be

used as a measure for NOx pollution control. In 2013, German based company, Elegant Embellishment, developed customized photocatalytic building facade for Hospital Manuel Gea Gonzáles in Mexico. According to the studies, the facade is capable of decomposing the contaminant and neutralizing the pollution of 1000 cars per day.

The basic advantage of using photocatalytic cementitious materials as building facade or concrete pavement is the availability of sunlight and rainwater for photoactivation and regeneration (Murata et al., 1999). Furthermore, the systems installed close to emission source react with the pollutants under higher concentration. As observed by Strini et al. (2005) and Guo et al. (2017), the photocatalytic activities were linearly dependent on the concentration of air pollutant and irradiance. Therefore, the strategy to immobilize TiO_2 photocatalyst into cementitious materials is attractive for these air-purification systems (Lee et al., 2014, Martinez et al., 2014b, Pérez-Nicolás et al., 2015, Poon and Cheung, 2007, Ramirez et al., 2010, Sugrañez et al., 2013).

The mechanism of photocatalytic oxidation of NOx at steady state is illustrated in Figure 2-5 (Devahasdin et al., 2003). The generated $OH^{\bullet}$ radicals are presumed to be the key oxidant in the reactions. At the nitrogen dioxide (NO_2) stage, part of the gas may escape from the photocatalyst surface (Fujishima et al., 2008). Nevertheless, cement matrix possess an inherent ability to bind NO_2 (Lee et al., 2014). Therefore, use of cementitious materials as catalyst supporting media may effectively trap the NO_2 gas.

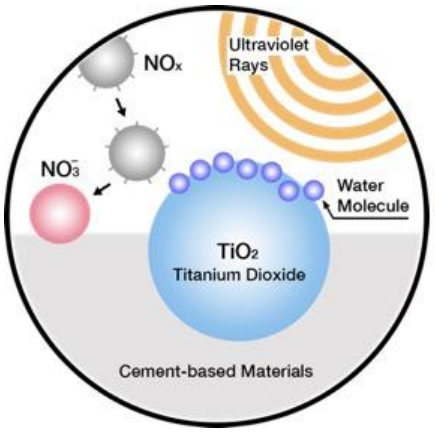

$$H_2O + h_{VB}^{+} \rightarrow OH^{\bullet} + H^{+}$$

$$NO + OH^{\bullet} \rightleftarrows HNO_2 + OH^{\bullet} \rightleftarrows NO_2 + H_2O$$

$$NO_2 + OH^{\bullet} \rightleftarrows HNO_3$$

Figure 2-5: Mechanism of photocatalytic oxidation of NOx at steady state under UV irradiation

To assess the air-purification performance of photocatalytic materials, there are five published ISO methods (ISO 22197 series) nowadays. According to that, nitric oxide, acetaldehyde, toluene, formaldehyde and methyl mercaptan are commonly used as model air pollutants. These pollutants are well recognized pollutants found in indoor and outside air (Mills et al., 2012). However, the current standard test methods do not consider the surface properties of cementitious materials such as porosity, heterogeneity, time-dependent variability, and environment-dependent variability (Jayapalan et al., 2015). Since the photocatalytic reactions take place at the surface of photocatalyst, the surface properties of cementitious materials are expected to influence their photocatalytic efficiencies.

For decomposition of gaseous pollutants, the photocatalytic reaction rate is influenced by numerous environmental-related parameters, such as temperature, humidity, wind speed, and light intensity. Light (wavelength and intensity) that can provide enough energy for photoactivation is one essential factor determining the reaction rate. The reaction rate increase with increasing light intensity, as shown in the following equation (Hoffmann et al., 1995):

$$r = k \Gamma I^{\alpha} \qquad (1)$$

where r is the rate of reaction, k is the rate constant, Γ is the catalyst concentration per unit area, and I is the light intensity. Humidity significantly influence the formation of active species since water molecular adsorbed on the surface can react with generated hole to form hydroxyl groups which in turn oxidizes pollutants (Ibusuki and Takeuchi, 1986). In the absence of water vapor, the photocatalytic reaction can seriously retarded. However, excessive water vapor on the surface could inhibits the reaction due to the competition between contaminant and water molecules for adsorption sites on the photocatalyst, thus reducing its performance (Obee and Hay, 1997). In the most of study, the reaction was operated at room temperature around 23±2 °C by using cooling system in the test chamber to eliminate heat generated from the lamp (Mills et al., 2012). The effect of increasing temperature is mainly to improve the photocatalytic reaction rate (Fu et al., 1996, Obee and Hay, 1997). In addition, the good contact between pollutants and active surface is

important for effective photocatalytic reaction. Hence, wind speed and its direction, street layout, and pollution source were another essential factors for photocatalytic reaction (Boonen et al., 2015, Boonen and Beeldens, 2013, Yu et al., 2018).

2.3.2. Self-cleaning cementitious materials

Prolonged exposure to various atmospheric pollutants also leads to the discoloration of cementitious materials. (Maury and De Belie, 2010, Ohama and Van Gemert, 2011). Due to this discoloration effect, the aesthetic of buildings, monuments, and other infrastructure exposed to outdoor environments are gradually lost with time. Besides the visible discoloration, the contamination of cement-based surfaces by airborne particles like algae and fungi can have destructive effect on structural integrity (Giannantonio et al., 2009, Gu et al., 1998). The key role of microorganism in the deterioration of cementitious materials has been linked to the generation of biogenic acids (i.e. sulfuric acid and nitrifying acid) (Parker, 1945). These substances cause dissolution of calcium hydroxide (CH) and other calcium containing minerals from concrete matrix. As a result, buildings should be repaired regularly to maintain a good appearance and prevent concrete deterioration.

Biocides treatments are common methods for preventing biodeterioration of cementitious materials. However, it has not been well accepted due to durability issues and its toxicity. Research found that the use of photocatalytic cementitious material was more effective for controlling biodeterioration processes than the conventional biocides (Fonseca et al., 2010). Early development of cementitious materials containing TiO_2 photocatalyst has been carried out primarily to enhance aesthetic durability of cementitious materials, especially those based on white cement (Maury and De Belie, 2010). Research work has successfully demonstrated that self-cleaning technique can be applied to various construction materials such as glass and cement-based materials like concrete and mortar (Cassar, 2004).

Apart from its function to decompose organic contaminant through photocatalysis process, TiO_2 has another unique photo-induced phenomenon to alter the wettability of its surface. The latter effect is often termed ‘super hydrophilicity’. The first phenomenon, photocatalysis process, has been studied extensively for decades while

the second one, super hydrophilicity, is more recently discovered. The ability of photocatalyst-based coating to improve the wettability upon illumination highly influences the efficiency of self-cleaning activity (Mills et al., 2012). In this case, after generation of electron-hole pairs, the photoexcited electrons could react with the Ti^{4+} cations to form the Ti^{3+}, as shown in Figure 2-6. Meanwhile, the holes could oxidize the O^{2-} anions to form the molecular oxygen. Then, the oxygen atoms are released, creating oxygen vacancies. The oxygen vacancies could be then occupied by water molecules, forming layer of chemisorbed OH groups which tend to make the surface hydrophilic (Fujishima et al., 2000). In the super-hydrophilic surface, the close contact between surface and adsorbed contaminant could be prevented (Guan, 2005). Hence, even though the number of incident photons may be insufficient to decompose the dirt and other impurities, the surface is maintained clean when water flow is supplied (Fujishima et al., 2008).

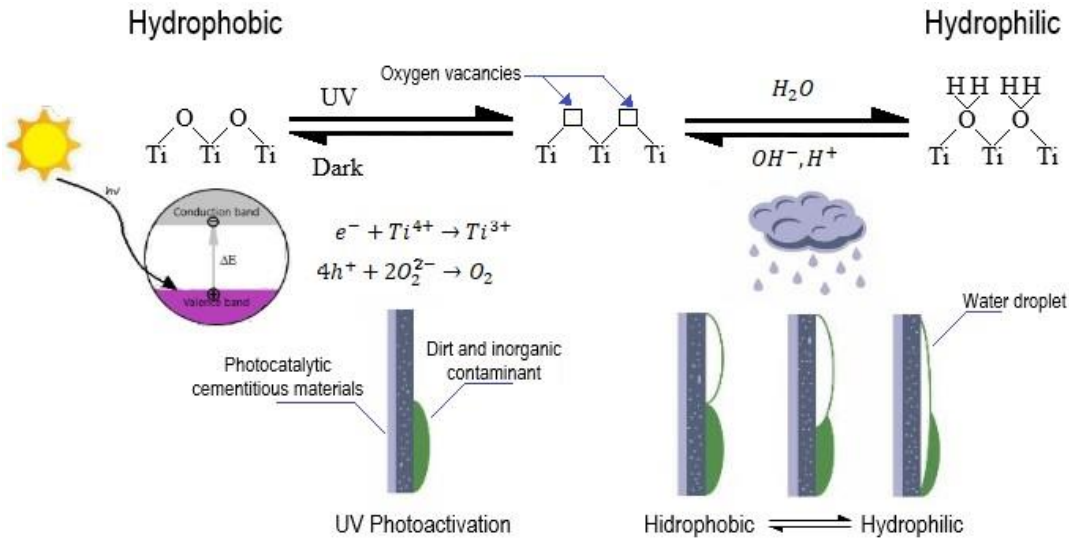

Figure 2-6: Mechanism of photoinduced hydrophilicity on TiO_2 cement surface under UV irradiation and rainfall (Fujishima et al., 2000)

The efficiencies of self-cleaning effect lies on the synergy between photocatalysis and photoinduced super hydrophilicity (Fujishima et al., 2000). International standard methods already exist nowadays to determine the efficiency of self-cleaning surface and further can be used by manufacturer to ensure the quality and reliability of their products (Banerjee et al., 2015). Measurement of water contact angle (ISO 27448: 2009) and organic dye decomposition (ISO 10678:2010) are commonly used test

method to evaluate self-cleaning activity of photocatalytic surface. The former method is used to measure the water contact angle under UV illumination. The latter method is used to evaluate the photocatalytic processes by degradation of the dye molecule in aqueous solution under UV illumination.

TiO_2 photocatalysis produce a more pronounced effect on smooth surface such as glass and ceramic tiles than in cementitious materials surface (Ohama and Van Gemert, 2011). The effect on cement-based surfaces is limited due to their relatively high roughness, porosity and permeability. Nevertheless, through the synergetic effect of photodecomposition and super hydrophilicity, self-cleaning effect of photocatalytic cementitious materials is still promising. Therefore, the best practice of self-cleaning cementitious materials is for outdoor application due to the availability of sunlight and rainfall to maintain the self-cleaning effect continuously (Fujishima and Zhang, 2006, Kazuhito et al., 2005, Murata et al., 1999).

2.3.3. Self-sterilizing cement-based coated surfaces

The researchers have shown that photocatalysis reaction induced by light-activated TiO_2 is significantly effective in destructing the pathogenic microorganisms (Carre et al., 2014, Foster et al., 2011, Huang et al., 2000, Kiwi and Nadtochenko, 2005, Kubacka et al., 2014). *Escherichia coli*, *Lactobacillus acidophilus*, *Salmonella enteritis*, and *Clostridium perfringens* are range of test bacteria that have been investigated (Mills et al., 2012). The basic photocatalytic disinfection mechanism is mainly caused by an initial attack on the bacteria cell wall. Carre et al. (2014) revealed dual effects of superoxide anions (O_2^-) on lipid peroxidation that could enhance membrane fluidity and disrupt cell integrity. After eliminating the cell wall protection, the oxidative damage takes place on the plasma membrane of the bacteria, resulting in subsequent rapid death of cell. It was also found that, the cell exposed to TiO_2-UV treatment exhibits rapid cell inactivation at the signalling stages, which affects a restricted set of respiratory components (Kubacka et al., 2014).

Furthermore, the cell exposed to TiO_2-UV treatment exhibit rapid cell inactivation at the signalling stages, which affects a restricted set of respiratory components (Kubacka et al., 2014). It was possible that superoxide anions (O_2^-) might inhibit the

bacterial respiration process. For example, *Shewanella oneidensis* used the cytochromes MtrA, MtrB, MtrC and OmcA for electron transfer (Lower et al., 2009, Reardon et al., 2010, Wang et al., 2008). By the cytochromes, the bacteria were able to transfer the electron from intracellular region to extracellular space and have the redox reaction in the outer membrane or extracellular space, known as one of the important steps in bacteria (Jani et al., 2010). However, the superoxide anions ($O2^-$) were highly active, which might further affect the cytochromes stability and/or inhibit the normal redox process in bacterial respiration.

Bacteria were ubiquitous and they formed the biofilms after attaching on the cementitious materials (Flemming and Wingender, 2010). Previous studies have reported that the bacteria in the biofilm stage was more tolerant in the harsh environment (e.g. temperature fluctuation, antimicrobial agents) compared to the bacteria in the free-swimming stage. The bacteria and the biofilms might further affect human body and cause serious infection (Wagner and Iglewski, 2008, Yang et al., 2008). As a result, the anti-bacterial and anti-biofilm techniques were strongly needed in the cementitious materials. One of the emerging techniques was immobilization of TiO_2 in cementitious materials.

Immobilization of TiO_2 into cementitious materials has led to the development of versatile self-sterilizing cement-based surface that are useful for a wide variety of application. Self-sterilizing surface is particularly useful for construction of microbiologically sensitive place such as healthcare facilities and manufacturing facilities that produce microbiologically sensitive product. Previous study demonstrated that the photocatalytic cementitious materials could deactivate the *Escherichia coli* under UV irradiation within relatively short time (Giannantonio et al., 2009, Guo et al., 2013, Maury-Ramirez et al., 2013, Sikora et al., 2017, Singh et al., 2018). The biocidal capabilities of photocatalytic cement-based surface can induce microbial death and maintain the surface sterile. However, compared with air-purification and self-cleaning applications, little research has been carried out to investigate the antimicrobial effect of photocatalytic cementitious materials.

2.4. Discussion

2.4.1. Influence of using cementitious materials as catalyst supporting media on photocatalytic activity

As discussed earlier, the immobilization of TiO_2 on solid support such as cementitious materials greatly enhance its use in practical applications. However, it may reduce the photocatalytic efficiency due to the reduction of active surface and mass-transfer limitation. For TiO_2 immobilized systems, the accessible active-surface-area is a key element affecting the efficiency of photocatalytic activity. The accessible active-surface-area depends on the amount of TiO_2 in the hardened cement and the pore structure of cementitious materials. The factors controlling the accessible active-surface-area should be well understood before developing efficient photocatalytic process.

2.4.1.1. TiO_2 dispersion

The effectiveness of TiO_2 dispersion in cement media has a great influence on the photocatalytic performance of the resulting products. In conventional dispersion method, the TiO_2 particles were usually mixed with cementitious materials as dry powders by mechanical stirring before adding water. This mixing procedure was inclined to strong aggregation of TiO_2 particles in cement matrix, resulting in the decrease of the available active-surface-area in hardened cement (Folli et al., 2010). It was found that the hydrodynamic size of TiO_2 nanoparticle dispersed in aqueous solution tend to be larger than the primary particle size. Jiang et al. (2009) shows that probe-sonication works very well to significantly decrease the hydrodynamic size. In the next studies, Yousefi et al. (2013) as well as Krishnan et al. (2013) adopted wet-mixing procedure in order to suppress the aggregation of TiO_2 particles in cement matrix. In wet-mixing procedure, the TiO_2 particles were first mixed with water using probe ultrasonication before adding other materials. The use of ultra-sonication leads to uniform distribution of the nanoparticles and enhance the photocatalytic performance.

Regardless of the mixing methods, mixing TiO_2 particles with cementitious materials may reduce the active surface area due to the encapsulation of photocatalyst particles

by hydration products. Consequently, the photocatalytic activity is seriously limited and sensitive to ageing processes (Lackhoff et al., 2003). It was observed that dispersion of TiO_2 into coatings can be considered as an attractive alternative since the coating are in direct contact with pollutant and photons and less affected by cement hydration (Krishnan et al., 2013, Ramirez et al., 2010). However, the coating method might be susceptible to harsh weathering processes. Hence, the selection of suitable dispersion method should be adjusted to their intended applications to maximize the active surface area.

2.4.1.2. Pore structure

The researchers have shown that there is a direct relationship between photocatalytic performance and microstructures of cementitious materials (Lucas et al., 2013, Sugrañez et al., 2013). Microstructure in this context is defined in terms of pore structure (i.e. pore volume, pore size distribution, interconnectivity). The pore structure of cementitious material is one of the important factors to determine the surface area accessible for photocatalytic process. Generally, increasing total porosity could enhance the photocatalytic performance due to the increase of accessible active-surface-area. Besides, high porosity is advantageous to the TiO_2 particles retention after weathering process (Ramirez et al., 2010).

The structure of porosity also determines the rates of intrusion, the rate of pollutant accessing the mass of concrete. Insufficient porosity for adsorption of contaminant may lead to negligible effect of photocatalytic activity (Rachel et al., 2002). Hence, high porosity is favorable for pollutant accessing the internal structure of concrete (Poon and Cheung, 2007). However, in some study, high porosity caused the decrease of photoactivity because the rate of contamination is higher than the rate of decontamination (Gallus et al., 2015, Maury-Ramirez et al., 2013).

In the long term, the microstructure of cementitious materials changes with age due to surface carbonation. Carbonation of cementitious materials is the irreversible chemical reaction which transforms hydration product, $Ca(OH)_2$, to $CaCO_3$ by the presence of CO_2 in the pore water. Since $CaCO_3$ has different crystal structure and higher molar volume, carbonation increases the solid volume of cement paste

(Arandigoyen et al., 2006). Thus, it decreases the total porosity and shifts the pore size distribution towards smaller diameters. It was found that carbonation also cause a little reduction of the specific surface area (Johannesson and Utgenannt, 2001). The decrease of porosity and specific surface area could result in the reduction of accessible active-surface-area. Furthermore, Dias (2000) investigated that carbonation alters the sorptivity of concrete to a lower degree, weakening the adsorption of contaminant. Hence, the change of microstructure by surface carbonation may lead to the reduction of photocatalytic performance (Jun and Chi-Sun, 2009, Krishnan et al., 2013, Lackhoff et al., 2003).

2.4.2. Effect of incorporating TiO_2 into cement-based materials

Understanding the effect of TiO_2 incorporation on the behavior of cementitious composites is of great importance especially for possible construction applications. In the fresh state of the mix, reduction of workability is the main effect induced by adding TiO_2 materials (Torgal, 2013). Due to their nanometre size, the mix undergoes extensive alteration in the rheological behavior. This change is very pronounced and must be considered to achieve a targeted workability during construction processes. On the other hand, several researchers have studied the influence produced by the presence of TiO_2 fine particles on the cement hydration and the concrete strength (Bo Yeon and Kurtis, 2010, Gutteridge and Dalziel, 1990, Jun and Chi-Sun, 2009, Lackhoff et al., 2003, Pérez-Nicolás et al., 2015). The addition of TiO_2 fine particles generally increases the strength of concrete, which is attributed to the filling effect. However, there is no general consensus on the effect of TiO_2 fine particles on hydration kinetics. Hence, the impact of TiO_2 on cement hydration kinetics is still a subject of debate.

Early research work on this effect found that the presence of fine particle enhance the degree of hydration of the major cement phase (Gutteridge and Dalziel, 1990). Further studies by Lackhoff et al. (2003) as well as Bo Yeon and Kurtis (2010) confirms that there were specific interactions between the cement matrix and the photocatalysts due to pozzolanic activity of the semiconductors. The addition of TiO_2 particle which has high surface area provides additional nucleation sites for hydration

product formation. TiO_2 may react with calcium hydroxide (CH) to form a product like calcium silicate hydrates (C-S-H).

In contrast to research discussed above, Jun and Chi-Sun (2009) observed that the incorporation of TiO_2 into cement matrices did not influence the amount of hydration product. Their results indicated that TiO_2 was inert and chemically stable in the cement hydration reaction. Their findings suggest that the TiO_2 particles act only as fillers and did not influence the amount of hydration product. Recent study by Pérez-Nicolás et al. (2015) found that the addition of TiO_2 into iron-rich dark-cement gave rise to a heterogeneous matrix, as a result of the TiO_2-ferrite interaction. On the other hand, it is suggested that the predominant mechanism of incorporating TiO_2 into iron-lean white-cement is physical entrapment, without significant chemical interaction. In this latter case, most TiO_2 in white-cement matrix remained unaltered and almost fully available for the photocatalytic processes.

2.4.3. Photocatalyst deactivation

The photocatalyst lifespan is obviously important point for economic reason, as it sets optimum run times between catalyst regeneration and replacement (Sauer and Ollis, 1996). Performance degradation over time, called photocatalyst deactivation, is among the most severe practical problems. The generation of intermediates is one of the main causes of photocatalytic deactivation. An incomplete process of photocatalytic oxidation produces intermediates that are retained on the surface. Intermediate products can occupy the active sites of the catalyst, leading to number of problems that include catalyst deactivation. Further catalyst deactivation (and regeneration) studies in photocatalysis are necessary to obtain better understanding on these processes and establish the process economics of this technology.

Research work has successfully demonstrated that using more active photocatalyst could retard the deactivation process (Méndez-Román and Cardona-Martinez, 1998). Choosing the correct photocatalyst for each specific application during manufacturing phase determine the overall durability of the final product in the usage stage. For example, visible light activated photocatalysts will have much wider light absorption range and radically improved performances under low light intensity

conditions. Improving performance could, at the same time, delay the deactivation processes.

In the usage phase, controlling relative humidity is of great importance for the efficiency of photocatalytic reaction. Water vapor plays a significant role in the formation of active species (Ibusuki and Takeuchi, 1986). Water molecular adsorbed on the photocatalyst will react with the hole and generate some hydroxyl groups which in turn oxidizes pollutants. Ibusuki and Takeuchi (1986) found no conversion in the absence of water vapor and the photocatalytic reaction rate increased linearly with increasing relative humidity over the range 0-60%, as shown in Figure 2-7(a). However, excessive water vapor on the catalyst surface inhibits the photocatalytic reaction because the presence of water vapor competes with contaminants for adsorption sites on the photocatalyst, thus reducing the performance (Obee and Hay, 1997). This is called "competitive adsorption" between water vapor and contaminants.

Although the deactivation mechanism of photocatalyst is not clear, it can be supposed that it is due to the partial saturation of active sites for adsorption, on the photocatalyst surface, with intermediate products. Akhter et al. (2015) demonstrated that placing the used catalyst in an oven at 30° C and relative humidity of approximately 40% for 12 h to evaporate the adsorbed species could recovered more than 90% of the catalysts, as shown in Figure 2-7(b). The works found that most of the adsorbed species were only adsorbed physically.

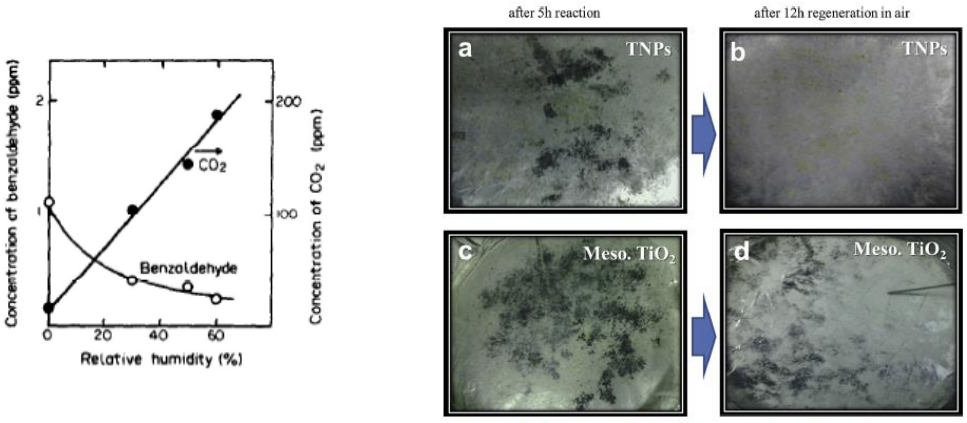

Figure 2-7: (a) Effect of relative humidity (Ibusuki and Takeuchi, 1986) and (b) Effect of heat treatment (Akhter et al., 2015)

2.5. Summary

In this study, a systematic review of the cementitious composite materials containing TiO_2 photocatalyst was presented. The immobilization of TiO_2 on solid support such as cementitious materials greatly enhances its use in practical applications. Photocatalytic cementitious materials with diverse functions, such as air-purifying, self-cleaning, and anti-bacteria properties could be achieved. In photocatalytic cementitious materials, the key element affecting the photocatalytic performance is the accessible active-surface-area. However, microstructure of cementitious materials changes with age due to hydration and surface carbonation. Hence, surface-area reduction and mass transfer limitation become the main drawback of incorporating TiO_2 on cementitious materials. Further study on evaluating anti-bacterial effect of photocatalytic cementitious materials and using visible-light-activated-TiO_2 in cementitious materials is needed as up to this stage little evidence is available on such applications.

The efficiency of antibacterial and self-cleaning application is influenced by a variety of factors, such as crystal structure, surface area, nanoparticles size distribution, porosity, relative humidity and dispersion method in cement matrix. By optimizing various factors, the efficient antibacterial and self-cleaning cement-based composites can be obtained. For example, during the synthesis process of GO-P25, the hydrothermal conditions should be optimized to control the particle size, dispersion and doping level in GO. The procedure for good dispersion of the TiO_2 into cementitious materials in order to improve their photocatalytic performance need to be investigated. Table 2-1summarize the major step and their specific target in order to achieved visible light activated antibacterial and self-cleaning functionalities in the TiO_2-based cement composites.

Table 2-1: The major step and their specific target in order to achieved antibacterial and self-cleaning functionalities in the TiO_2-based cement composites.

Processes	**Target**
Synthesis visible light activated TiO_2 nanoparticle	- Enhanced visible light responsiveness; - Strong adsorption of contaminants.
Dispersion of nanocomposite in cement matrix	- Optimized the mixing/dispersion method; - Prevent serious agglomeration of nanoparticle during mixing process.
Performance evaluation	- Efficient antibacterial and self-cleaning under lowlight condition; - Durable and stable

Chapter 3. TiO_2-based cementitious composites for self-cleaning application: Effect of TiO_2 nanostructures on photocatalytic performances

3.1. Overview

Exterior of building envelopes exposed to outdoor environments is degraded over time. The most obvious characteristic of degradation is visible discoloration. Building exterior gradually shows green, red, or black stains on the surface (Martinez et al., 2014a, Maury-Ramirez et al., 2013), for example black and green stains shown in Figure 3-1(a). Such degradation of concrete facade is mainly due to accumulation of particulate matters or colonization of microorganisms. Particulate airborne pollution which is the product of incomplete combustion of fuels engine contain sulphur-based gases (Association, 2002). It can combine with moisture to form sulfuric acid. Moreover, the contamination of cement-based surfaces by microorganism has been linked to the generation of biogenic acids (i.e. sulfuric acid and nitrifying acid). These acid substances cause dissolution of calcium hydroxide (CH) and other calcium-containing minerals from concrete matrix (Gu et al., 1998, Parker, 1945). Finally, it may have a destructive effect on structural integrity. As a result, buildings should be repaired regularly to maintain a good appearance and prevent concrete deterioration.

Pressure-washing and soft-washing are common methods for cleaning the exterior building to remove dirt, algae, mildew, and other contaminants. Pressure washing use high-pressure water to clean (Figure 3-1(b)), whereas soft-washing use low-pressure water combined with specialized chemicals (biocides treatment). However, both methods do not provide a long-term protection. In addition, pressure washing may damage the materials, while soft washing may be not well accepted due to toxic issues. Research found that the use of photocatalytic cementitious material (Figure 3-1(c)) was more effective for controlling deterioration processes than the conventional methods aforementioned (Fonseca et al., 2010).

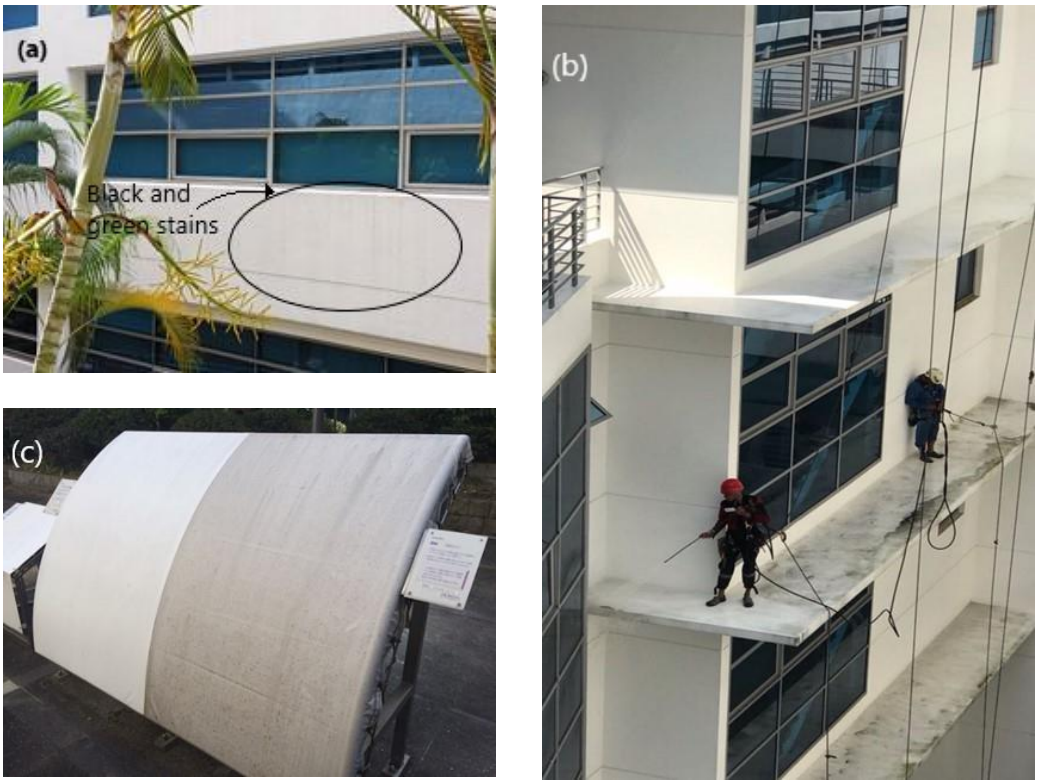

Figure 3-1: (a) Black and green stains appearance in exterior building, (b) pressure washing process and (c) comparison of photocatalytic surface (left) and conventional surface (right) (Green Millennium, 2018)

Immobilization of TiO_2 into cementitious materials has led to the development of versatile cement-based surface that are useful for a wide variety of application. For example, TiO_2-based cement composite can be applied as exterior building for self-cleaning surfaces, urban pollution control, and anti-microbial surface (Zhu et al., 2004, Pérez-Nicolás et al., 2015, Singh et al., 2018, Yang et al., 2017, Sikora et al., 2017). The ability of photocatalyst-based materials to improve the wettability upon illumination highly influences the efficiency of self-cleaning activity (Mills et al., 2012). Super-hydrophilic surface of TiO_2-based cement composite can utilize rainwater to wash away a dirt and organic contaminants, maintaining a clean surface. TiO_2 treatment can also have capabilities to deactivate bacteria under UV irradiation within relatively short time, leading to microbial death and maintaining the surface sterile (Giannantonio et al., 2009, Guo et al., 2013, Maury-Ramirez et al., 2013, Sikora et al., 2017, Singh et al., 2018). However, compared with air-purification and self-cleaning applications, little research has been carried out to investigate the antimicrobial effect of photocatalytic cementitious materials.

It is also essential to study the contribution of radicals in the photocatalytic reaction. After photoexcitation, the electron-hole pairs could react with oxygen and water molecules to produce oxidation radicals (Hoffmann et al., 1995, Linsebigler et al., 1995). One of radicals is hydroxyl radicals which is a highly important species in photocatalysis, being often assigned as the reactive oxidation species responsible for photocatalytic efficiency (Hirakawa and Nosaka, 2002, Xiang et al., 2011, Xiao and Ouyang, 2009). This work presents an experimental study to evaluate the hydroxyl radical production by various TiO_2 with respect to the TiO_2 surface area, morphology, optical properties, and band energy gap. Nano and microstructure of TiO_2 composite might influence the radical formation during photocatalytic reaction and as a result affecting over-all performance.

Overall, this work can help establish a clear link between the nanostructure of TiO_2, microstructure of TiO_2-based cementitious composites and its photocatalytic performance. It is hypothesized that cementitious materials containing TiO_2 nanoparticles might affect bacterial initial attachment and growth. Hence, the presence of TiO_2 catalyst can potentially suppress biofilm formation on cement-based surface. In addition, self-cleaning activity and superhydrophilicity of TiO_2-based cementitious materials are assessed.

3.2. Methodology

3.2.1. Materials

In this study, white cement (Aalborg Portland Malaysia) was used as the cementitious materials. Rhodamine B (Sigma-Aldrich, Singapore) was selected to mimic particulate air pollution. *Escherichia coli* K-12 (DSM-498) was used as the model bacterium for evaluating anti-bacterial activity. Three type of commercial titanium dioxide catalysts were used: Aeroxide P25 (Evonik, Germany), TiO_2-anatase and TiO_2-rutile (Shijiazhuang Kailing, China). Physical and chemical properties of the TiO_2 are summarized in Table 3-1. Unless otherwise stated, the experiments were performed at room temperature (23±2 °C) and 80% humidity.

Table 3-1 Characteristics of commercial TiO_2

Characteristic	Aeroxide P25	TiO_2-Anatase	TiO_2-rutile
Crystalline phases (%)[a]	80 anatase 20 rutile	99 anatase	99 rutile
Specific surface area (m^2/g)[b]	46.892	8.004	10.194
Average primary particle size (nm)[c]	20-40	≥ 100	≥ 100
TiO_2 content - purity (wt. %)[d]	≥ 99.5	98	94

[a] investigated by XRD analysis
[b] measured by N_2 adsorption test (BET theory)
[c] estimated by SEM images
[d] according to manufacturer specifications

3.2.2. Sample preparation

The mix proportions used to prepare the sample were listed in Table 3-2. Three different TiO_2 materials were intermixed into cementitious materials with 5% loading. The loading for Aeroxide P25 was also varied - 3%, 5% and 10% by weight of the cementitious materials. The water to cement ratio was kept constant at 0.5 for all the mixtures. The mixture without any TiO_2 was prepared as a control specimen. For sample preparation, cementitious material and TiO_2 were manually mixed as dry powders for 5 min until evenly distributed. Distilled water was then added and manually mixed for another 10 min. The mortar specimens were casted in 60 mm diameter and 15 mm thickness moulds. Three cement discs were prepared for each set. The prepared samples were cured for 28 days at room conditions before tests.

Table 3-2 Mix proportion (on weight basis of cement)

Mix No	TiO_2 type	TiO_2 loading	w/c
1	-	-	0.5
2	TiO_2-anatase	5%	
3	TiO_2-rutile	5%	
4	Aeroxide P25	5%	
5	Aeroxide P25	3%	
6	Aeroxide P25	10%	

3.2.3. Characterization of TiO_2 nanoparticles

Surface morphologies of different TiO_2 nanoparticles were investigated using a field emission scanning electron microscopy (FE-SEM, JSM-7600F). The crystallinity of pristine TiO_2 nanoparticles were analyzed using an x-ray diffractometer (XRD, D8 Advanced, Bruker) with monochromatized Cu-Kα radiation. N_2 adsorption-desorption was used to determine specific surface area of TiO_2 nanoparticles by Brunauer-Emmett-Teller (BET) theory. Bandgap of commercial TiO_2 were estimated by means of the diffuse reflectance spectroscopy (DRS, Varian Cary 5000).

3.2.4. Hydroxyl radical detection

The bleaching of p-nitrosodimethylaniline (RNO) by TiO_2 was investigated. RNO is an organic dye molecule and chosen as probe compound for evaluation of several oxidative species generated in the photocatalytic process. RNO has a strong yellow color in solution. It is used as a spin trap for detection of hydroxyl radicals. It will not react with singlet oxygen, superoxide anions and other peroxyl compounds (Cruz-Ortiz et al., 2017, Simonsen et al., 2010). In a typical procedure, 50 ml aqueous solution of RNO (50 μM) and 2.5 mg of the photocatalyst were placed in 100 ml Pyrex beaker. The suspension then irradiated with UV/visible light under continuous stirring with 160 rpm. Samples were taken at a regular time interval and centrifuged to separate the catalyst particles before analysis. The optical absorbance was recorded at 440 nm in an UV/visible spectrophotometer.

3.2.5. Dye degradation test

Rhodamine B was dissolved in distilled water to a concentration of 0.1 g/L. A circular zone with 2 cm diameter was circumscribed in the centre of a cement sample. A 100 μl of RhB solution was applied evenly on the zone using an adjustable precision pipette. The RhB contaminated samples were stored under dark conditions for 24 h followed by UV/visible light illumination. A 500 W long arc xenon lamp was used as the light source for UV/visible light photocatalytic reaction. The intensity of illumination on the surface of specimen was measured using a light meter (Lutron Digital Instruments). The illuminance on a sample surface perpendicular to the direction of source was around 10k lux. A portable spectrophotometer (MiniScan EZ

4000S, HunterLab, USA) was used for measuring the colour change during light exposure.

The results were expressed in L*a*b* colour space, as shown in Figure 3-2. In this colour space, L* indicates lightness, while a* and b* are chromaticity coordinates: +a* is in the red direction, -a* is in the green direction, +b* is in the yellow direction and -b* is in the blue direction. Since RhB dye applied to the cement sample was predominantly a red coloration, only a* coordinate was considered. During the application of RhB on the specimens, variations were observed in the intensity of the red colour at the specimens. Therefore, relative colour change ΔC was used to evaluate the photocatalytic degradation, using the following equation:

$$\Delta C_n = \frac{[(+a^*)_{dn} - (+a^*)_0]}{[(+a^*)_{d0} - (+a^*)_0]} \qquad (1)$$

where ΔCn is percentage of colour change at n period of illumination, (+a*)0 is the colorimetric coordinate a* on the specimen surface without RhB, (+a*)d0 is the colorimetric coordinate a* on the specimen surface with RhB dye but before the UV/visible light illumination, and (+a*)dn is the colorimetric coordinate a* on the specimen surface applied with RhB at n period of illumination. The sample will be considered as photocatalytic if ΔC4 > 20 % and ΔC26 > 50 % (Cassar et al., 2007). The long-term photocatalytic surface for RhB degradation was assessed for three cycles to simulate continuous process of dirt and staining on the cement-based surface. Test duration of each cycle was 26 h as described above and after that, the samples were exposed to UV/vis light and dark condition alternately until the colour change (ΔC) achieve more than 90%. RhB B dye was then reapplied to the specimens for the next cycle.

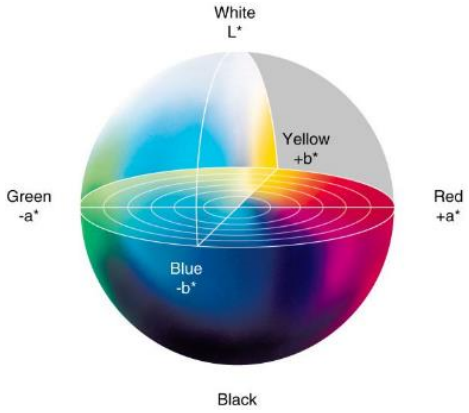

Figure 3-2: Self-cleaning result is expressed in L*a*b* color space

3.2.6. Water contact angle test

Surface property of TiO_2-based cementitious materials can be evaluated by measuring water contact angle of the sample after dropping water into its surface. Measurement of water contact angle was conducted to study the wettability of cement sample surface after UV/visible light treatments. This method is one of the indices affecting the level of self-cleaning performance. In this test, minimum 2 cement samples were tested with different TiO_2 loading. A 3 µl of water was dropped into the cement surface in different location. Water contact angle was measured using video contact angle system (VCA Optima, AST).

3.2.7. Anti-bacterial test

Escherichia coli K-12 (DSM) strain was used as model microorganism for photocatalytic disinfection experiments. *E. coli* was inoculated in a liquid nutrient medium (Difco™ LB Broth, Miller (Luria Bertani)) and incubated on a rotary shaker for 24 h at 37 °C. Bacteria were collected after incubation and optical density at 600 nm (OD600) method was used to estimate bacteria concentration. *E. coli* concentration was adjusted by dilution to reach the same initial concentration for all groups. The cement samples were firstly sterilized to kill existing bacteria. After sterilization process, the samples were irradiated with UV/visible light for 24 h to activate the photocatalyst. The light source used was similar to the light source used in dye degradation test. A total of 1 ml of *E. coli* suspension was then applied evenly on the cement surfaces using an adjustable precision pipette. The contaminated

samples were stored under dark conditions for 30 min. The viable bacteria in each sample were grown in LB agar dishes. The infected area and colony forming unit were examined after 24-h incubation at 37 °C. Figure 3-3 summarize the experimental procedure of anti-bacterial test.

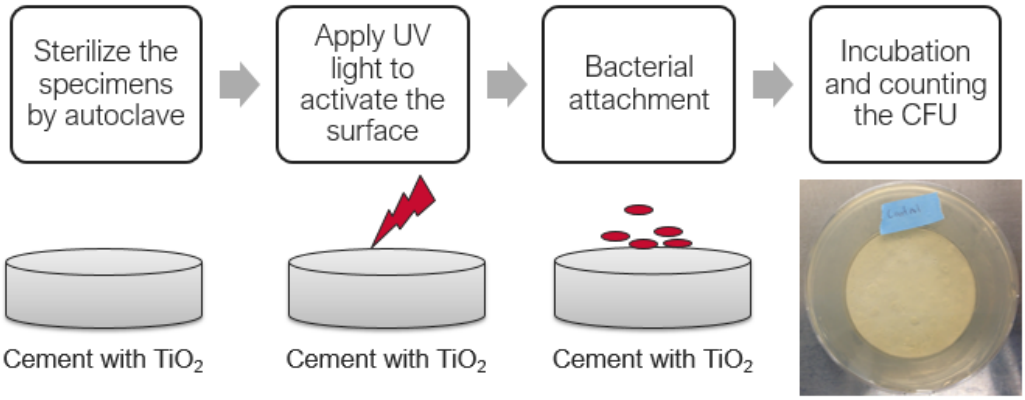

Figure 3-3: Experimental procedure for the surface study on anti-bacterial concrete

3.3. Result

3.3.1. Characterization of TiO_2 nanoparticles

The optical properties of various TiO_2 were examined using diffuse reflectance spectroscopy. Figure 3-4 presents the absorption spectra and bandgap energy calculation of Aeroxide P25, TiO_2-anatase, and TiO_2-rutile. While all the samples have a good response under UV light, only TiO_2-rutile has a response in visible light. It was indicated by higher absorption spectra crossed the visible light threshold. This means TiO_2-rutile could adsorb a light with smaller energy compared to the other materials, suggesting a lower bandgap for TiO_2-rutile than TiO_2-anatase and Aeroxide P25. The bandgap of photocatalyst can then be estimated from absorption spectra using Kubelka-Munk model and plotted using Tauc's relation:

$$\alpha h\nu = const\ (h\nu - Eg)^r \qquad (2)$$

where hν represent the energy of incident photon and the exponent r denotes the nature of transition. The Tauc's plot $(\alpha h\nu)^{1/r}$ versus hν has a distinct linear regime which indicates the onset of absorption. Linear extrapolation of this regime to energy axis at $(\alpha h\nu)^{1/r} = 0$ yields the bandgap energy of material, Eg. Assuming the value of

r is 2 (indirect allowed transition) for TiO_2 materials as reference used (Jimenez-Relinque et al., 2017, Zhang and Pan, 2011), the Tauc's plot of relationship between modified Kubelka-Munk function $(\alpha h\nu)^{1/2}$ and the energy of incident photon ($h\nu$) is illustrated in Figure 3-4(b). As shown in Figure 3-4(b), TiO_2-rutile has the lowest bandgap compared to Aeroxide P25 and TiO_2-anatase. The bandgap of Aeroxide P25, TiO_2-anatase and TiO_2-rutile is determined to be 3.21 eV, 3.20 eV, and 2.95 eV, respectively. Lower bandgap semiconductor, such as TiO_2-rutile in this case, should be preferred as it could be photoactivated by a smaller photon energy than that of higher bandgap semiconductor.

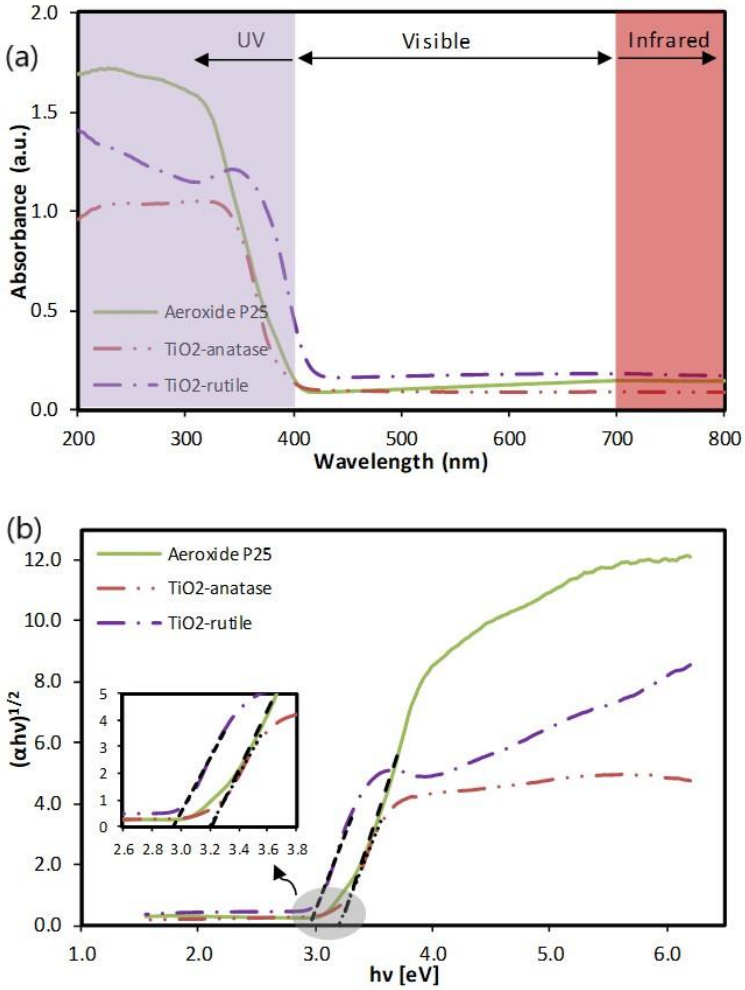

Figure 3-4: Optical properties of different TiO_2 materials (a) UV/visible absorption spectra and (b) Bandgap determination of various TiO_2

The morphologies of Aeroxide P25, TiO_2-anatase, and TiO_2-rutile are displayed in Figure 3-5(a-c). The particles show a spherical shape with a strong tendency to be clustered together, forming larger-size particles. As illustrated in Figure 3-5, in this dry state/powder form, Aeroxide P25 particles form agglomeration; whereas TiO_2-anatase and TiO_2-rutile particles form aggregation. According to ISO 14887, agglomeration is used to describe assemblage of particles which are loosely attached to each other at their corners or edges while aggregation is used to describe assemblage of particles that are rigidly joined together, as by partial fusion, sintering or by growing together (Nichols et al., 2002). It is essential to know whether the particles are in agglomerated or aggregated state (Jiang et al., 2009, Yousefi et al., 2013) to understand the configuration of particles in the dry and wet state (Figure 3-5(d)). It was suggested that the agglomeration of Aeroxide P25 nanoparticles is due to due to a weak van der Waals bond between primary particles (Jiang et al., 2009). Meanwhile, the aggregation of TiO_2-anatase and TiO_2-rutile was suggested due to a strong bond between primary particles as a result of sintering.

As it can be seen, the primary particle size of Aeroxide P25 is about 20-40 nm in diameter, while the primary particle size of TiO_2-anatase and TiO_2-rutile is in the range of hundreds nanometer. These results were in accordance with BET specific surface area (SSA) results listed in Table 3-1. SSA of Aeroxide P25 is 4-6 times greater than TiO_2-anatase and TiO_2-rutile. Aeroxide P25 offers higher number of active site available for photocatalysis due to its smaller particle size and higher SSA. Further, the contribution of hydroxyl radical production by various TiO_2 in the photocatalytic process was examined with respect to the TiO_2 surface and optical properties.

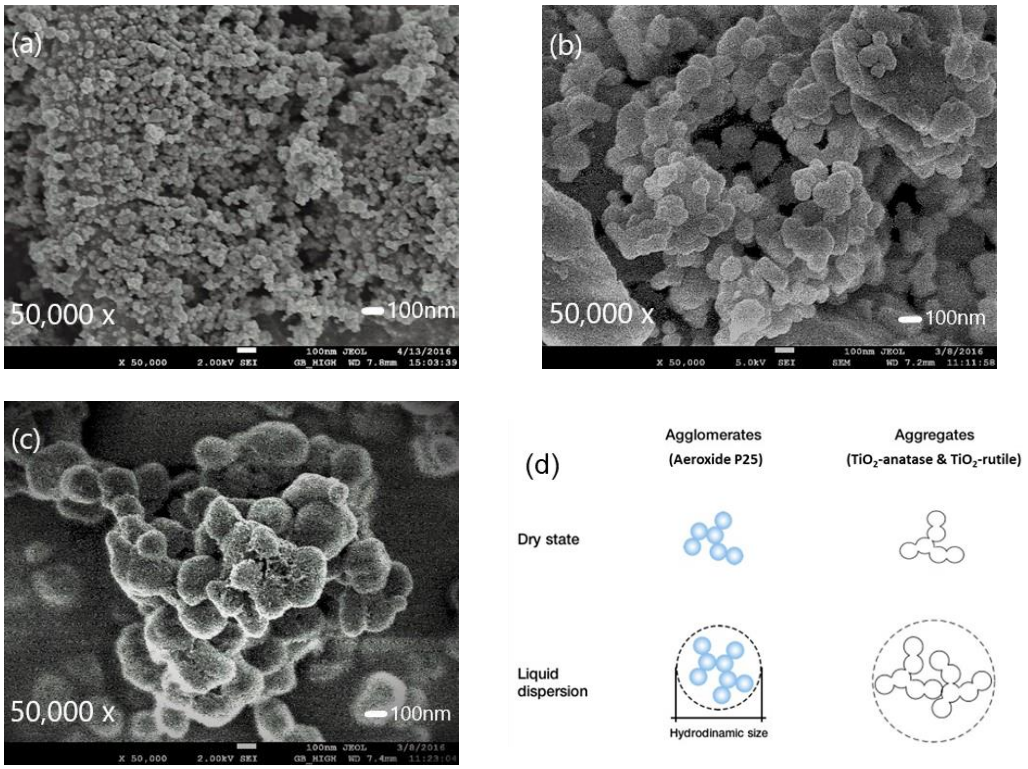

Figure 3-5: Secondary electron images of different TiO_2 nanoparticles (a) Aeroxide P25, (b) TiO_2-anatase, (c) TiO_2-rutile and (d) Various configuration of nanoparticles in the dry and wet state (Jiang et al., 2009)

Hydroxyl radical generation during UV/visible light illumination in the presence of various TiO_2 was detected by means of RNO degradation/bleaching. RNO bleaching can be investigated from the changes of absorption spectra recorded at a regular time interval. Absorption spectra in Figure 3-6 shows the photobleaching of RNO when irradiated in aqueous TiO_2-P25 suspension. Upon irradiation, a great decrease of peak intensity at 440nm was observed and it finally disappears after 60 min light irradiation. It was suggested that the hydroxyl radicals generated reacts with conjugated π bonds of RNO as shown in Figure 3-6 (Simonsen et al., 2010). Considering the band-energy level of P25 and RNO, oxidation of RNO by trapped holes or hydroxyl radicals is thermodynamically favorable. The potential of TiO_2 valence band is +2.5 V versus the normal hydrogen electrode (NHE) at pH 7.0, while the oxidation potential of RNO is only +0.3 V versus NHE at pH 7.0 (Zang et al., 1997). This makes the charge transfer process possible, from regions of low potential to the regions of high potential.

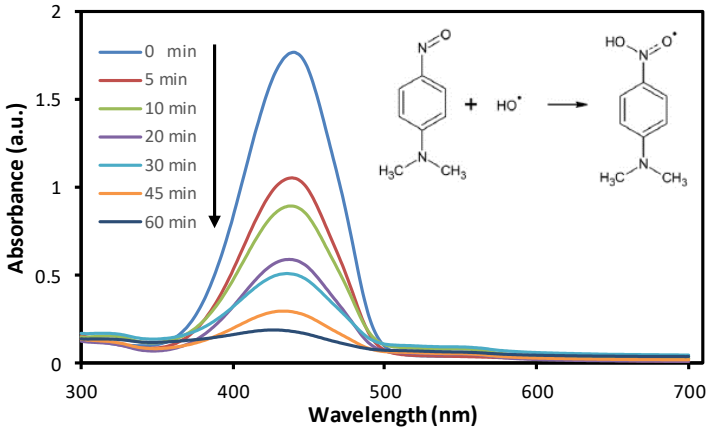

Figure 3-6: Absorption spectra of RNO bleaching in aqueous TiO_2-P25 suspension

Control samples in Figure 3-7(a) indicated that the presence of TiO_2 was essential for photobleaching of RNO, otherwise, no bleaching was observed. Aeroxide P25 showed highest OH● production due to its high surface area which provides a large number of active sites available for the photocatalytic process. Despite the fact that TiO_2-rutile has the smallest bandgap and higher SSA than TiO_2-anatase, OH● generation in the presence of TiO_2-rutile was the lowest one. It is not surprising as the reaction was thermodynamically not permissible due to band energy level of TiO_2-rutile (Mills and Le Hunte, 1997). The conduction band of rutile is 0.2V more positive than the reduction potential of electron acceptor (H+/H2). As a result, such condition inhibits electron transfer process, which in turn increase electron hole recombination and diminish photocatalytic activity.

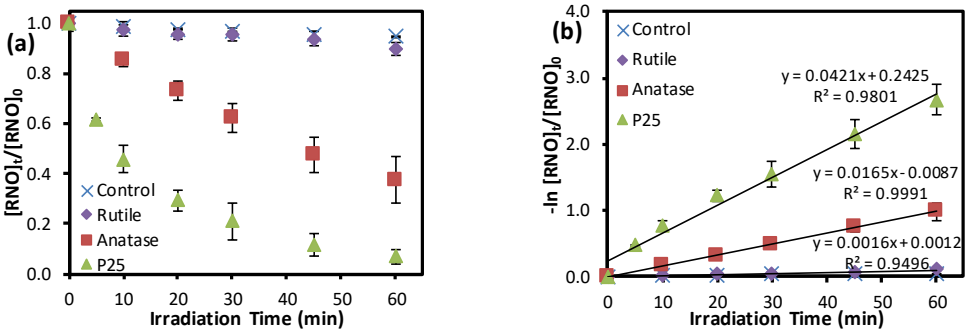

Figure 3-7: (a) Hydroxyl radical detection by means of RNO bleaching and (b) rate of hydroxyl radical production

Langmuir–Hinshelwood (L–H) mechanism has often been used to model the kinetics of photocatalytic activity (Carp et al., 2004, Mills and Le Hunte, 1997), as shown below:

$$r = -\frac{d[RNO]}{dt} = \frac{k_r K_e [RNO]}{1 + K_e [RNO]} \qquad (3)$$

as the condition of the experiment was carried out under low concentration of RNO (<< 10-3), the equation can be expressed as:

$$-\ln \frac{[RNO]_t}{[RNO]_0} = k_r K_e t = k' t \qquad (4)$$

where r is rate of reaction, k_r is the apparent reaction rate constant, K_e is the apparent equilibrium constant for the RNO to adsorb onto the surface of TiO_2, k' is the overall rate constant and t is the reaction time in minutes. Figure 3-7(b) shows ln $[RNO]_t/[RNO]_0$ has a linear relationship with irradiation time for various TiO_2. Hence, the hydroxyl radical generated at the sample surface followed first-order reaction kinetics. The slope of these lines could represent the rate of hydroxyl radical production with $k'_{P25} >> k'_{anatase} > k'_{rutile}$.

3.3.2. Microstructure of cementitious materials

During mixing process, TiO_2 nanoparticles were mixed with cementitious material as dry powder before added into an aqueous media. Figure 3-8 displays the microstructure of hydrated cement paste without and with TiO_2 nanoparticles. Relatively smaller TiO_2-P25-cluster (Figure 3-8(b)) was observed on the surface of the ettringite compared to TiO_2-P25 in the dry state. However, aggregation of TiO_2 particles on the cement matrix was still observed for the cement samples with TiO_2-anatase and TiO_2-rutile (Figure 3-8 (c-d)). The effect of pH on nanoparticle dispersion size could be used as a basis to explain this finding. In DLVO theory of suspension, the stability of particle dispersions is determined by the balance of the electrostatic repulsion force and attractive forces. In high pH environment during mixing process, the agglomeration of TiO_2-P25 can be suppressed as the repulsive force in TiO_2-P25 become more dominant than the van der Waals force under strong alkaline condition (Jiang et al., 2009). However, such forces are not enough to break the strong bounds

between individual particles in aggregated-TiO_2. Hence, in the case of TiO_2-anatase and TiO_2-rutile, these TiO_2 nanoparticles tend to remain as aggregates or even create a larger particle in the hardened cement paste.

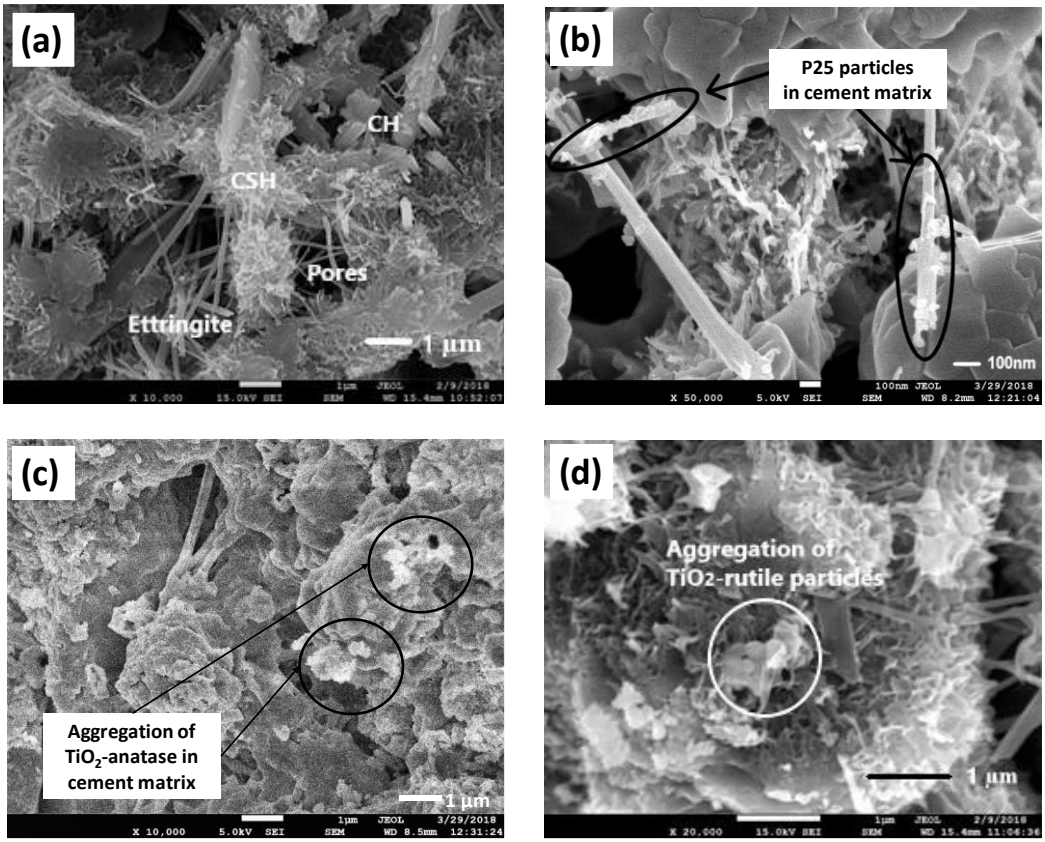

Figure 3-8: SEM images of hardened cement pastes (a) without TiO_2, (b) 5% P25, (c) 5% TiO_2-anatase, and (d) 5% TiO_2-rutile

Furthermore, the increase of TiO_2 concentration in cement matrix could intensify its agglomeration/aggregation degree. The inset images in Figure 3-9(a) and Figure 3-9(b) show TiO_2 particle distribution in cement matrix with the increasing TiO_2 loading. TiO_2 particles firstly occupied the interlacing network pores of hydration products. Further increase of concentration subsequently covered more and more on the surface of hydration product, which enlarges TiO_2 agglomeration level on substrate surface. This finding is consistent with the work by Yang et al. (2017) and Zhao et al. (2015). Furthermore, the EDX spectrum and the inset table in Figure 3-9(a) and Figure 3-9(b) present the elemental identification and quantitative compositional information of hardened cement. The spectrum showed the presence of Ca, O, Si and a low level of Ti. It was shown that the weight percentage of Ti atom

(the inset table in Figure 3-9) on cement matrix is generally less than its loading concentration. The gap between TiO_2 loading and estimated TiO_2 content become higher with the increasing of TiO_2 loading.

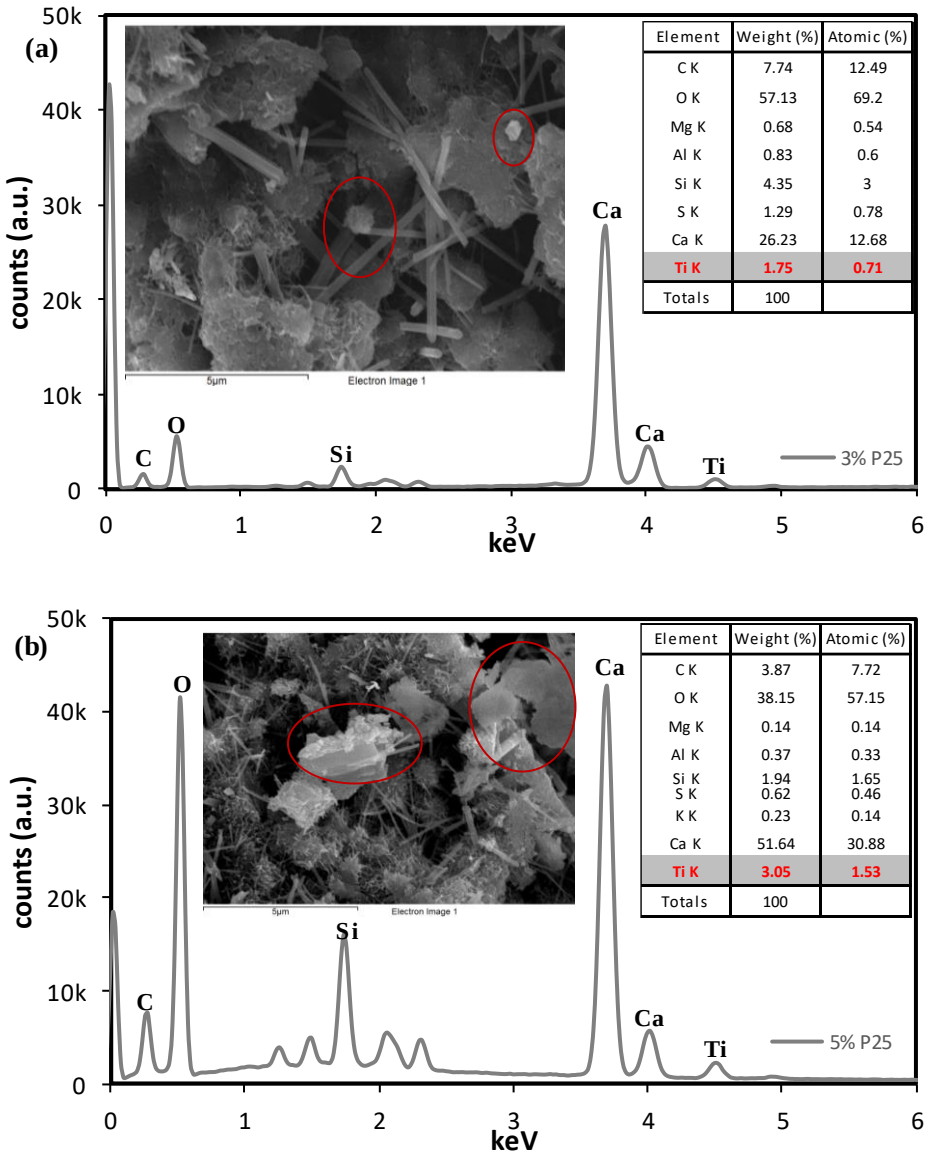

Figure 3-9: SEM images and EDX spectrum showing a presence of Ca, O, Si, and low level of Ti element

3.3.3. Dye degradation test

In this study, self-cleaning activity of the prepared cement samples was evaluated by measuring the degradation of dyes under UV/visible light irradiation. Rhodamine B (RhB) dye which shows a strong red colour was used for this self-cleaning test. RhB

has been extensively used to evaluate self-cleaning effect in photocatalytic cementitious materials for the following reasons. Firstly, the structure of RhB is similar to the structure of anthracene, an example of polycyclic aromatic hydrocarbons compounds (PAH compounds) (Gustafson and Dickhut, 1997). PAHs are example of soiling agents found in urban environments and mainly produced by incomplete combustion of organic matter. Secondly, RhB dye is relatively stable in alkaline environment of cementitious surface (Ruot et al., 2009). Lastly, RhB dye is water-soluble and hence can be spread easily on the surface of cement samples.

Figure 3-10 show dye degradation efficiencies as the result of the effect of TiO_2 type and the effect of TiO_2 loading. The effect of TiO_2 type on RhB degradation (Figure 3-10(a)) indicate that cement sample mixed with Aeroxide P25 achieved the highest degradation of dye compared to TiO_2-anatase and TiO_2-rutile under the same TiO_2-loading. P25-cement sample is the only TiO_2-cement shows degradation of dye larger than the photocatalytic limits ($\Delta C_4 > 20\%$ and $\Delta C_{26} > 50\%$). In P25-cement sample, the degradation of RhB dye generally happens in the first four hours of UV illumination. Its performance at 4h and 26h is around $\Delta C_4 = 51.4\%$ and $\Delta C_{26} = 57.8\%$, respectively. Thus, around 80% of total degradation happens in the first 4h of experiment. This finding is consistent with earlier findings suggesting that the degradation of dye on treated-samples is rapid and reach its maximum efficiencies after four hours of UV exposure (Graziani et al., 2014, Krishnan et al., 2013). The result is in accordance with RNO bleaching results in which highest $OH^{\bullet}$ radical production was achieved in the presence of Aeroxide P25 as a photocatalyst. However, due to aggregation problem on TiO_2-anatase cement samples, it reduces the active surface available for photocatalytic reaction and then might significantly lowering $OH^{\bullet}$ radical production, compared to $OH^{\bullet}$ radical production in TiO_2-anatase suspension system. As a result, TiO_2-anatase-cement shows very low degradation after 4h of UV exposure similar to control cement and TiO_2-rutile-cement. It is suggested that the improvement of degradation with increasing irradiation time for these three samples were due to direct photolysis of the dye.

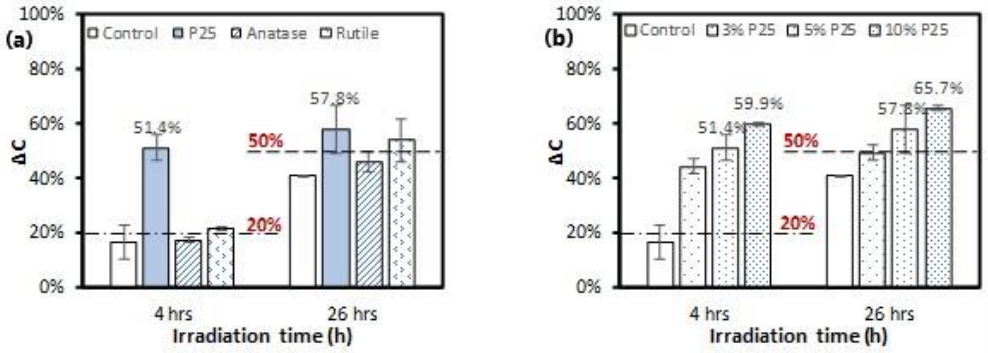

Figure 3-10: Dye degradation efficiencies (a) Effect of TiO_2 type and (b) Effect of TiO_2 loading

The effect of TiO_2 content was further studied by varying the Aeroxide P25 content - 0%, 3%, 5%, and 10%. As can be seen in Figure 3-10(b), about 3% of Aeroxide P25 is adequate to achieve minimum photocatalytic performance ($\Delta C_4 > 20\%$ and $\Delta C_{26} > 50\%$). Degradation of RhB obviously improves with the increasing of TiO_2 amount as it provides more active site for reaction. However, the improvement in dye degradation is not linearly proportional to the TiO_2 loading (Figure 3-10(b)). It is noticed that, unlike the effect of 3% TiO_2 loading, RhB degradation improvement is not significant with further increase of TiO_2 content from 3% to 5% and 5% to 10%. Generally, light intensity, surface area, and pore structure of cement paste samples highly influence their photocatalytic activity (Zouzelka and Rathousky, 2017, Guo et al., 2017, Yang et al., 2017). As previously discussed, increasing TiO_2 loading can lead to serious agglomeration problem. Such agglomeration/aggregation problem control the utilization of TiO_2 nanoparticle in cement matrix for photocatalytic reaction.

It is necessary to evaluate the durability and repeatability of photocatalytic activity for practical application. As shown in Figure 3-11, in general, Rhodamine B removal efficiency of TiO_2 cementitious materials gradually decreased after several cycles of application. The cycling processes simulated the continuous process of dirt and staining on the cement-based surface. For each cycle, TiO_2 cementitious materials could not fully degrade the applied dye, creating a thicker stain layer on the surface with the increase of testing cycle. It is suggested that the remaining dye on the surface of samples could block the active sites available for further photocatalysis reaction. It has led to a reduction of Rhodamine B removal efficiency after application of

several cycles. This assumption is supported by previous studies (Guo et al., 2016, Krishnan et al., 2013), which observed that remaining dye blockage is one of the main reason for photocatalytic deactivation.

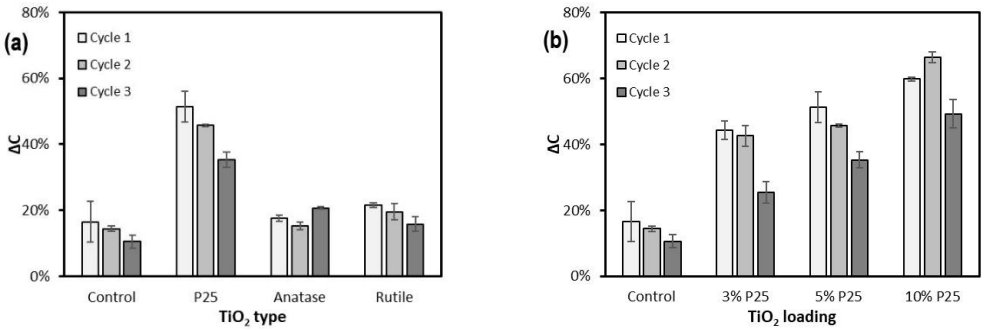

Figure 3-11: Rhodamine B removal efficiencies after three cycles of application

3.3.4. Water contact angle test

Water contact angle test is one of the methods to evaluate self-cleaning performance. Figure 3-12 displays water contact angle on cement surface with various loading of Aeroxide P25 - 0%, 5% and 10%. It can be seen that increasing TiO_2 loading result in the increase of water contact angle and improve the level of hydrophobicity. More hydrophobic surface prevents the fast contact and adhesion of pollutant into cement-based surface. After UV/visible light exposure, the water dropped onto TiO_2-based surface forms very low contact angle compared to control specimen, as shown in Figure 3-12. This effect is assigned to photoinduced super-hydrophilic surface. The effect improves with increasing TiO_2 loading as the higher TiO_2 content generate more hydroxyl radicals or trapped holes to facilitate the reaction. Fujishima et al. (2000) pointed out that the mechanism of this photoinduced hydrophilic effect initiated by similar process as photodegradation, which is generation of electron-hole pairs. The generated electron-holes pair could react with the Ti^{4+} cations and the O^{2-} anions to form the Ti^{3+} and O_2, respectively, creating the oxygen vacancies. The oxygen vacancies can be then occupied by water molecules, forming layer of chemisorbed OH groups. This layer formation is inclined to make the surface hydrophilic and avoid the close contact between surface and adsorbed contaminant (Guan, 2005). As a result, even though the energy of adsorbed light may be

insufficient to decompose the dirt and other impurities, the surface is maintained clean when water flow is supplied (Fujishima et al., 2008).

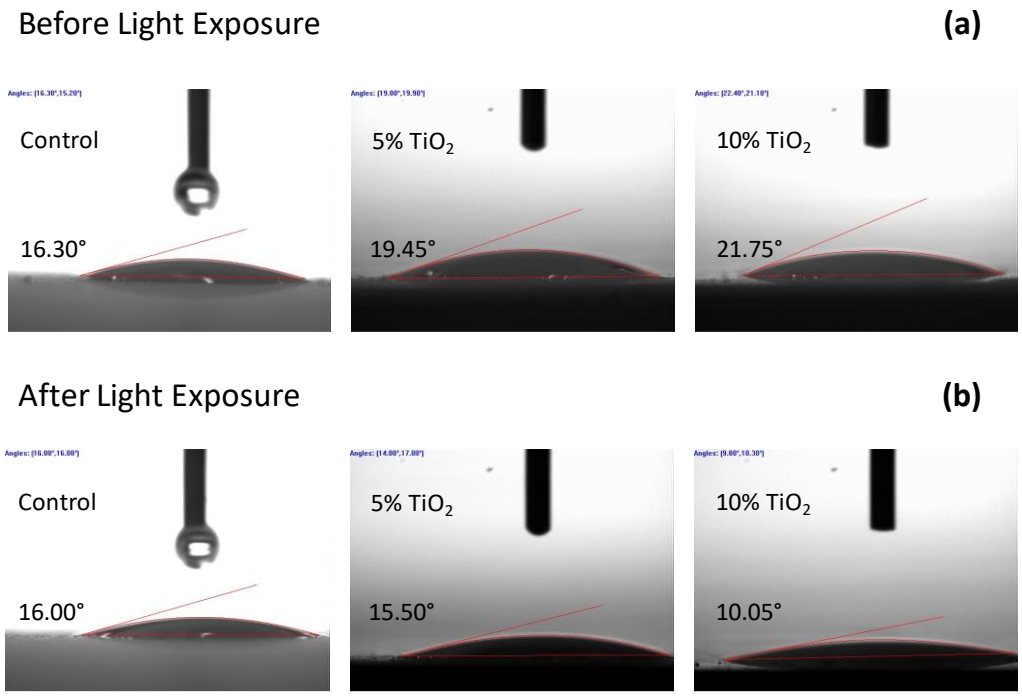

Figure 3-12: Water contact angle of cement surface containing 0%, 5%, and 10% TiO_2

3.3.5. Antibacterial test

Application of TiO_2-based cementitious materials for exterior building can also be utilized as a strategy to prevent biofilm formation on the surface. The presence of TiO_2 nanoparticles together with plenty of sunshine could inhibit microbial contamination on cement-based surface. The preliminary study was conducted to evaluate the existence of airborne microbes in different environments. Figure S12 shows a comparison of microbial growth result after 1-day incubation and 5-day incubation in 37 °C for different locations. The result indicated that outdoor environment has low concentration of airborne microbes by showing a small number of bacteria and fungi. As widely known, UV light from sunlight itself is able to kill bacteria, germs, and others microorganism, keeping the outdoor environment relatively clean. However, by long-time exposure of exterior buildings to airborne microbes, these remaining microbes could attach and colonize on the building surface.

Anti-microbial activity of cement-based surface containing TiO_2 catalyst is examined for preventing *E. coli* colonization. As this study was focused on a strategy to prevent the microbial colonization on the exterior building, the specimens were exposed to UV/vis light before getting in contact with bacteria. The results of estimated infected area on the surface of photocatalytic cementitious composite are presented in Figure 3-13. Interestingly, a significant anti-bacterial effect was achieved by the sample with 3% and 5% of Aeroxide P25. It can be seen from Figure 3-13, cement surface containing Aeroxide P25 generally displays much less infected area compared with control specimen. The bacteria survival was estimated on agar dish after 24-h incubation (Figure S13). The center part of agar dish showed visually the bacteria grow after 24-h incubation. Bacterial survival was very low after getting in contact with cement paste containing 5% TiO_2. Furthermore, the contaminated surface without light exposure (under dark condition) was conducted as a control to ensure that photocatalytic reaction could only start after UV/vis light absorption. In this test, with no UV/vis light treatment, *E. coli* suspension was applied on the surface of cement sample with 5% Aeroxide and without TiO_2 (control specimen). The result shows that both of the cement samples have no anti-bacterial activity (Figure S14).

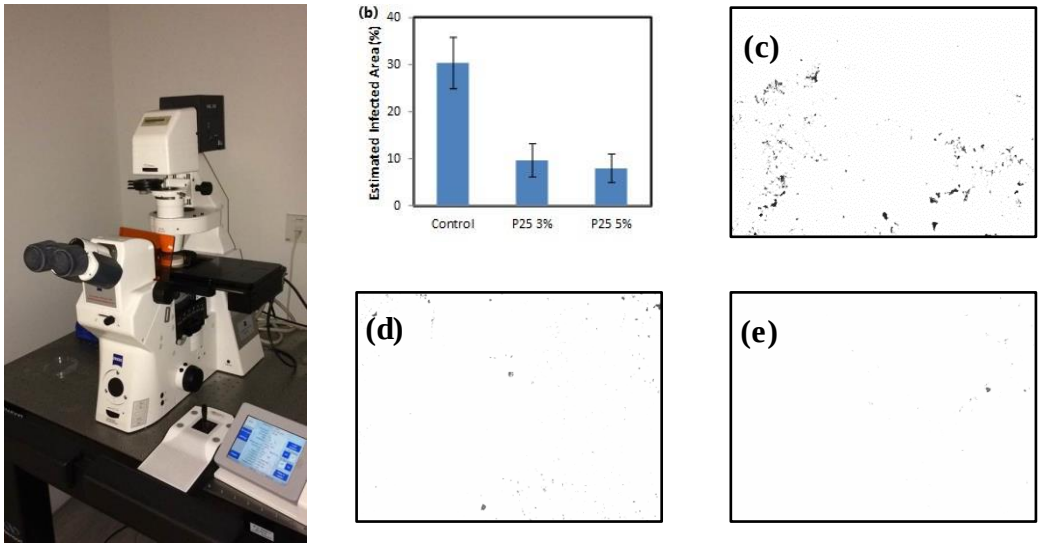

Figure 3-13: (a) Microscope used for study, (b) comparison of estimated infected area, (c) Control specimen, (d) 3% Aeroxide P25, and (e) 5% Aeroxide P25

As incorporation of TiO_2 with different loading level has some effect on pore structure of cementitious composite, the effect of cement pores was evaluated. The

experimental procedure to study the effect of porosity on anti-bacterial activity is shown in Figure S15. In the typical procedure, after application of *E. coli* suspension, the bacteria on the surface was cleaned by ethanol 70% and the remaining bacteria in the pores was washed by 0.9% NaCl buffer. It was then re-cultured on agar dish and incubated for 24 h at 37 °C. The percentage of bacteria survival was calculated using the following equation:

$$\%\ bacteria\ survival = \frac{Number\ of\ colonies\ in\ treated\ sample}{Number\ of\ colonies\ in\ control\ sample} x100 \qquad (5)$$

As shown in Figure 3-14, in general, the bacteria survival for cement paste containing 3% and 5% Aeroxide P25 is much lesser than control specimen.

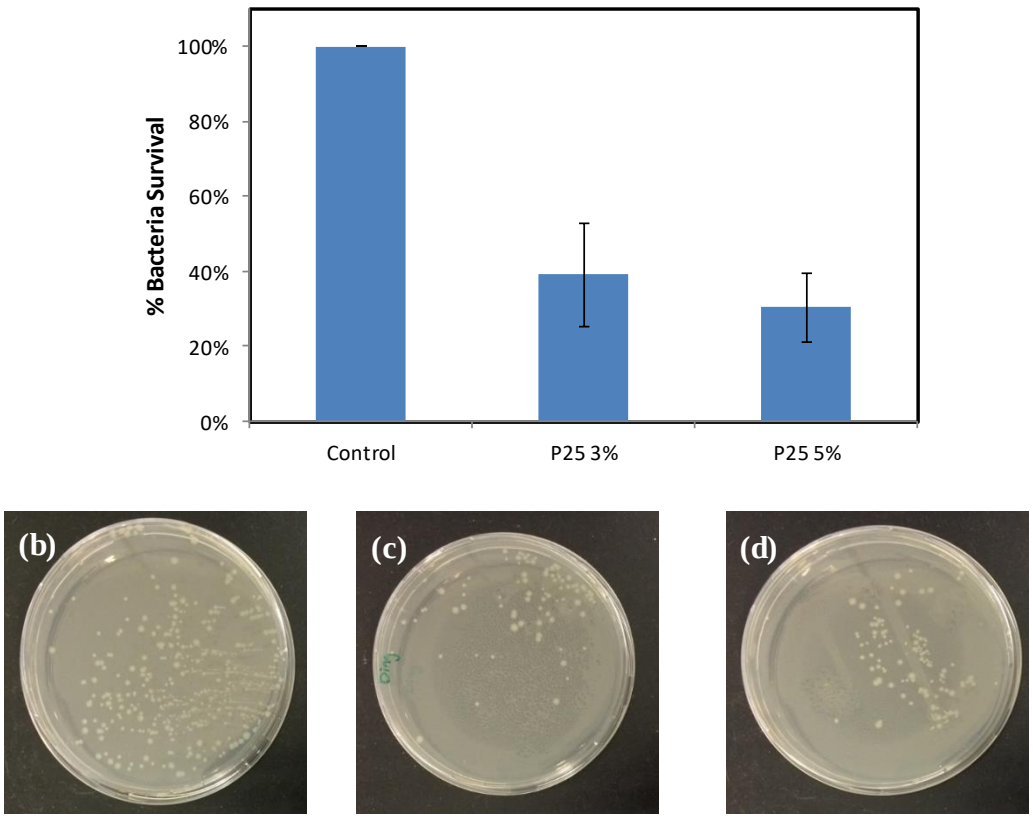

Figure 3-14: Anti-bacterial activity test from contribution of cement pores (a) Quantification of colony forming unit and (b-d) The viability of E. coli after 24 h incubation with control specimen, 3% P25, and 5% P25, respectively

This result indicates an obvious anti-bacterial activity of TiO_2-based surface. The TiO_2-based substrate might inhibit the initial adhesion of *E. coli* and as a result reduce

bacterial colonization (Davidson et al., 2015, Lorenzetti et al., 2015, Peng et al., 2013). As discussed earlier, $OH^{\bullet}$ generation in the presence of Aeroxide P25 was the highest one. It is suggested that this $OH^{\bullet}$ radicals is responsible for significant cellular damages (DNA, RNA, Lipids, Protein) (Daly et al., 2007). Moreover, Carre et al. (2014) revealed dual effects of superoxide anions (O_2^-) on lipid peroxidation that could enhance membrane fluidity and disrupt cell integrity. After eliminating the cell wall protection, the oxidative damage takes place on the plasma membrane of the bacteria, resulting in subsequent rapid death of cell (Kubacka et al., 2014).

3.4. Summary

In this study, nanoscale analysis of different TiO_2 materials, microstructure of TiO_2-based cementitious materials, and photocatalytic performance for self-cleaning and anti-bacterial application was investigated. Nanoscale analysis demonstrated that Aeroxide P25 showed highest $OH^{\bullet}$ production due to its high surface area which provide a large number of active sites available for photocatalytic process. Although TiO_2-rutile has the smallest bandgap, $OH^{\bullet}$ generation in the presence of TiO_2-rutile was the lowest one. It is not surprising as the reaction was thermodynamically not permissible due to band energy level of TiO_2-rutile. The structure of TiO_2 in the nanoscale greatly affect its photocatalytic performance in cement-based application. Cement sample containing Aeroxide P25 achieved much higher RhB degradation compared to TiO_2-anatase and TiO_2-rutile with the same loading. The long-term performance of RhB degradation was reduced after several cycles of application due to the accumulation of intermediates that might block the active sites.

Addition of TiO_2 into cementitious composite make the surface more hydrophilic. As a result, the self-cleaning effect would be more significant especially if there is a rainwater coming to wash away a remaining dirt or contaminant on the surface. On the other hand, the strategy to use TiO_2-based cementitious materials for exterior building is promising to prevent biofilm formation on the surface. Cement surface containing Aeroxide P25 generally displays much less infected area / lower bacteria survival compared to control specimen.

Since TiO_2 is intermixed with cement mechanically, these TiO_2 nanoparticles tend to agglomerate or aggregate during mixing process, reducing the surface area available for photocatalytic process. Hence, exploring another dispersion method to improve TiO_2 distribution on cement matrix could be beneficial to increase photocatalytic efficiencies. Although more research is still needed to improve the efficiency of self-cleaning and anti-bacterial effect, especially under low light intensity or visible light irradiation, the result demonstrated in this work is promising. The use of TiO_2 based cementitious materials as exterior building could passively maintain a good appearance of the building and potentially prevent deterioration of cement/concrete-based surfaces, resulting in a reduction of maintenance work.

Chapter 4. Graphene-based TiO_2 nanocomposites for enhanced visible light degradation of organic dye and antibacterial effect of *Escherichia coli*

4.1. Overviews

Since Fujishima and Honda (1972) introduced the scientific concept of photocatalysis, enormous research work has been done to understand the fundamental mechanism and further improve the efficiency of various photocatalysts. In recent years, titanium dioxide (TiO_2) has been proved to be the most suitable photocatalyst for environmental control due to its capability to completely destroy a large variety of organic pollutants (Carp et al., 2004, Mills and Le Hunte, 1997). Titanium dioxide particle is abundant, economical, relatively non-toxic, highly photoactive, yet chemically stable and resistant to photocorrosion (Evans et al., 2013, Fujishima et al., 2008, Ohama and Van Gemert, 2011). However, the wide bandgap of pristine TiO_2 hinders its full potential for many applications (Agrios and Pichat, 2005, Linsebigler et al., 1995). The bandgap of TiO_2 lies in the UV region which is only 3-5% of the sunlight energy. Therefore, one of the main challenges in improving the performance of TiO_2 photocatalyst is to extend their optical response from the UV to the visible region.

Improving the optical-response and photocatalytic performance of TiO_2 in the visible light region can be achieved by doping or sensitization (Xiaobo and Mao, 2007). Doping is a kind of bulk chemical modification to alter the chemical composition of TiO_2 but maintain the integrity of TiO_2 crystal structure. This technique substitutes the metal (titanium) or the non-metal (oxygen) component in order to alter the optical properties of TiO_2 nanomaterial. The study by Endo et al. (2018) show that doped the commercial Titania samples with metal such as silver or gold result in excellent visible-light driven photodecomposition of microorganisms. An alternative technique is a photosensitization, a photochemical process by which a chemical reaction is induced by energy transfer from the light-absorbing sensitizer (Braslavsky, 2007). The match of the energy difference between the oxidation potential of the excited sensitizer and conduction band of the TiO_2 acts as the driving force for the charge

injection process (Vinodgopal et al., 1995). The sensitizer for TiO_2 materials can be any materials with a lower bandgap, including semiconductors, metals, and organic dyes (Vallejo et al., 2015, Cabir et al., 2017).

Surface modifications of TiO_2 with carbonaceous materials such as graphene oxide (GO) have received great attention due to its excellent photocatalytic performance in the visible light (Chen et al., 2010, Chen et al., 2009, Du et al., 2011, Lettmann et al., 2001, Morales-Torres et al., 2012, Nguyen-Phan et al., 2011, Zhang et al., 2010a, Cruz-Ortiz et al., 2017). This composite can be synthesized by different methods, for example sol-gel method, hydrothermal/solvothermal technique, or even simple mixing process. In sol-gel method, typically it starts with solutions consisting of metal compounds (sol) as precursor (Sakka, 2013). Further reaction integrates the network between particles, solidifying the sol into a gel. Sol-gel routes afford excellent control of nanosized particles, shapes distribution and crystallinity. However, it has a number of disadvantage such as substrate dependent (typical precursor is metal alkoxides which is high cost materials) and time consuming due to slow process of gel formation (Mackenzie, 1988). Hydrothermal technique involves single or heterogeneous phase reactions under controlled temperature and pressure to crystallizing substance from aqueous solution (Morales-Torres et al., 2012, Suchanek and Riman, 2006). It allows shorter processing time and lower energy consumption since high calcination temperature, mixing, and milling can be minimized. The need of expensive autoclaves is one of the main disadvantages of these methods.

The paper presents an experimental study to prepare the GO-TiO_2 nanocomposites by a one-step hydrothermal process. The preparation route will be simplified and conducted at ambient conditions. It could allow the scaling-up process for commercial production and hence promotes the potential of GO-TiO_2 composites towards wider practical applications such as construction industry. First, the photocatalytic performance of various commercial TiO_2 nanoparticles will be evaluated. The commercial TiO_2 product that performs the best will be selected for synthesis of a series of GO-TiO_2 composite photocatalysts. Different reaction conditions will be carried out to optimize the photocatalytic activity under visible light illumination. The photocatalytic performance in visible light will be evaluated

for degradation of methylene blue dye and antibacterial effect (*Escherichia coli*). A preliminary study was also conducted to evaluate the application of GO-TiO_2 composite in cement-based construction materials for decomposition of *E. coli*.

4.2. Methodology

4.2.1. Materials

Four commercial titanium dioxide catalysts were used for screening test: Aeroxide TiO_2 P25 (Evonik, Germany), KRONOClean 7000 (KRONOS, USA), Anatase (Shijiazhuang Kailing, China) and Rutile (Shijiazhuang Kailing, China). Commercially available graphene oxide (>99% purity and research grade quality) was purchased from HENGQIU Technologies, China. It is small scale single layer graphene oxide prepared by improved hummers method. Methylene blue was used for photodegradation of dye and it is obtained commercially from Sigma-Aldrich, Singapore. Bacteria *E. coli* K-12 obtained from the bacterial library in the environment laboratory of Nanyang Technological University was used for antibacterial test.

4.2.2. Synthesis of GO-TiO_2 nanocomposite

The composites were prepared through a one-step hydrothermal process using the selected commercial TiO_2 and GO, based on the work of Zhang et al. (2010a) with modifications, as illustrated in Figure 4-1. The GO loading was kept constant at 3% weight of TiO_2 as an optimum content (Pastrana-Martínez et al., 2012). Briefly, 242.5 mg of TiO_2 powder was dispersed in 35 ml of distilled water. The TiO_2 solution was then stirred continuously for 30 min at room temperature (≈ 23-25 °C) using a magnetic stirrer at 160 rpm. In the meantime, 7.5 mg of graphene oxide was dissolved in 15 ml of distilled water. The GO solution was sonicated at room temperature (≈ 23-25 °C) for 30 min using a high-intensity ultrasonic probe. Subsequently, the obtained GO solution was added to the TiO_2 solution under magnetic stirring for another 30 min. The mixture was then stirred at 150° C until all water completely evaporated. Lastly, the obtained solid deposit was then oven-dried for 24 h at 60° C. The final product is referred to as GO-TiO_2.

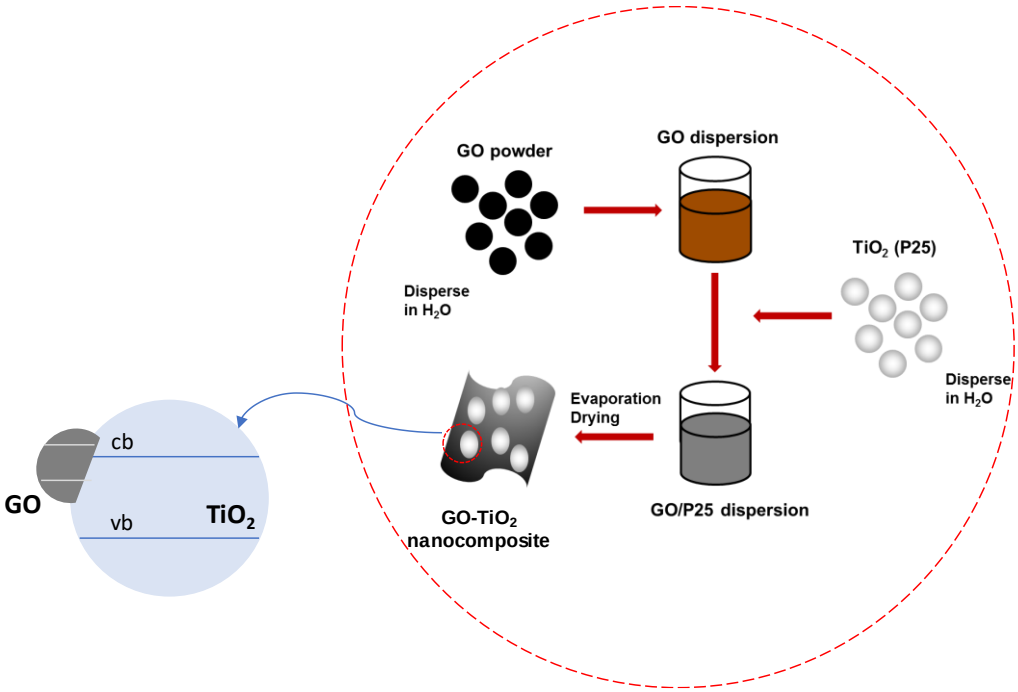

Figure 4-1: Synthesis process of GO-TiO_2 nanocomposites

4.2.3. Sample characterization

The morphology of composites was characterized using a field emission scanning electron microscopy (FE-SEM, JEOL JSM7600F) and the elemental analysis and mapping were carried out by energy-dispersive x-ray spectroscopy (EDX) on the same instrument. The GO content in the GO-TiO_2 composites was analyzed under dry air using a thermogravimetric analyzer (Perkin Elmer TGA 4000). The samples were heated from room temperature to 800° C at a rate of 10° C/min. The crystal structure of pure TiO_2 and GO-TiO_2 composites were investigated using an x-ray diffractometer (D8 Advanced XRD, Bruker AXS, Germany) with monochromatized Cu-Kα radiation. The functional groups of the GO, TiO_2, and GO-TiO_2 composites were detected using a Fourier transform infrared spectroscopy (FTIR, Perkin Elmer Frontier) in the range of 4000–600 cm^{-1}. The X-ray photoelectron spectroscopy (XPS) analysis was used to further identify the interaction between GO and TiO_2. The optical properties of the catalysts were investigated by means of the diffuse reflectance spectroscopy (DRS, Varian Cary 5000). Specific surface area of the catalysts was measured by Brunauer-Emmett-Teller (BET) nitrogen adsorption-desorption. Surface charge of TiO_2 materials was assessed by measuring their electro-

kinetic potential (zeta potential) via zeta potential analyser (Malvern Zetasizer Nano ZS).

4.2.4. Photocatalytic degradation of methylene blue under visible light

The degradation of methylene blue was observed based on the absorption spectroscopic technique. In a typical procedure, 50 ml aqueous solution of methylene blue dyes (10 μM) and 50 mg of the photocatalyst were placed in 100 mL Pyrex beaker. The mixture was then stirred in the darkness until reaching the adsorption equilibrium. The photocatalytic reaction was started by turning on the lamp. A 500 W long arc xenon lamp with a UVIRCUT420 optical filter was used as the light source for visible light photocatalytic reaction. After turning on the lamp, the mixture was irradiated for certain period and stirred incessantly during irradiation.

The dyes solution was taken from the reactor at a regular time interval and centrifuged to separate the catalyst particles before analysis. The photo-reacted solution was analysed by recording variations of the absorption band maximum (660 nm) in the ultraviolet-visible spectra of methylene blue using an ultraviolet-visible (UV-vis) spectrophotometer (Varian Cary 5000). Direct photolysis in the absence of photocatalyst was also performed as a blank experiment in order to calculate the contribution from direct photolysis.

Dark adsorption test was evaluated to compare the adsorption capability of pure TiO_2 and GO-TiO_2 composite. In this test, 50 mg of the photocatalyst was dispersed in 50 mL of methylene blue solution (10 μM). The solution was continuously stirred and kept in the dark for 30 min. Every 15 min, the sample was taken and centrifuged for the UV-visible absorption measurement. From the difference in the absorbance before and after adsorption, the amount of dyes adsorbed by the photocatalyst could be estimated.

4.2.5. Photocatalytic disinfection of *E. coli* under visible light

The photocatalytic activity of the TiO_2-based material was evaluated by disinfection of *E. coli* under visible light irradiation at room temperature (≈ 23-25 °C). Briefly, the *E. coli*. K-12 was obtained from the bacterial library in the environment laboratory

of Nanyang Technological University. Unless specifically noted, *E. coli*. mixing with 50% glycerol (mix ratio volume/volume = 1/1) was kept in -80 °C for long-term storage. After overnight growth in 37 °C, 200 rpm incubator, the overnight bacterial cultures were diluted to same concentration for all TiO_2-based material groups (GO, P25, Krono, GO-P25, GO-Krono). Then same amount of different TiO_2-based materials was added for 60-min incubation (final concentration: 50 mg/l). During 60-min incubation, the samples were collected at the 6 time points (Min 0, Min 10, Min 20, Min 30, Min 45, Min 60) and the live bacteria number was calculated by colony forming unit (CFU) and drop-plate method described in the previous study (Ding et al., 2014b).

4.3. Result and discussion

4.3.1. Physicochemical properties of pristine titanium dioxide

Four commercial TiO_2 samples were evaluated in this screening test. Figure 4-2 displays the morphologies of various commercial TiO_2 particles. As it can be seen, the TiO_2 particles used in this screening test show a spherical shape with strong flocculation to form larger-size clusters. The primary particle size of TiO_2-P25 and TiO_2-Krono is estimated to be about 20-40 nm in diameter, while the particle size of TiO_2-anatase and TiO_2-rutile is in the range of hundreds nanometer. However, in the case of the TiO_2-Krono photocatalyst, the primary particles tend to agglomerate to form larger secondary particles (> 500 nm) giving raise to the porous structure.

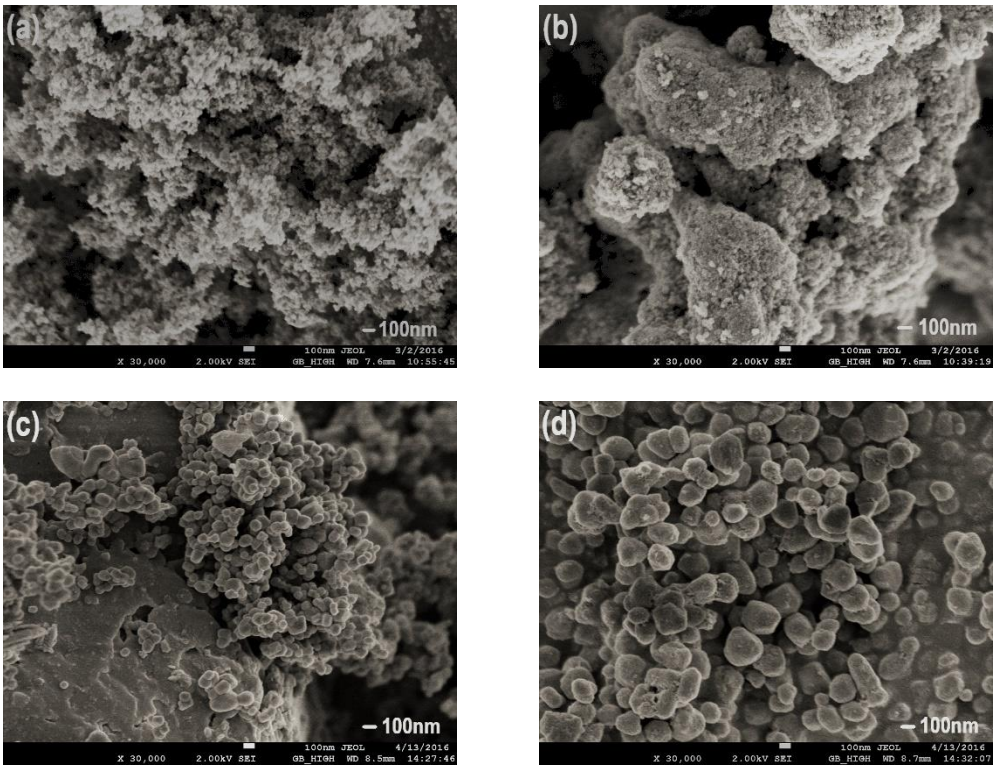

Figure 4-2: Scanning electron microscope (SEM) images of different commercial TiO_2 powders: (a) TiO_2-P25, (b) TiO_2-Krono, (c) TiO_2-anatase and (d) TiO_2-rutile

The specific surface area and pore structure were then evaluated by N_2 adsorption experiment. Figure 4-3 presents the physisorption isotherm of four commercial TiO_2 used in this study. As shown in Figure 4-3, the physisorption isotherm for TiO_2-Krono photocatalyst shows a hysteresis effect indicating that the particles are mesoporous. In comparison, the observed isotherms for TiO_2-P25, TiO_2-anatase, and TiO_2-rutile suggest that particles are non-porous. Brunauer–Emmett–Teller (BET) theory was adopted to calculate surface area. The surface area for all commercial TiO_2 is tabulated in Table 4-1. As listed in Table 4-1, the calculated BET shows that TiO_2-Krono has the highest specific surface area (252 m^2/g) followed by TiO_2-P25 with 46.9 m^2/g. The high surface area for TiO_2-Krono was strongly correlated to mesopore volume (Chang et al., 2009). In contrast, the surface area for TiO_2-anatase and TiO_2-rutile samples is only 8 and 10 m^2/g, respectively.

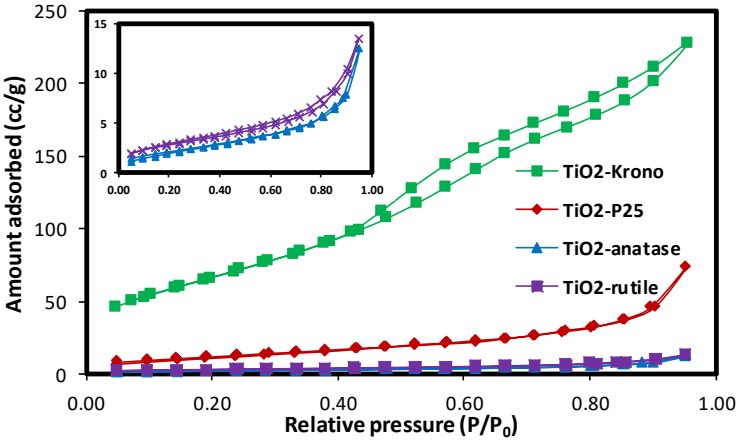

Figure 4-3: N_2 adsorption isotherms of TiO_2-P25, TiO_2-Krono, TiO_2-anatase, and TiO_2-rutile

The crystal structures of commercial TiO_2 materials were investigated through the XRD analysis. Figure 4-4 shows the XRD patterns of TiO_2-P25, TiO_2-Krono, TiO_2-anatase, and TiO_2-rutile. As shown in Figure 4-4, XRD analysis confirms that TiO_2-Krono and TiO_2-anatase samples consist of anatase phase, while TiO_2-rutile sample consists of rutile phase. TiO_2-P25 is the only sample consisting of both anatase and rutile phase, in the ratio 80% to 20%. As listed in Table 4-1, the calculated bandgap of TiO_2-P25, TiO_2-Krono, and TiO_2-anatase is around 3.2 eV. The calculated bandgap for rutile is around 3.0 eV, which is 0.2 eV narrower than the other commercial TiO_2 materials. Calculation of bandgap energy of the sample was presented in Figure S16.

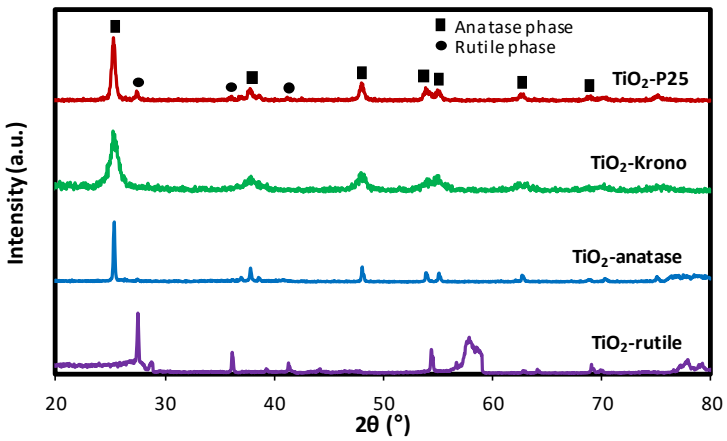

Figure 4-4: XRD spectra of TiO_2-P25, TiO_2-Krono, TiO_2-anatase, and TiO_2-rutile

Table 4-1 Properties of commercial TiO_2 materials

TiO_2 sample	Crystalline phase	BET-surface area (m^2/g)	Bandgap energy (eV)	Surface charge* (mV)
TiO_2-P25	80% Anatase 20% Rutile	46.9	3.23	33.20 ± 0.26
TiO_2-Krono	Anatase	252	3.25	20.00 ± 0.10
TiO_2-anatase	Anatase	8	3.22	-28.7 ± 2.21
TiO_2-rutile	Rutile	10	3.02	21.13 ± 0.38

* Measured in deionised water. Values are means ± standard deviation (n=3). Statistical significance differences (t test): $P < 0.01$.

The photocatalytic performance of various commercial TiO_2 nanoparticles was evaluated by degradation of methylene blue in an aqueous solution under visible light irradiation. The change of dye concentration was investigated at regular time intervals using an UV-vis spectrophotometer. To compare the adsorption capability, dark adsorption test was carried out before light activated degradation. As shown in Figure 4-5, the dye solution achieved adsorption equilibrium after 15 min under dark conditions. After dark adsorption test, most of the dye molecules obviously remained in the solution with TiO_2-P25, TiO_2-Krono, and TiO_2-rutile as the catalyst. This result indicates that the adsorption capability of these three catalysts was very low. In contrast, the concentration of dye solution dropped rapidly in first 15 min with TiO_2-anatase as the catalyst. A large amount of dye molecules, almost 50% of initial concentration, was adsorbed on the surface of TiO_2-anatase during adsorption test.

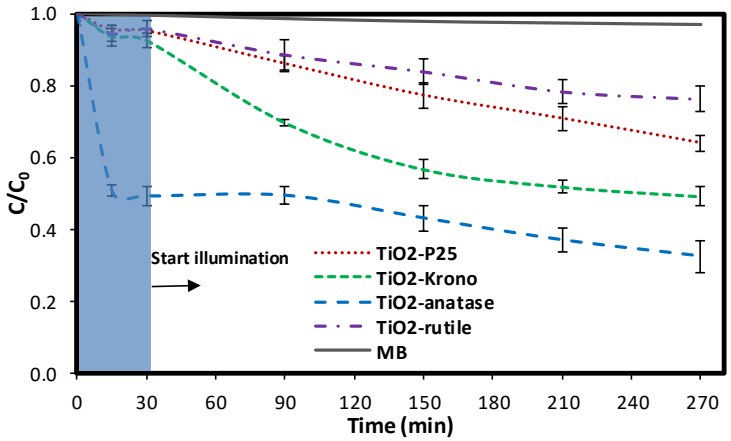

Figure 4-5: Photocatalytic performances of commercial TiO_2 products in the degradation of methylene blue in visible light

The interesting result has been identified by comparing the BET result with adsorption capability from each commercial product. Although TiO_2-anatase has the lowest surface area, this material showed the highest adsorption capability under dark conditions. The previous study demonstrated that surface charges of TiO_2 material play an important role in the adsorption process (Dai, 1994, Karaca et al., 2008, Butman et al., 2018). Electrostatic interactions between the organic dye and TiO_2 material have been shown to be an important factor controlling the interaction mechanism of contaminant/dye particles to TiO_2 surfaces. Therefore, the surface charge of commercial TiO_2 materials was measured using zeta potential analyser. The results in Table 4-1 showed that the TiO_2-anatase was more electronegative than other materials, supporting stronger adsorption capability with cationic dye of MB which is positively charged.

Following dark adsorption test, the photocatalytic activities of commercial TiO_2 particles were observed for degradation of dye in visible light. As shown in Figure 4-5, TiO_2-anatase displayed a highest total decrease in concentration of dye after 4 h visible light illumination. However, the decrease of dye concentration for TiO_2-anatase mainly occurred during adsorption process and was very slow during visible light exposure. On the contrary, total decrease in dye concentration for the other commercial products was highly controlled under visible light irradiation. Figure 4-5 shows that TiO_2-Krono generally outperformed other TiO_2 materials used in this study for degradation of dye in visible light. This result is predictable as TiO_2-Krono

is the only commercial TiO_2 with visible light activity according to manufacturer specification.

Photodegradation of methylene blue during visible light irradiation also shows interesting results. Considering the bandgap of various commercial TiO_2, it lies in the UV region which has no response in visible light. Further study was conducted to detect the oxidation power generated by means of RNO bleaching during light exposure. TiO_2-P25 showed high hydroxyl radical ($OH^{\bullet}$) production during UV/visible light irradiation, while no $OH^{\bullet}$ production was observed during visible light irradiation, as illustrated in Figure S19. This result indicates that under visible light irradiation the photon energy was not strong enough for electron excitation. As a result, commercial TiO_2-P25 could not produce hydroxyl radical under visible light irradiation.

It was suggested that the degradation of MB dye in visible light was ascribed to the dye photosensitization mechanism (Liu et al., 2014, Cabir et al., 2017, Mamba et al., 2014). In this procedure, MB molecule could absorb a visible light to generate electron-hole pairs. The excited electrons are then transferred from a singlet/triplet state of MB (MB*) into the conduction band of TiO_2 which further could react with oxygen, O_2, to produce O_2^- radicals (superoxide anion). The radicals generated could oxidize the aromatic rings of MB. The performance differences among commercial TiO_2 was mainly caused by their particle size and pore structure, which define active site available for photosensitization process. Due to high surface area and porosity, TiO_2-Krono and TiO_2-P25 provide more active site for reaction, resulting in a good photocatalytic performance.

4.3.2. Characterization of titanium dioxide modified with graphene oxide

TiO_2-P25 was then used for synthesis of a series of GO-TiO_2 composite and the composite products are then called GO-P25. The morphology of GO-TiO_2 prepared with 3% GO loading was observed with FESEM. The elemental analysis was then performed using EDX spectroscopy to identify the elemental composition in the composites. There is no significant difference between the morphology of GO-P25 (Figure 4-6(a)) and the morphology of pristine TiO_2-P25 materials (Figure 4-6(b)).

This finding is consistent with earlier studies (Jo and Kang, 2013, Liu et al., 2014) suggesting that the low ratio of GO in the composites did not make a significant alteration to the outward appearance of original TiO_2 particles. The EDX spectrum of GO-P25 (Figure 4-6(d)) exhibits peaks of Titanium (Ti), Oxygen (O) and Carbon (C) atoms. The presence of Ti and O atoms were ascribed to TiO_2 while the presence of C could be related to GO. Furthermore, elemental mapping (Figure 4-6 (e-g)) shows the uniform distribution of each element including smaller amount of C element corresponding to low percentage of GO in the composite.

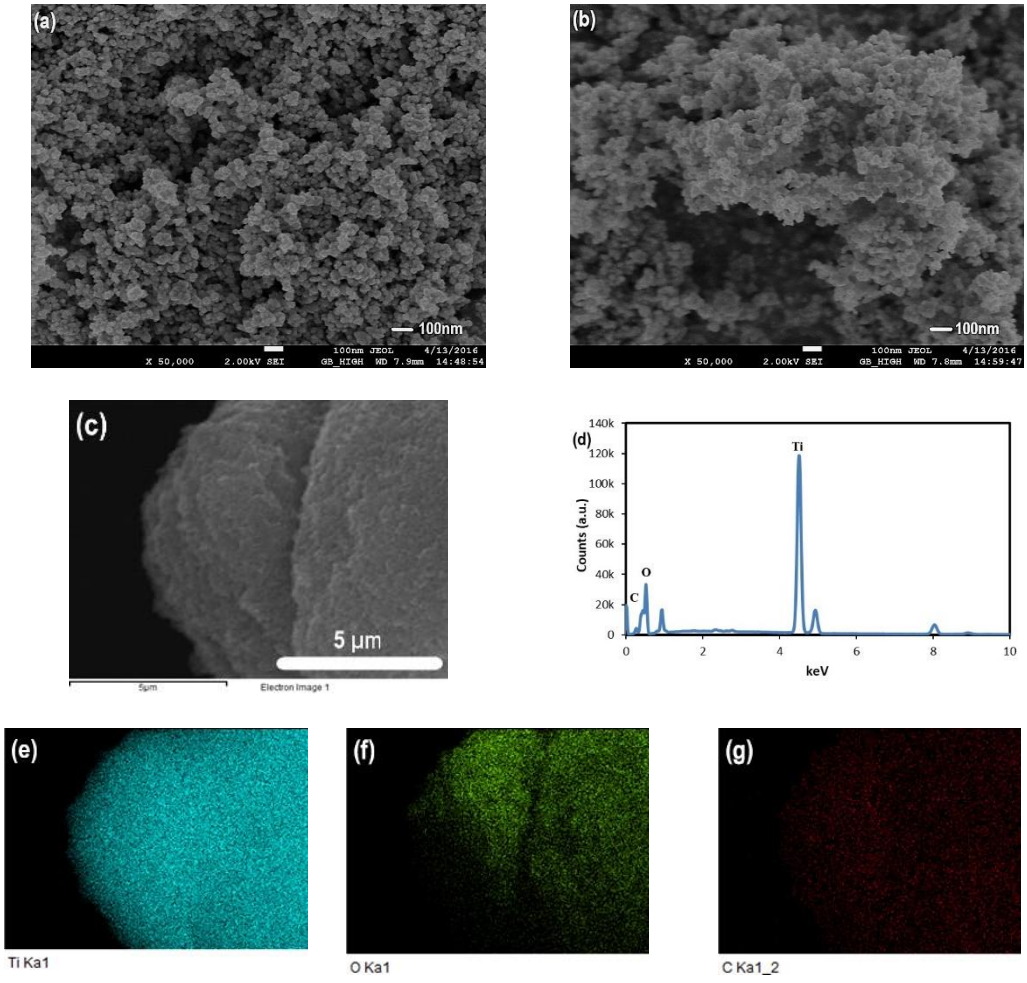

Figure 4-6: SEM images of (a) GO-P25, (b) TiO_2-P25, (c-g) EDX and elemental mapping of GO-P25

The percentage of GO in the composite was determined under dry air using the thermogravimetric analyzer (TGA). The TGA results generated on GO, TiO_2-P25 and GO-P25 nanocomposite is shown in Figure S20. The plot shows the percent mass as a function of sample temperature. The descending curves indicate a weight loss

occurred. The difference in weight loss between GO-P25 and P25 is about 2.0%. The TGA result for GO indicates 65.8% of weight loss. The percentage of GO content in the composite was estimated by calculating ratio among them, as shown below:

$$= \frac{\left(WL_{GO-P25} - WL_{TiO_2-P25}\right)}{WL_{GO}} x100\% \qquad (1)$$
$$= \frac{2.0}{65.8} x100\% = 3.0\%$$

The estimated GO contents in the composites are equivalent to the GO loading during the synthesis process. This finding indicates that GO content in the composites could be controlled during the synthesis process.

As thermal treatment in TGA is usually followed by an evolution of gases due to sample decomposition, coupling TGA with FTIR was conducted to identify the evolved gas components. Figure S21 shows the infrared spectrum of gases released directly from GO sample during thermal treatment. The evolved gas during heat treatment of GO corresponds to the CO_2 infrared spectrum. Hence, it was confirmed that the difference of weight loss between GO-P25 and TiO_2-P25 could be attributed to the decomposition of carbonaceous materials.

The interactions between GO and TiO_2-P25 are of great importance for the properties of GO-P25 composites. The previous study have indicated that coupling TiO_2 with GO did not alter the crystal structure of TiO_2 (Nguyen-Phan et al., 2011, Zhang et al., 2010a). The same XRD patterns were observed between pristine TiO_2-P25 and GO-P25 nanocomposite, as shown in Figure S22. These findings suggested that the absence of diffraction peaks for carbon species may be associated with the low amount of GO or low diffraction intensity.

Figure S23 shows the infrared spectrum of GO, TiO_2-P25 and GO-P25. The spectrum of graphene oxide at 1100 cm^{-1}, 1230 cm^{-1}, 1320 cm^{-1} and 1720 cm^{-1} were attributed to the presence of C-O, C-O-C, C-OH, and C=O stretching in carboxylic acids, respectively (Si and Samulski, 2008). Nevertheless, none of these peaks were observed in the GO-P25 spectrum. These oxygen-containing functional groups were probably removed during thermal process (Zhang and Pan, 2011). The pure TiO_2-P25

material displayed a low frequency spectrum at 690 cm^{-1}, which could be ascribed to the vibration of Ti-O-Ti bonds. However, in the GO-P25 composite, the broad adsorption below 1000 cm^{-1} was much higher than the corresponding peak in pristine TiO_2-P25 and shifted toward high wavenumber. The shift of such absorption curve could be assigned to the result of a combination between Ti-O-Ti and Ti-O-C vibration (798 cm^{-1}) (Nethravathi and Rajamathi, 2008, Sakthivel and Kisch, 2003, Zhang et al., 2010a). These results suggest that a chemical interaction between TiO_2 and GO may exist in the GO-TiO_2 composite materials due to the presence of Ti-O-C bonds.

The chemical state of elements in GO-P25 has been analyzed using XPS analysis. The XPS results are shown in Figure 4-7. According to the full-scale XPS spectra, as shown in Figure 4-7(a), GO-P25 composite contains graphitic C1s peak at 284.6 eV, O1s peak at 531.8 eV and Ti2p peak at 458.7 eV. In order to investigate the carbon states in the sample, the high resolution C1s spectra was measured as shown in Figure 4-7(b). Deconvolution of XPS spectrum is used to remove a specific type of signal such as noise from the observed signal. The procedures used a Gaussian response function with a Fourier deconvolution/filtering algorithm. Deconvolution of the C1s peak in the high resolution XPS spectrum shows two main separated peaks are existed for the GO-P25 composite at the binding energies of 284.6 and 286.8 eV. Generally, the binding energy of 284.6 eV could be either connected to a signal of adventitious elemental carbon contamination adsorbed from ambient or ascribed to a graphitic C-C bonds (Chen et al., 2010, Liu et al., 2014). The binding energy of 286.8 eV demonstrated the presence of Ti-O-C bonds as in other works (Zhang et al., 2010b, Zhang and Pan, 2011). This reveals that the C atoms substitute part of the Ti lattice point and form a Ti-O-C band structure. It confirms that C-atoms actually exist in the GO-P25, which is in good accordance with the previous SEM, TGA and FTIR analysis.

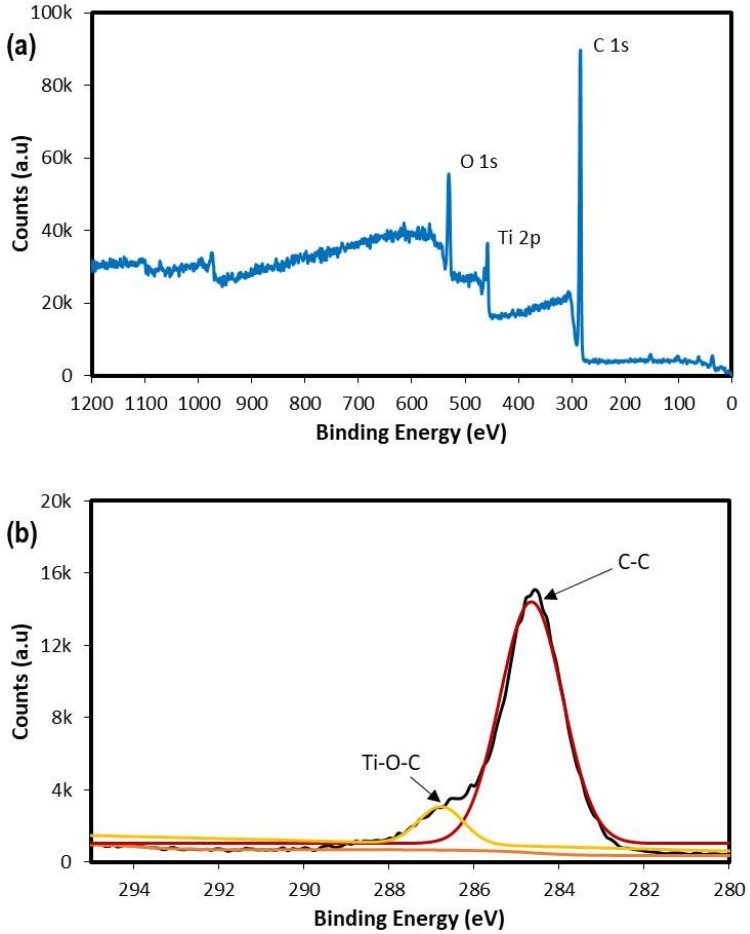

Figure 4-7: (a) The full XPS spectrum of GO-P25 and (b) High resolution XPS spectra of C1s for GO-P25 nanocomposites

The optical properties of TiO_2 based materials were determined using an UV-visible spectrophotometer equipped with diffuse reflectance accessory. The optical absorption spectrum and optical bandgap determination of TiO_2-P25 and GO-P25 are presented in Figure 4-8. The result showed that GO-P25 nanocomposite exhibited an obvious redshift in the absorption edge along with strong absorption in the visible light range. In contrast, TiO_2-P25 has no response in the visible light region. The optical absorption spectra of TiO_2-P25 displayed the absorption threshold at around 400 nm which is corresponding to UV region. This result indicates the bandgap narrowing upon the addition of GO in the GO-P25 nanocomposites.

The optical bandgap of the photocatalyst can be estimated from absorption spectra using Kubelka-Munk model and plotted using Tauc's relation, as shown below:

$$\alpha h\nu = const(h\nu - E_g)^2 \qquad (2)$$

where α, hν, and Eg represent the absorption coefficient of the materials, energy of adsorbed light, and optical bandgap of materials, respectively. Typically, the Tauc's plot shows the relationship between light energy (hν) on the abscissa and modified Kubelka-Munk function $(\alpha h\nu)^{1/2}$ on the ordinate. The energy gap can be obtained from the intercept of the resulting straight lines with energy axis at $(\alpha h\nu)^{1/2} = 0$. As shown in Figure 4-8, GO-P25 composite material has narrower bandgap and exhibit stronger absorption in the visible light range (< 3.2eV) than that of pristine TiO_2-P25. The bandgap narrowing for GO-P25 can be assigned to the formation of Ti-O-C bond in the GO-TiO_2 composite surface which is in agreement with the FTIR and XPS result. Further, their performances in organic dye degradation and *E. coli* decomposition will be compared under visible light irradiation.

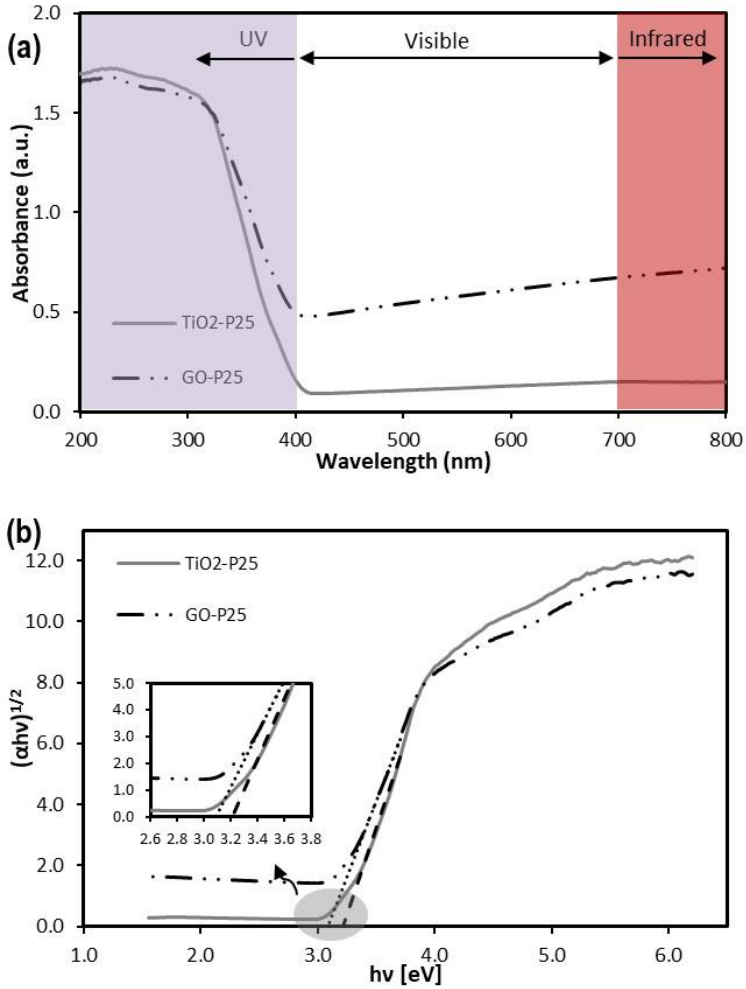

Figure 4-8: (a) Optical absorption spectrum of TiO_2-P25 and GO-P25 and (b) Optical bandgap determination of TiO_2-P25 and GO-P25

4.3.3. Evaluation of photocatalytic performance

Adsorption capability

The adsorption capability is one of the important factors influences the overall photocatalytic efficiencies (Fujishima et al., 2008, Xiaobo and Mao, 2007, Nguyen-Phan et al., 2011, Zhang et al., 2010a). Therefore, investigation of methylene blue adsorption was carried out before starting the irradiation. The purpose of adsorption test is to study the effect of combination of GO and TiO_2 on the adsorption capability. In a typical procedure, the photocatalyst powder was dispersed in methylene blue solution. The solution was then kept in the dark with incessant stirring for 30 min to reach the adsorption equilibrium. The UV absorption spectra of methylene blue after adsorption test are shown in Figure 4-9. Methylene blue solution is an aromatic

chemical compound with maximum absorption of light around 664 nm. As shown in Figure 4-9, the great decrease of peak intensity at 664 nm was observed for a solution containing GO-P25 materials.

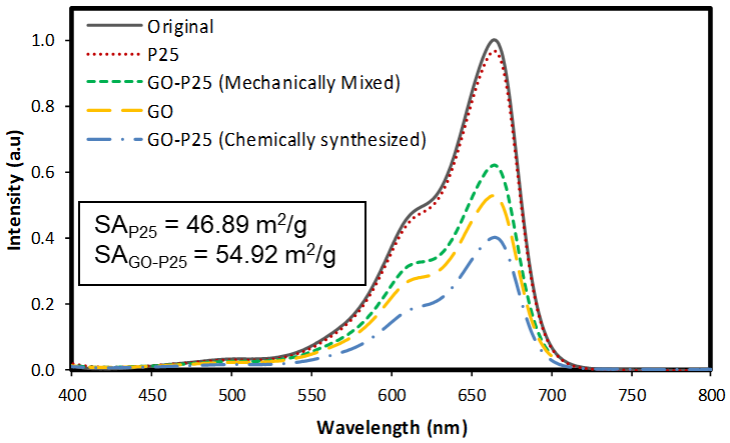

Figure 4-9: UV absorption spectra of methylene blue after adsorption test

This result indicates that the amount of methylene blue dye adsorbed by GO-P25 composites materials was remarkably increased compared to the pristine TiO_2-P25. Approximately 60% and 40% of the initial dye was adsorbed by GO-P25 prepared through chemical synthesis and mechanical mixing, respectively, while only less than 10% of the initial dye was adsorbed by pristine TiO_2-P25. This result suggests that GO plays an important role during adsorption process. In general, the adsorption capability could be enhanced by increasing GO content. However, the excessive GO content could hinder the adsorption of oxygen on the surface of active site. As a result, in the absence of oxygen, the injected electron at conduction band of TiO_2 could recombine, potentially leading to a great decrease of photocatalytic activity. Hence, it is suggested that there should be an optimum amount of GO in the GO-TiO_2 nanocomposite materials for the efficiency of photodegradation process (Liu et al., 2014, Pastrana-Martínez et al., 2012, Wang and Zhang, 2011).

The enhancement of adsorption capability was generally attributed to the increase of specific surface area (Pastrana-Martínez et al., 2012, Zhang and Pan, 2011). However, in this case, surface area improvement was not significant compared to the increase of adsorption capability. According to BET result (Table S1), the increase of specific surface areas was only around 17% (SA_{P25} = 46.89 m^2/g and SA_{GO-P25} =

54.92 m^2/g) whereas adsorption capability greatly increased from 10% to 60%. This finding is consistent with earlier studies suggesting that the reason for the enhanced adsorption capability is not only due to the increase of specific surface area but also due to the non-covalent interactions (π-π interaction) between graphene layer and methylene blue dye (Zhang et al., 2010a). The electrostatic interaction between methylene blue dye (+11.3 mV, cationic dye) and the surface of Graphene Oxide (-7.87 mV, negatively charged) has a significant effect on increasing adsorption capacity.

Dye degradation

Figure 4-10 presents the photodegradation of methylene blue over TiO_2-P25, TiO_2-Krono, and GO-P25 under visible light irradiation. GO-Krono was also added to compare the effectivity of synthesis process for different TiO_2 materials. It was obvious that the combination of GO and TiO_2 significantly enhance the photodegradation of the dye compared to pristine TiO_2-P25 and TiO_2-Krono, as shown in Figure 4-10. For the GO-P25 composite materials, 94% of the initial dye was degraded after 1-h irradiation; on the contrary, only 36 % of the initial dye was decomposed by TiO_2-P25 even with longer irradiation time, 4-h. Since TiO_2-P25 has no optical absorption in the visible light region, as described earlier, the discoloration was mainly attributed to the dye sensitized photodegradation of methylene blue (Liu et al., 2014). Photocatalytic activity of TiO_2-Krono in visible light was better than that of pristine TiO_2-P25 where 51% of the initial dye was degraded after 4-h irradiation. After coupling with GO, the degraded dye increased up to 87% of the initial dye after 2-h irradiation, which is much higher than the pure TiO_2-Krono. In the absence of photocatalyst, approximately 3% of the methylene blue was decomposed due to direct photolysis of the dye.

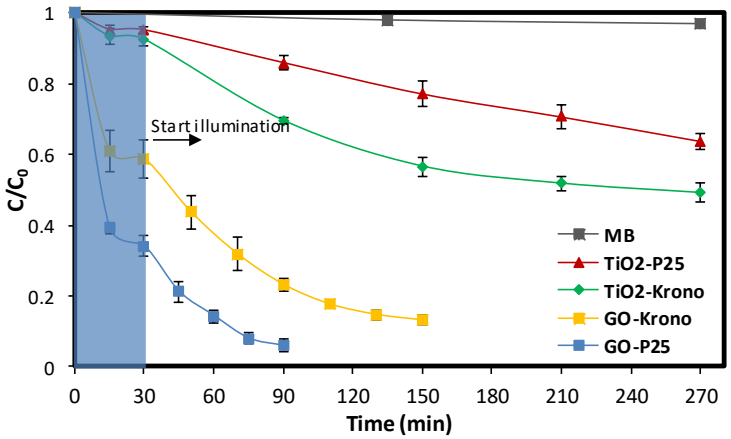

Figure 4-10: Photodegradation of methylene blue over TiO_2-P25, GO-P25, TiO_2-Krono and GO-Krono under visible light irradiation

Figure 4-11 display the reaction rates for photodegradation of methylene blue on the GO-TiO_2 composite systems. The photocatalytic reaction rate for TiO_2 and GO-TiO_2 was described by the first order kinetic model. All linear models have R-squared values close to unity. Figure 4-11 clearly displays a great improvement in the degradation rate for GO-TiO_2 compared to pristine TiO_2. GO-P25 shows the best in degradation of methylene blue, giving the highest reaction rate of 0.0299. This gives a reaction rate that is approximately 19 times that of P25. While the reaction rate of GO-Krono is around 0.0134 which is approximately 5 times greater than that of Krono.

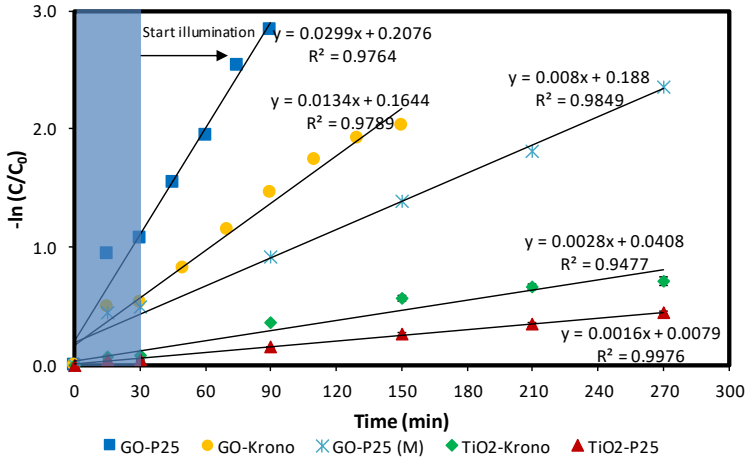

Figure 4-11: Degradation rate for pristine TiO_2 and GO-TiO_2 composite

This excellent photocatalytic performance for GO-TiO_2 nanocomposite materials can be attributed to the following factors. Initially, the dye was highly adsorbed on the surface of graphene to reach adsorption equilibrium. Under visible light irradiation, graphene acts as sensitizers to absorb photon (Chen et al., 2010, Du et al., 2011). Following photon absorption, an electron could be transferred from the excited state of GO into the conduction band of TiO_2 leaving the accumulation of holes in the graphene layer (Du et al., 2011). Then, the created electron-hole pairs become well-separated. These processes could significantly suppress the charge recombination. Subsequently, the electron is transferred to oxygen adsorbed on the semiconductor surface producing superoxide anion (O_2^-) which can facilitate the degradation of organic components (Figure 4-14). Photodegradation process broke the adsorption equilibrium and more dye would transfer from the solution to the interface (Nguyen-Phan et al., 2011, Zhang et al., 2010a). The process is iterated until all the dye is fully decomposed into CO_2, H_2O and mineral acids. The synergetic effect between adsorption strength and photodegradation is a key factor in excellent photocatalytic performance of GO-TiO_2 nanocomposite materials.

As a control, the degradation performance of GO was also observed to exclude the impact of GO during photodegradation process. In the presence of GO, the concentration of dye remained unchanged after achieving adsorption equilibrium, suggesting that the GO alone did not show photocatalytic activity (Figure S27). Furthermore, GO-TiO_2 was also prepared by mechanical mixing. The GO-TiO_2 mixture obtained by a simple mechanical mixing was compared to the GO-TiO_2 activity prepared by a chemical synthesis method. It was found that although the adsorption of MB dye increased significantly for both composite and mixture materials, the degradation process of GO-P25 (M) prepared by mechanical mixing was much slower than that of GO-TiO_2 prepared by chemical synthesis (Figure 4-11). This indicates that there may be no synergistic action in mechanically mixed GO-TiO_2 and most likely significant percentage of the MB was just adsorbed rather than degraded.

Escherichia coli disinfection

Considering the good adsorption capabilities and high activity on MB degradation under visible light for GO-P25 nanocomposite materials, anti-bacterial performances of such composite materials are expected to be improved than that of pristine TiO_2. After 60-min incubation with nanocomposite materials (Figure 4-12), the bacteria were significantly killed. The total number of the bacteria was reduced by around 77% after 60-min incubation with GO-P25 (Figure 4-12). However, the total number of bacteria was only reduced by around 20% for the control group (no TiO_2 addition, Figure 4-12). As a result, the GO-P25 has the most significant effect in antibacterial test.

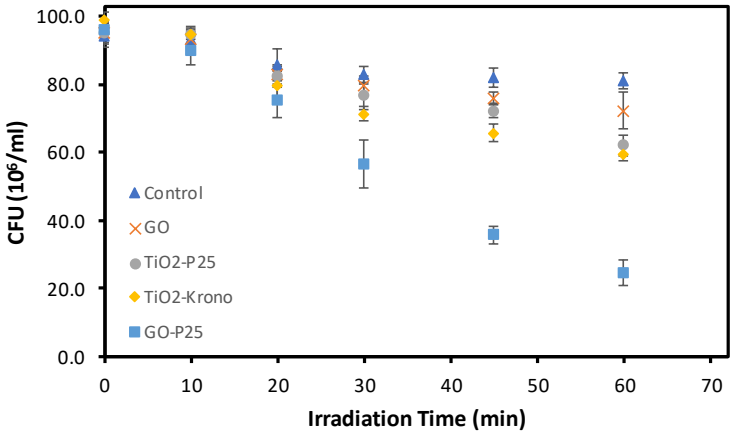

Figure 4-12: Colony Forming Unit (CFU) test during 60-min incubation with different nanocomposite materials

Field emission scanning electron microscopy (FESEM) and fluorescence spectroscopy were carried out to investigate whether the E. coli cells were really decomposed during photocatalytic treatment. Figure 4-13 shows the FESEM image and fluorescence image of bacteria decomposition under visible light irradiation with the presence of GO-TiO_2 photocatalyst. It was found that the decomposition of bacterial cells can be achieved in a relatively short time (1 hr visible light irradiation). The antibacterial effect of GO-P25 nanocomposite materials was also observed in previous studies (Joost et al., 2015, Zimbone et al., 2015).

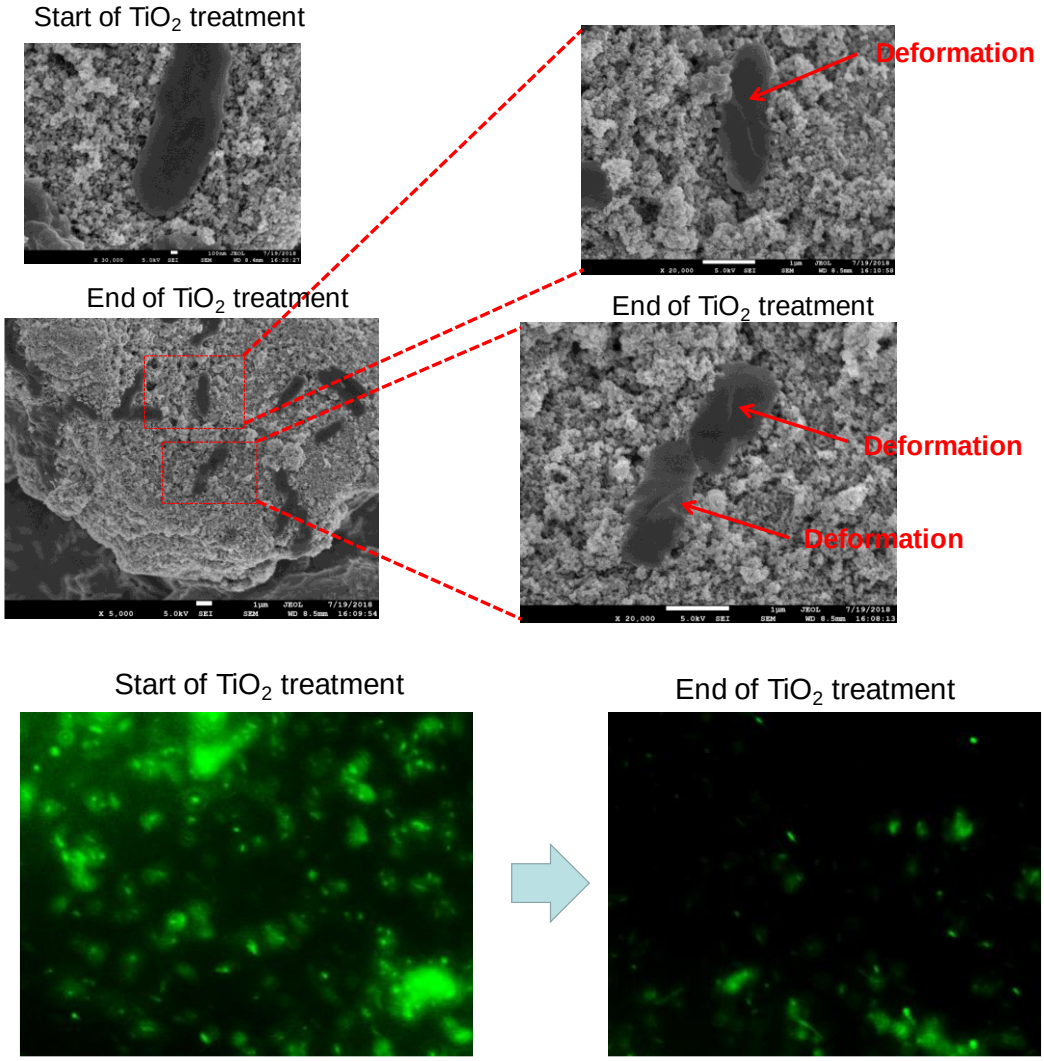

Figure 4-13: (a) FESEM image and (b) fluorescence image of the decomposition of E. coli under visible irradiation on GO-TiO_2 photocatalyst

Antibacterial GO-P25 nanocomposite materials were highly important because it might have good potential in the application for future hospital construction materials. There were many Hospital-Acquired Infection (HAI) cases all over the world. The pathogenic bacteria coming from infected patient attached to the surfaces of cementitious materials and transferred to another healthy person afterward, which leading to the HAI (Leung and Chan, 2006) case. As a result, the construction materials with antibacterial effects are strongly needed and might have great potential in future hospital construction.

A preliminary study was conducted to evaluate the effectiveness of GO-TiO_2 application in cement-based construction materials for disinfection of *E. coli*. The

experimental procedure for the surface study on anti-bacterial concrete is presented in Figure S28. After 24-h UV/vis light irradiation, 1 ml of *E. coli* suspension was then applied evenly on the cement surfaces using an adjustable precision pipette. The bacteria survival was estimated on agar dish after 24-h incubation. The bacteria growth can be visually seen by observing the center part of agar dish which is in contact with cement surface (Figure S29). Cement sample with 5% GO-TiO_2 loading has the best anti-bacterial activity compared to cement sample without TiO_2 and/or with 5% TiO_2-P25. Under visible light irradiation, the injected electron from excited state graphene layer to TiO_2 conduction band can induce the reduction of molecular oxygen (O_2) to form the superoxide anion (O_2^-) (Du et al., 2011), as illustrated in Figure 4-14. It was suggested that superoxide anion could damage iron-sulphur protein such as aconitase (Imlay, 2003, Daly et al., 2007). Aconitase is an enzyme that catalyses the interconversion of citrate and isocitrate, which is a series of chemical reactions in the Citric Acid Cycle, that is crucial to aerobic cellular respiration.

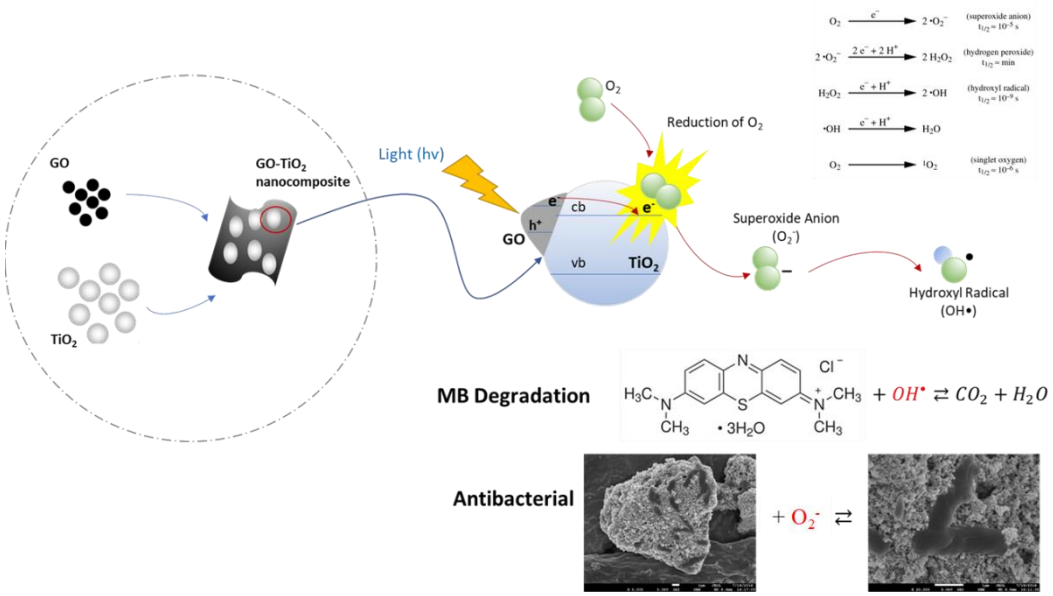

Figure 4-14: Photocatalytic mechanisms of dye degradation and antibacterial effect under visible light on GO-TiO_2 nanocomposites

4.4. Summary

In this study, visible light activated graphene based TiO_2 nanoparticle composites were synthesized through a simple mixing method. It was found that the GO-TiO_2 nanocomposite materials possessed strong optical response in the visible light region. The visible light response of GO-TiO_2 nanocomposite materials could be assigned to the formation of Ti-O-C bond on the surface of GO-TiO_2 nanocomposite materials. In addition, the combination of GO and TiO_2 in the GO-TiO_2 composite significantly increased the capability of adsorbing the methylene blue dyes compared to the pure TiO_2 materials. Consequently, their photocatalytic activity was greatly improved in the degradation of methylene blue under visible light irradiation. GO modified TiO_2 sample show high antibacterial activity compared to pristine TiO_2. The preliminary study on application of GO-TiO_2 into cement-based construction materials confirms the effectiveness of the composites for disinfection of *E. coli* under visible light. This finding is of considerable importance since it suggests that the simple synthesis process still provides remarkable improvement in the photocatalytic activity.

Chapter 5. Antibacterial potential of cementitious materials containing GO-TiO_2 nanocomposites for self-sterilization surface

5.1. Overview

Development of cement-based materials containing TiO_2 photocatalyst materials is one of the active research areas in the field of innovative and smart construction materials, and yet it holds the key to broaden the advantage of photocatalysis technologies. The use of cement-based construction materials as TiO_2 supporting media on exterior building, tunnelling and road related facilities provide a massive amount of surface area available for photocatalytic reaction (Fujishima and Zhang, 2006, Guerrini, 2012, Ohama and Van Gemert, 2011). Moreover, advanced functional construction materials, for example self-cleaning, water detoxification, anti-microbial, and air pollutant removal, could be achieved by incorporating TiO_2 materials into cementitious composite (Guo et al., 2017, Rastogi and Vaish, 2016, Sikora et al., 2017, Yang et al., 2017).

Such advanced function is induced by light-activated TiO_2: the presence of TiO_2 in cement-based materials can absorb the sunlight energy, generating an electron-hole pairs (e^- and h^+). The holes (h^+) trapped at the TiO_2-based surface can react with adsorbed water molecule (OH^-) to generate hydroxyl radical ($OH^\bullet$) while the excited electron could induce the reduction of molecular oxygen (O_2) to form the superoxide anion radical (O_2^-) (Hoffmann et al., 1995, Kamat, 1993, Linsebigler et al., 1995). These molecules are powerful oxidant in the chain reaction for breaking down the organic pollutant attached into TiO_2-based surface completely into harmless final product. However, due to wide bandgap of TiO_2, the application of TiO_2 photocatalyst is limited to outdoor environment as it can only be activated by ultraviolet (UV) radiation. In order to expand its use in indoor application, different attempts to improve the optical response of TiO_2 towards the visible light spectrum have been carried out. Surface modifications of TiO_2 with carbonaceous materials such as graphene oxide (GO) have received great attention nowadays due to its excellent photocatalytic activity in the visible light (Chen et al., 2010, Chen et al.,

2009, Du et al., 2011, Lettmann et al., 2001, Morales-Torres et al., 2012, Nguyen-Phan et al., 2011, Zhang et al., 2010a, Cruz-Ortiz et al., 2017).

This work aims to investigate the photocatalytic efficiency of GO-TiO_2 nanocomposites intermixing with cementitious materials under visible light irradiation. The new GO-TiO_2 based photocatalysts will have much wider light absorption range and radically improve performances under low light intensity conditions. The outcome of this work could be useful for construction of microbiologically sensitive place such as healthcare facilities (indoor application). Under visible light irradiation, graphene oxide (GO) acts as light absorbing sensitizers (Chen et al., 2010, Du et al., 2011) which can transfer the energy to TiO_2 host and induce a chemical reaction. Due to its high degree of micro-porosity, GO also acts as an adsorbent in the photocatalysis. It is therefore hypothesized that incorporating this novel photocatalyst into cementitious material will contribute to wider application of photocatalyst in construction industry with following advantages: (a) enhanced visible light responsiveness, (b) strong adsorption of contaminants, and (c) improve the photocatalytic efficiency under visible light.

5.2. Methodology

5.2.1. Materials

In this study, white cement (Aalborg Portland Malaysia) was used as the cementitious materials. Two commercial titanium dioxide catalysts were used for this test: Aeroxide TiO_2 P25 (Evonik, Germany) and KRONOClean 7000 (KRONOS, USA). Commercially available graphene oxide was purchased from HENGQIU Technologies, China. Rhodamine B (RhB) for photodegradation of dye was obtained commercially from Sigma-Aldrich, Singapore. Bacteria *E. coli* K-12 obtained from the bacterial library in the environment laboratory of Nanyang Technological University was used for antibacterial test.

5.2.2. Synthesis of GO-TiO_2 nanocomposite

The GO-TiO_2 composites were prepared using the commercial GO and TiO_2 (Aeroxide P25 and Kronoclean 7000) via a one-step hydrothermal process based on the work of Zhang et al. (2010a) with modifications. In detail, 30 mg of GO was

dissolved in 60 ml of distilled water by ultrasonic treatment for 30 min. In the meantime, 0.97 g of TiO_2 was dispersed in 140 ml of distilled water and then stirred continuously for 30 min at room temperature (≈ 23-25 °C) using magnetic stirrer at 160 rpm. The GO was subsequently added to the obtained GO solution and stirred for another 1 h to get homogeneous suspension. The suspension was then stirred at 150° C for 10 h and placed in the oven for 24 h at 60° C.

5.2.3. Parametric study

This parametric study statistically determines the significance of the governing factors such as TiO_2-type, TiO_2-loading, and mixing procedure on photocatalytic efficiencies. Although the effect of these factors on photocatalytic activity have been well studied, only a few numbers have reproduced consistent result. This section offers a statistically significant relationship between such factors and photocatalytic activity.

A special and simplest 2^k experiment was adopted to design the factor screening experiments which is useful in the early stage when the factors with significant effect are uncertain. The 2^k factorial design refer to experimental design with k factor in which each factor has just two levels. This method can significantly reduce the number of runs in an experiment for given number of factors, therefore, lower test is required to statistically study the effect and interaction among each factor. RhB degradation was selected as photocatalytic response for this experimental design. The response from different factors was investigated by measuring their relative colour change (ΔC) of RhB dye applied on the surface of cement sample under UV illumination.

Table 5-1 show the total number of mixtures with coded factors for all variables considered in the experiment. The photocatalytic response was analyzed statistically by its variance (ANOVA) and calculated *F*-ratio (test of significance).

Table 5-1 Coded factor for variables

Mixture No	Coded Factors			Labels		Factor Levels	
	A	B	C			Low (-)	High (+)
1	-	-	-	(1)	A	GO-Krono	GO-P25
2	+	-	-	a	B	3%	6%
3	-	+	-	b	C	Dry	Wet
4	+	+	-	ab			
5	-	-	+	c			
6	+	-	+	ac			
7	-	+	+	bc			
8	+	+	+	abc			

For mixing procedure, in the case of wet method, GO-TiO_2 was mixed with distilled water using a probe sonication for 10 min to obtain homogeneous GO-TiO_2 suspension. The cementitious material was then added and hand mixed with GO-TiO_2 suspension for 5 min. After mixing, cement pastes were cast in 60 mm diameter and 15 mm thickness moulds. Three cement discs were prepared for each set. The prepared samples were cured for 28 days at room conditions before tests. In the case of dry method, GO-TiO_2 and cementitious material were firstly manually mixed as dry powders. After that, the distilled water was added and manually mixed for 10 min. After mixing, the subsequent processes are similar to wet method described earlier.

5.2.4. Photocatalytic experiments

The photocatalytic performance under visible light irradiation was investigated by disinfection of *Escherichia coli (E. coli)* at room temperature (≈ 23-25 °C). Before each experiment, bacterial strains and growth media was prepared. Briefly, the *E. coli* K-12 was used as bacterial strain and obtained from bacterial library in the environment laboratory of Nanyang Technological University. *E. coli* was grown at 37° C in a liquid nutrient medium (Difco™ LM Broth, Miller (Luria Bertani)) for 24 h. After incubation, concentration of the culture was adjusted by dilution to reach the same initial concentration for all groups.

E. coli disinfection experiments were carried out using a PTFE beaker of 250 ml as a batch reactor. A 500 W long arc xenon lamp with an UVIRCUT 420 optical filter was used as the visible light source providing a light intensity of 20k lux at the surface

of the sample. The cement samples containing various TiO_2 materials (P25, GO-P25 and Kronoclean 7000) were firstly autoclaved to sterilize it. Subsequently, the samples were exposed to *E. coli* suspension and kept in contact with bacteria environment under dark conditions for 30 min to reach adsorption equilibrium. The system was then irradiated with visible light to investigate the photocatalytic efficiency. The viable bacteria was evaluated at regular interval of time by growing it in Luria Bertani (LB) agar plates followed by a series of dilution, as shown in Figure 5-1. The colony forming unit were examined after 24-h incubation at 37 °C. Two control experiments were conducted, which consisted of reaction in the absence of photocatalyst or in the absence of light source (dark condition).

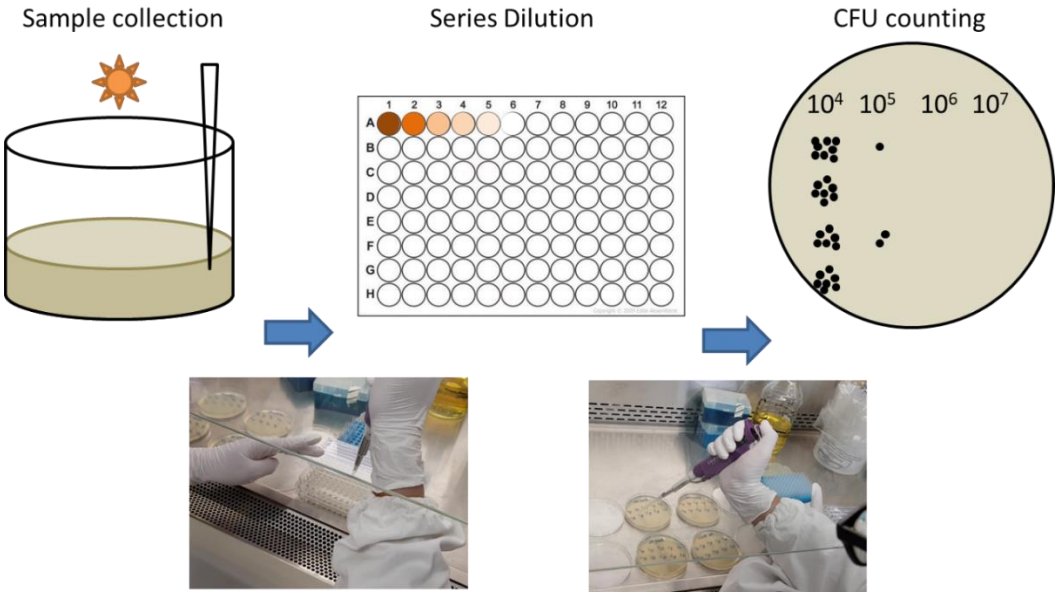

Figure 5-1: Antibacterial examination method

5.2.5. Characterization of materials

UV-vis absorption spectra of cementitious materials with and without TiO_2-based photocatalyst were analyzed using an ultraviolet-visible (UV-vis) spectrophotometer (Shimadzu UV-2600) equipped with diffuse reflectance accessory. Surface properties of the samples was evaluated by water contact angle test using video contact angle system (VCA Optima, AST). The objective of this test is to study the wettability of the surface of cement samples after UV-visible light treatments.

5.3. Result and discussion

5.3.1. Factors governing photocatalytic performance

This section focuses on understanding the factors affecting photocatalytic efficiency. A 2^k factorial design was used to develop photocatalytic cementitious materials in which each factor was run at two level. Different cement pastes were prepared by varying several factors such as type of TiO_2 particles, the amount of TiO_2 particles and procedures of mixing process. The response on photocatalytic performance from different factors was investigated by measuring their relative colour change (ΔC) of RhB dye applied on the surface of cement sample. Table 5-2 presents the test result (response data) obtained from two replicates of the 2^3 experiment.

Table 5-2 RhB test result (response data)

Mix No	RhB Colour Change (ΔC)		Total	Average
	Replicate 1	Replicate 2		
1	82.5%	76.1%	159%	79.3%
2	58.8%	43.6%	102%	51.2%
3	50.8%	58.8%	110%	54.8%
4	55.9%	64.4%	120%	60.1%
5	81.6%	75.4%	157%	78.5%
6	38.7%	53.1%	92%	45.9%
7	31.8%	55.1%	87%	43.5%
8	25.5%	50.6%	76%	38.0%

It is essential to estimate the magnitude and direction of the factor effect to determine which variables are likely to be important, as presented in Table 5-3 (the column labelled "Effect Estimation"). A positive effect means that the response will be greater when the factor is at the high level while the larger magnitude of the effect means that its influence on the response is higher, no matter the effect is positive or negative. For example, the effect of A (TiO_2 type) is negative; this suggests that the use of GO-P25 (high level) will decrease the value of ΔC. The lower value of ΔC indicates the colour degradation of the cement specimen containing TiO_2 is greater, which means the colour difference is more obvious than that of the initial intensity. In terms of magnitude, the largest effects are for TiO_2 type (A = -15.2%), TiO_2 loading (B = -14.6%) and the TiO_2 type-loading interaction (AB = 15.1%).

Furthermore, the column labelled "percent distribution" measures the percentage of contribution of each model term relative to the total sum of squares. The percentage contribution is often a rough but effective guide to the relative importance of each model term. Note that the main effect of A, B and interaction of A and B dominates this process. The main effect of A, B and the AB interaction account for about 22%, 20% and 22%, respectively. Although the aforementioned interpretations can give rough estimation on the importance of factors and their interaction, the information from the effect estimation and percent contribution only has relative or comparative meaning and cannot give the confidence level as in ANOVA. ANOVA is the most important statistic tool used in DOE. Its task is to decide whether and which factors or interactions have significant effect (influence) on the response.

Table 5-3 Analysis of variance for RhB test

Source of Variation	Effect Estimation	Sum of Square	DoF	Mean Square	F_0	Percent Contribution
TiO_2 type (A)	-15.2%	9.22%	1	9.22%	8.101	22%
TiO_2 loading (B)	-14.6%	8.55%	1	8.55%	7.510	20%
Mixing method (C)	-9.9%	3.90%	1	3.90%	3.425	9%
AB	15.1%	9.18%	1	9.18%	8.065	22%
AC	-3.8%	0.59%	1	0.59%	0.514	1%
BC	-6.8%	1.86%	1	1.86%	1.633	4%
ABC	-1.6%	0.10%	1	0.10%	0.085	0%
Error		9.10%	8	1.14%		
Total		42.48%	15			

F test presented in Table 5-3 may be used to confirm such interpretation. The control value $F_{\alpha,v1,v2}$ is determined from the F distribution Tables, where, α is a type I error rate (significance level) which is set to 0.05; v_1 is the D.O.F of the factor (or the interaction); v_2 is the D.O.F of the error. Hence, based on the F distribution Tables, the control limit $F_{\alpha, v1, v2} = F_{0.05,1,8} = 5.32$. By comparing the calculated F_0 value against the control limit, F_0 for factor A, B, and interaction AB is larger than the control limit. As a result, TiO_2 type and TiO_2 loading are highly significant on the photodegradation

of Rhodamine B dye while the effect from mixing procedure was considered not significant.

Furthermore, it was revealed that there is a significant effect from AB interaction, which means TiO_2 type has a strong interaction with TiO_2 loading. Figure 5-2 show this phenomenon, which suggests the response is very sensitive to TiO_2 content when GO-Krono is used as photocatalyst but much less pronounced when GO-P25 is used. As many experiments involve more than two levels of factor, it is necessary to design an experiment with focus on factors that have significant effect with arbitrary number α levels of the factor. Further, cement-based samples mixed with different TiO_2 type such as GO-P25, Krono, and P25 (one significant factor with four levels, including control specimen) were used for antibacterial study under visible light irradiation.

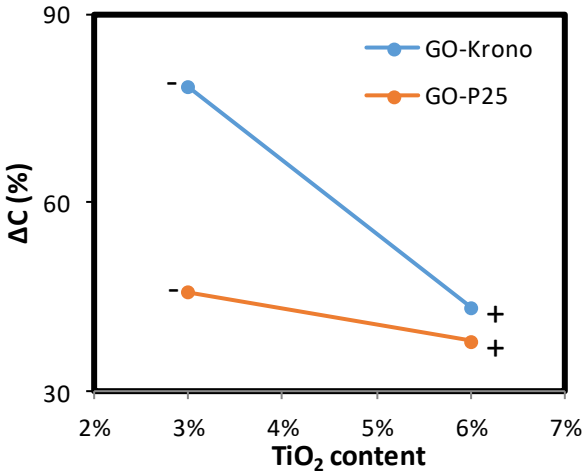

Figure 5-2: The interaction between TiO_2 type and TiO_2 content

5.3.2. Antibacterial activity of cement-based construction material containing GO-TiO_2 nanocomposite

The antibacterial efficiency of cementitious materials containing different type of TiO_2-based photocatalysts is evaluated, including control specimens. The TiO_2 material used were P25, Krono, and GO-P25. The study compared the efficiency of each material in destroying *E. coli* since it is one of organisms causing Hospital Acquired Infection (HAI). Reactive oxygen species (ROS), such as hydroxyl radical ($OH^{\bullet}$), hydrogen peroxide (H_2O_2), and superoxide anion (O_2^-), generated by light activated TiO_2 are cytotoxic and highly reactive. The production of ROS can damage

the DNA of *E. coli* and inhibits the activities of particular enzyme that is crucial for cell growth (Lemire et al., 2013, Moritz and Geszke-Moritz, 2013). Hence, the developed materials can potentially be used as self-sterilization surface in the construction of hospital and health care facilities.

Figure 5-3 shows the result of antibacterial test for different sample under visible light irradiation. The viability of *E. coli* is estimated by bacterial counting method on agar plates and expressed in logarithmic scale. The application of visible light on *E. coli* strain did not affect the viability of living cell in the absence of TiO_2 (control specimen). Furthermore, no antibacterial effect was detected for specimens with TiO_2 under dark condition while the reduction of cellular viability was identified only in the specimens with TiO_2 and exposed to light treatment. The loss of cell viability has a direct relationship with the duration of light exposure, and longer exposure time results in a significant decrease of survival ratio. The loss is escalating from 2 orders of magnitudes to 8 orders for the specimen with novel GO-P25 when the irradiation time increased from 120 min to 200 min. In contrast, bactericidal efficiency of the specimens with P25 and Krono is very small, displaying only two orders of reduction of living cells during the total irradiation time of 200 min.

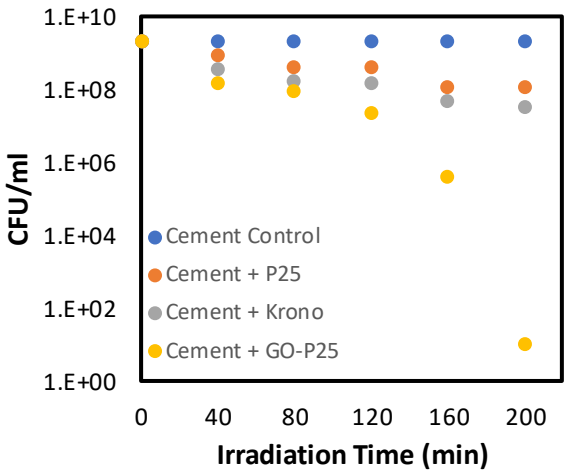

Figure 5-3: *E. coli* inactivation on TiO_2-based cement surfaces under visible light irradiation

As shown in Figure 5-3, the process of *E. coli* inactivation was very slow at earlier stage. It was suggested that the slow reaction at early stage can be related to mass transfer effect that influence the initial attachment of bacteria on cement-based

surface. Immobilization of TiO_2 into cementitious materials limits the diffusion of reactant molecules (bacteria in this case) from the bulk to the active site in the pore of cement surface (Klaewkla et al., 2011). Consequently, the mass transfer resistance becomes one of the important factors on the antibacterial processes. Another possible explanation is the ability of microorganism to adapt and resist to toxic species. Bacteria such as *E. coli* has a defense mechanism to protect the redox-sensitive cellular molecules from the detrimental effect of ROS. Antioxidant systems, chaperones (protein), and catalase (enzymes) involve as a defense system for bacteria to decrease the concentration of hydrogen peroxide (H_2O_2) and superoxide anion (O_2^-) (Harrison et al., 2009, Gogniat and Dukan, 2007). Finally, it will limit the generation of hydroxyl radical ($OH^\bullet$) and suppress the bactericidal activity at the early stage.

Natural existence of defense mechanism against ROS indicate that the production of reactive oxygen species is an unavoidable aspect of life under aerobic condition (Carre et al., 2014, Lemire et al., 2013, Lushchak, 2010). However, the presence of light activated TiO_2 may disturb the balance between production and elimination of ROS, leading to a severe cell damage. Previous study reported that the generated ROS initially attack the cell wall membrane and cause detachment of cell wall (Kiwi and Nadtochenko, 2005, Lemire et al., 2013). Longer irradiation time is needed to induce disruption of cytoplasmic membrane followed by DNA and protein damage that are leading to cell death (Carre et al., 2014, Daly et al., 2007, Endo et al., 2018). For further light exposure, the increase of dead cell might block the active site until the antibacterial activity had reached a plateau. This plateau corresponds with the saturation condition in the bactericidal activity.

The viability of *E. coli* can be visually seen by observing the number of colonies forming in the agar plates. It is clear that the number of CFU was almost negligible (8 orders of decrease) for cement sample containing GO-P25 after 200 min of visible light irradiation (Figure 5-4(d)) whereas the number of CFU was around 2 and 3 orders of decrease for cement samples mixed with P25 and Krono (Figure 5-4(b) and Figure 5-4(c)), respectively. No antibacterial effect was observed for control specimen under visible light irradiation. This evidence proved the hypothesis that GO-P25 successfully extend its photoactivity to the visible region.

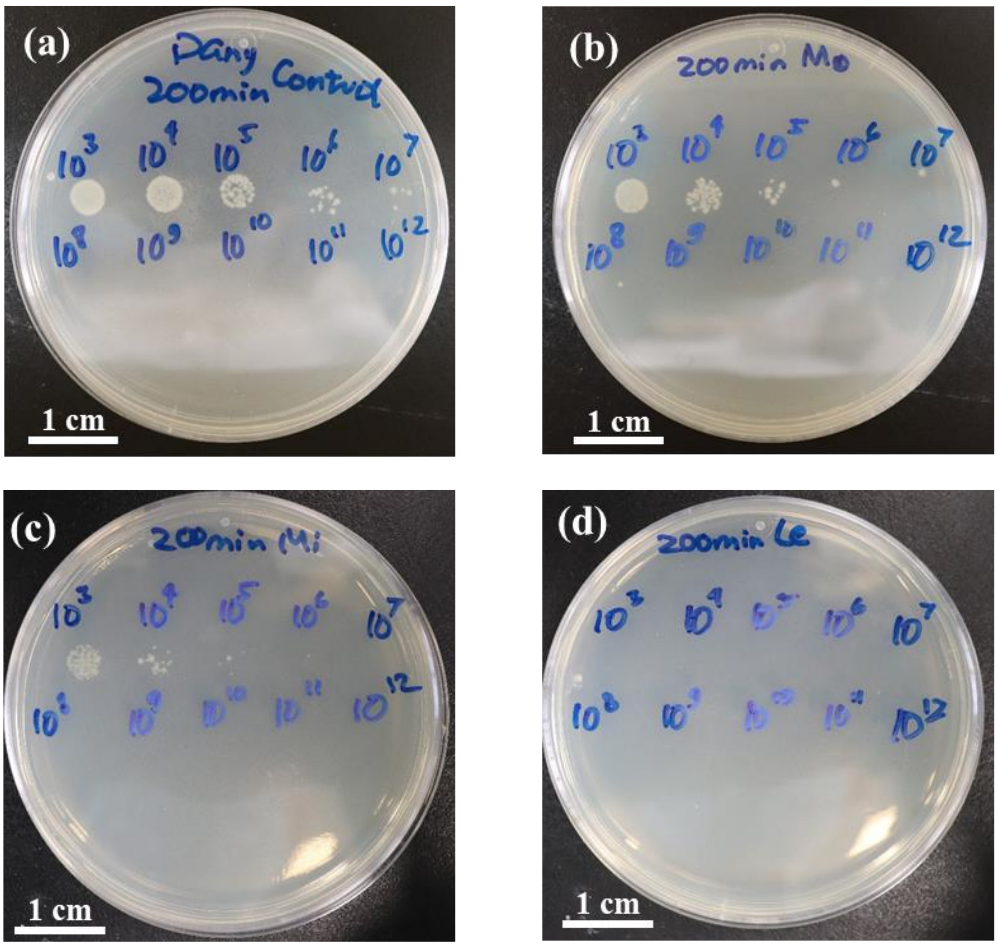

Figure 5-4: The viability of *E. coli* after 24 h incubation (a) Control, (b) TiO_2-P25, (c) TiO_2-Krono, and (d) GO-P25

5.3.3. Electronic band structure

Figure 5-5 show the optical spectra of cement-based specimens with different TiO_2, including the control specimen. The reflectance spectra (Figure 5-5(a)) were obtained using the UV-visible spectrophotometer equipped with diffuse reflectance accessory while the absorption spectra (Figure 5-5(b)) were determined from reflectance spectra using the Kubelka-Munk equation. It can be noted from Figure 5-5 that the optical spectra consist of three basic regions. First is a region with weak absorption in the wavelength range of 400 – 700 nm which is corresponding to the visible light region. Samples containing P25 and Krono indicate no response in this spectrum while sample containing GO-P25 show a better response under visible light. Second region is a strong absorption in the ultraviolet range of 250 – 370 nm, which is principally consistent with the characteristic of TiO_2 optical spectra. This ultraviolet spectrum contains sufficient energy to induce band-to-band transition of TiO_2 that are

important step to initiate the photocatalysis process. Last region is an absorption threshold in the range of 370 – 400 nm, which coincides with the threshold of pure TiO_2, and hence it might correspond to a bandgap energy of TiO_2. In contrast, the control specimen displays a relatively constant absorption spectra with a small absorption threshold at short wavelength. As this absorption threshold does not correspond to the characteristic of TiO_2 optical spectra, the absorption threshold can only be related to the colour of specimen (Jimenez-Relinque et al., 2017).

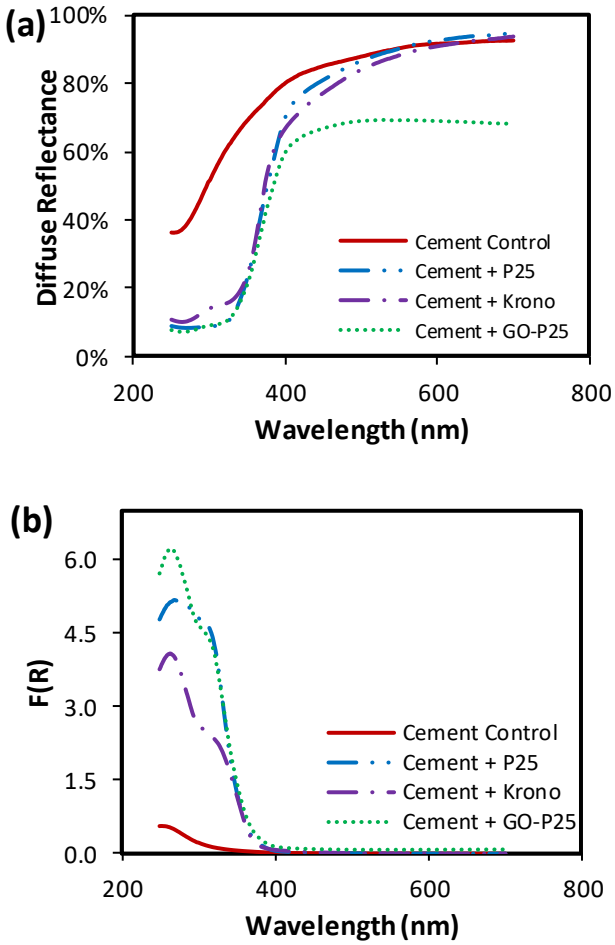

Figure 5-5: (a) Diffuse reflectance spectra and (b) Kubelka-Munk absorption curves

The bandgap energy of TiO_2-based cementititous samples can be determined by plotting the Kubelka-Munk absorption data using Tauc's relation.

$$F(R)hv = (hv - Eg)^2 \qquad (1)$$

The F(R) represent Kubelka Munk optical absorption coefficients, hv denotes the quantity of the energy of light, and Eg is the bandgap energy transition of materials.

The plot in Figure 5-6 show the relationship between the energy of light (hv) on the abscissa and the quantity of $(F(R)hv)^{1/2}$ on the ordinate. It displays a distinct linear regime in the region of band-to-band transition and the extrapolation of this line to the y = 0 yields the bandgap (Eg) value. The bandgap values of TiO_2 and TiO_2 mixed with cement are listed in Table 5-4. It was found that there is a slight reduction of optical bandgap of TiO_2 mixed with cementitious materials in comparison with TiO_2 itself. Bandgap energy of TiO_2-based cementitious samples are determined to be 3.20, 3.16, and 3.08 for cement specimen mixed with P25, Krono, and GO-P25, respectively. The lowered bandgap can be due to the presence of localised defect state near the valence and/or the conduction band of TiO_2 (Jimenez-Relinque et al., 2017, Karapati et al., 2014).

Table 5-4 Bandgap and Urbach energy

TiO_2 type	Bandgap of TiO_2 (eV)	Bandgap of TiO_2 with cement (eV)	Urbach energy (eV)
P25	3.21	3.20	0.37
Krono	3.26	3.16	0.36
GO-P25	3.11	3.08	1.61

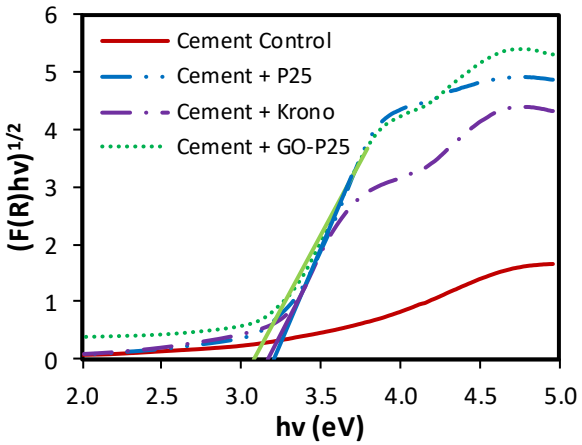

Figure 5-6: Determination of bandgap energy for cement samples with different TiO_2

Previous study suggested that TiO_2 mixed with cementitious materials to some extent was similar to surface modification of TiO_2 that could alter the electronic structure of TiO_2 by creating the surface defect state (Ti^{3+} and oxygen vacancies) (Karapati et al., 2014). The presence of the defect states causes the formation of an absorption tail

that extend the conduction band or valence band into the forbidden gap. The absorption tail is called Urbach tail and the energy associated with this tail is called Urbach energy (Boubaker, 2011, Choudhury and Choudhury, 2014). The Urbach energy can be determined using the following equation:

$$\alpha = \alpha_o exp(E/E_u) \qquad (2)$$

where α, E, and Eu represents the absorption coefficient, the photon energy, and the Urbach energy, respectively (Boubaker, 2011, Choudhury and Choudhury, 2014, Jimenez-Relinque et al., 2017). In order to estimate the Urbach energy, the relationship between ln α and photon energy (hv) should be constructed. Since the absorption coefficient (α) is proportional to the Kubelka-Munk absorption spectra (F(R)), Figure 5-7 show the plot of ln F(R) versus photon energy (hv). The curve follows a linear relationship and the positive reciprocal of the linear slope gives the Urbach energy, Eu.

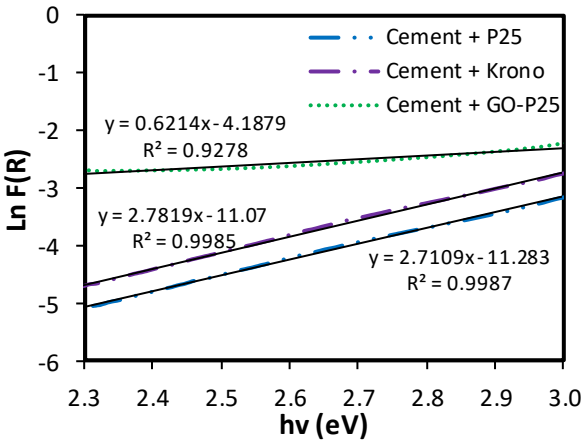

Figure 5-7: Determination of Urbach energy of TiO_2-based cement samples

Figure 5-7 presents the graph of Urbach energy for all TiO_2-based cement samples and Table 5-4 lists the corresponding Urbach energy. The highest Urbach energy for GO-P25 cement samples indicates the high density of the localized defect states. The defect is favorable to trap the electron and suppress the charge recombination process. Following excitation by photon energy, the excited electron is trapped by the surface defect states (oxygen vacancies or Ti^{3+}) which in turn improve the life-time of the charge carriers (Jimenez-Relinque et al., 2017). Moreover, the defect states allow a

higher possibility of band-to-tail transition or tail-to-tail transition (Entradas et al., 2014, Ikhmayies and Ahmad-Bitar, 2013, Rivera et al., 2016), reducing the energy needed for photoexcitation to initiate the photocatalysis process.

5.3.4. Surface hydrophobicity

Different kind of processes in microbiology depends on cell aggregation (cell-to-cell interaction), co-immobilization (cell with foreign cells interaction), or adhesion/fouling (cell to inert material interaction), all of which are surface sensitive reactions (Amory and Rouxhet, 1988, Lewin, 1984). As previously mentioned, the bactericidal effect at early stage may be affected by initial attachment of bacteria on the cement-based surface. Research study explained that the response of biological environment in contact with a given material is controlled by the physicochemical properties of its surface (Amory and Rouxhet, 1988, Ding et al., 2014a, Riveiro et al., 2018). Surface properties like surface charge, surface roughness, and wettability influence the interaction between the surface and biological environment.

As one of the important properties, the wettability shows the tendency of the surface to interact with one fluid rather than another. It can be evaluated by measuring the water contact angle, the angle between the interface of liquid-vapor and a solid surface. A water-repelling (hydrophobic) surface has high contact angle and low surface energy whereas a water-attracting (hydrophilic) surface has low contact angle and high surface energy. Figure 5-8 displays the water contact angle of cement-based surface containing different loadings of TiO_2. It can be seen that increasing TiO_2 loading result in an increase of water contact angle and improve the level of hydrophobicity. More hydrophobic surface prevents the fast contact and adhesion of cell into cement-based surface, limiting antibacterial effect at early stage. Another important finding is that the surface of cement samples with GO-P25 could switch from hydrophobic surface to super-hydrophilic surface after 2 hours of visible light exposure, as shown in Figure 5-8. After electron excitation, the generated electron-hole pairs could react with the Ti^{4+} cations and the O^{2-} anions to form the Ti^{3+} and O_2, creating the oxygen vacancies (Fujishima et al., 2008). It can be then occupied by water molecules to form chemically adsorbed OH groups and hence make the surface hydrophilic. Hydrophilic surface promotes the spreading and adhesion of cell which

is supported by work of Schakenraad et al. (1986). Higher cell adhesion after light irradiation expose the active surface with higher bacteria cell, leading to a significant improvement of the rate of antibacterial process.

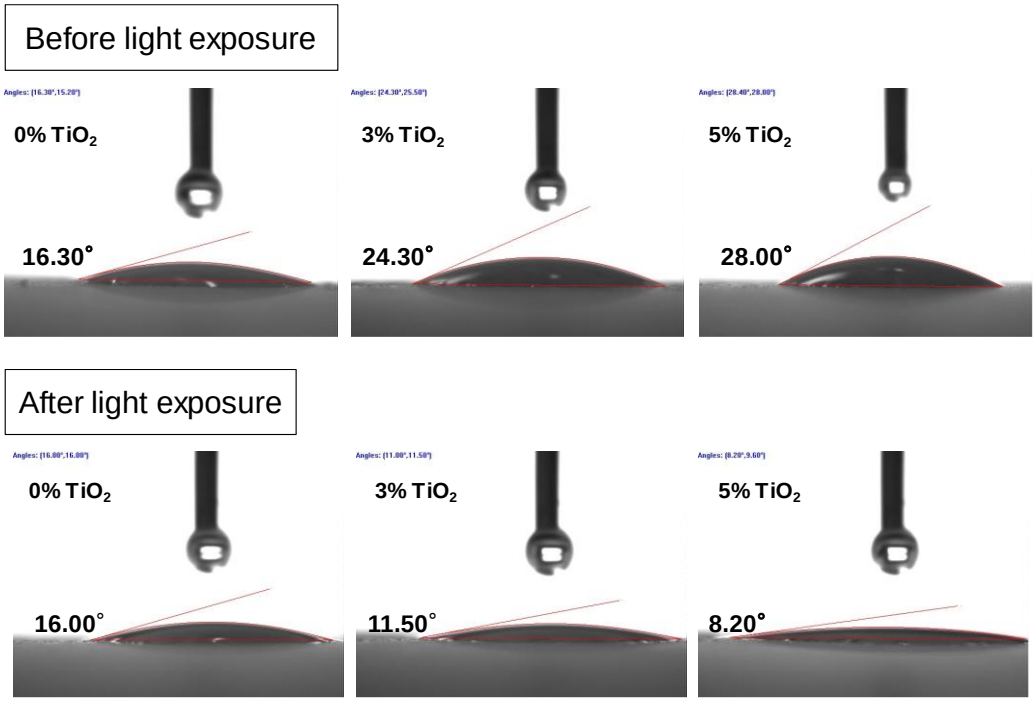

Figure 5-8: Water contact angle of cement based surface containing TiO_2 (GO-P25)

5.4. Summary

In this study, the photocatalytic efficiency of GO-TiO_2 nanocomposites intermixing with cementitious materials under visible light irradiation was investigated. Parametric study was firstly conducted to statistically determine the relationship between the governing factors and the photocatalytic activity. Three parameters including TiO_2 type, TiO_2 loading, and mixing method were evaluated on their correlation to the photocatalytic performances. It is found that the main effects of TiO_2 type and TiO_2 loading are highly significant on the photodegradation of Rhodamine B dye while the effect from mixing procedure was considered not significant. Furthermore, it was also revealed that there is a significant effect from the interaction between TiO_2 type and TiO_2 loading on photocatalytic performance.

Further, cement-based samples mixed with different TiO_2 type such as GO-P25, Krono, and P25 (one significant factor with four levels, including control specimen)

were used for antibacterial study under visible light irradiation. Specimen with GO-P25 outperformed specimens with TiO_2-Krono and TiO_2-P25 for the antibacterial of *E. coli* under visible light. It is likely that hydrophobicity plays a key role in the adhesion of cell into the surfaces, limiting the bactericidal activity at early stage. The surface of cement samples with GO-P25 could switch from hydrophobic surface to super-hydrophilic surface after visible light exposure and hence increase the cell dispersion on the surface. Higher cell adhesion exposes the active surface with higher bacteria cell, leading to a significant improvement of the rate of antibacterial process afterwards.

It was found that there is a slight reduction of optical bandgap of TiO_2 mixed with cementitious materials in comparison with pure TiO_2. The bandgap lowering can be due to the presence of localised defect state near the valence and/or the conduction band of TiO_2. The electronic structure of TiO_2-photocatalyst intermixed with cement matrix may be distorted through the formation of defect state. The highest Urbach energy for GO-P25 cement samples indicates the high density of the localized defect states. The defect states could be beneficial for initiating the photocatalysis process by reducing the energy needed for photoexcitation through a band-to-tail or tail-to-tail transition.

Chapter 6. Lightweight engineered cementitious composites (ECC) for antibacterial application

6.1. Overview

Engineered cementitious composite (ECC), a class of high-performance fiber-reinforced cementitious composites (HPFRCC), has a unique characteristic of high tensile ductility and multiple microcracks (Li, 2008). As the most important characteristic, the high tensile ductility is represented by tensile strain hardening behaviour (metal-like behaviour) with tensile strain capacity in the range of 3-5%, which is about 300-500 times that of normal concrete or FRC. Micromechanics based design tailors the interaction among fiber, matrix, and interface to attain high tensile ductility through the development of multiple microcracking while minimizing fiber volume fraction, generally 2% by volume (Li, 1998, Li, 2003, Li et al., 2001). After first cracking, the crack width increases until reaching a steady-state crack width (around 60 μm) and further loading generate multiple microcracking rather than localised crack opening. Even in the presence of large deformations, ECC materials can maintain the very small crack width, less than < 100 μm. The tight crack width property is of great importance for improving the durability of both material and structure (Lepech and Li, 2006).

Due to its unique characteristics, ECC materials nowadays have been used in a wide range of full scale applications, from sprayed ECC for Dam retrofitting to seismic resistance elements of high rise buildings (Kojima et al., 2004, Li, 2008, Maruta et al., 2005). In some ECC applications, for example precast wall panel, the use of lightweight ECC makes condition more favorable for reducing the intrinsic weight of structure as well as the seismic internal mass. There is three basic forms of lightweight concrete: no-fines concrete, aerated concrete, and lightweight aggregate concrete (Newman and Owens, 2003). Previously lightweight aggregates such as expanded perlite sand, glass micro-bubbles, polymeric micro-hollow bubble, and fly-ash cenospheres were used in attempts to achieve the lightweight property in ECC materials (Huang et al., 2013, Wang and Li, 2003). It can produce a lightweight ECC with an air-dried density range of approximately 900 to 1600 kg/m^3 while maintaining a tensile strain capacity over 3%.

Photoinduced processes governed by light activated TiO_2 have been investigated in many applications. In recent years, there has been increasing interest in using cementitious materials as catalyst supporting media (Chen and Poon, 2009b). The cementitious materials used in building facade offer enormous surface area for photocatalytic reactions (Cassar, 2004). TiO_2 semiconductors can absorb the light with energy greater than their bandgap and generate an electron-hole pair. The generated electron-hole pairs can be utilized for creating electric power (photovoltaic process), promoting chemical reaction (photocatalysis process) or altering its surface properties (super-hydrophilicity) (Carp et al., 2004). Photocatalysis technologies make the production of construction materials with advanced functions such as self-cleaning, air purifying and self-sterilizing surface feasible (Zhu et al., 2004).

Incorporating TiO_2 photocatalyst into lightweight ECC materials for example as a photocatalytic precast wall panel is attractive to control airborne pollutants. Prolonged exposure to airborne pollutants (volatile gas, liquid droplets, microbes, or particulate matters) may affect human immune systems (Albright and Goldstein, 1996). Photocatalytic lightweight ECC materials may be able to keep the surface clean, control the level of air pollutant, and maintain the surface sterile (Guo et al., 2013, Singh et al., 2018). Despite many works on photocatalytic cementitious materials, little evidence is available on the development of photocatalytic functionalities of ECC materials. This work aims to develop a Photocatalytic Lightweight Engineered Cementitious Composites (PL-ECC) for antibacterial application. The influence of TiO_2 and different lightweight ingredient materials on mechanical properties and antibacterial behaviour based on *Escherichia coli* (*E. coli*) was investigated.

6.2. Methodology

6.2.1. Material and mix design

Mix proportion of antibacterial lightweight ECC investigated in this study was summarized in Table 6-1. Three types of lightweight aggregates were evaluated such as fly-ash cenospheres (FAC), glass bubbles K-1, and air entraining agent (AEA). The characteristics of glass bubbles is listed in Table 6-2. The cement used for all mixtures was a white cement type I (Aalborg Portland Malaysia). PVA fiber REC-15

(Kuraray, Japan) with a diameter of 39 μm, a length of 12 mm, and 0.5% oil coating was used with constant proportion of fiber in the mixture at 2% by volume. AEROXIDE TiO_2 P25 (Evonik, Germany) was used as a photocatalyst material to introduce the antibacterial properties into lightweight ECC materials. Other ingredients including superplasticizer (SP) and viscosity modifying agent (VMA) were used to control the workability and achieve good fiber dispersion.

Table 6-1 Mix proportion of photocatalytic lightweight ECC

Mix No	Cement	FAC	FA	AEA	GB	Water/CM	SP	VMA	TiO_2	PVA (by vol)
Ref. (Yang et al 2014)	1	Sand (0.5)	-	-	-	0.31	0.003	-	-	0.02
1	1	-	-	-	-	0.30	0.005	-	0.05	0.02
2	1	-	-	0.1	-	0.26	0.008	-	0.05	0.02
3	1	0.1125	2.2	-	-	0.26	0.007	-	-	0.02
4	1	0.1125	2.2	-	-	0.26	0.017	-	0.05	0.02
5	1	-	-	-	0.2	0.80	0.069	0.0015	-	0.02
6	1	-	-	-	0.2	0.80	0.092	0.0015	0.05	0.02

- Lightweight material: FAC (fly ash cenospheres), AEA (air entraining agent), and GB (glass bubbles)
- CM (cementitious materials): Cement and FA (fly ash)
- Admixtures: SP (superplasticizer) and VMA (viscosity modifying admixture)

Table 6-2 Physical properties of glass bubbles

Density (kg/m^3)	125
Composition	Soda-lime-borosilicate glass
Average diameter (μm)	65
Effective maximum diameter (μm)	120
Isostatic crush strength (MPa)	1.7

6.2.2. Specimen preparation

All ECC mixture was prepared using a 20 L planetary mixer (Hobart HL200 Mixer). The mixing processes was started by stirring all the solid ingredients like white cement, lightweight aggregate, and TiO_2-P25 powder for several minutes until it was evenly distributed. Then, water and superplasticizer were added into the dry mix and the mixing was continued until the fresh mix reached a consistent state before adding

fibers. PVA fiber was slowly added into the mixture shortly afterwards. The mixing was stopped once it reached a good fiber dispersion and no clumping of fibers was observed. The fresh ECC mixtures were cast into three sets of 50 mm cube mould for compression tests, six sets of dogbone mould for tension tests, three sets of disc-shape mould for antibacterial test. The specimens were covered with plastic paper for 24 h at a room temperature (25±1 °C). Then, all specimens were demolded and cured at room conditions before testing at the age of 28 days.

6.2.3. Mechanical testing

The compression test was conducted on 50 mm cube specimen to determine the compressive strength of materials at the age 28 days. At least three specimens were tested for each mixture. Uniaxial tensile test was carried out on the dog-bone specimen to characterize the tensile stress-strain behaviour at the age of 28 days. The test was carried out under displacement control with a loading rate of 0.1 mm/min to simulate quasi-static loading condition. Two LVDTs (Linear Variable Displacement Transducers) were attached on both side of specimen to measure the extension. The testing gauge length is approximately 100 mm. Figure 6-1 display a tensile test and compression test machine used in this study.

Figure 6-1: Tensile test and compression test machine

6.2.4. Photocatalytic experiments

The photocatalytic activity was evaluated by decomposition of *Escherichia coli (E. coli)* under UV/visible light irradiation. Before each experiment, bacterial strains and growth media was prepared. Briefly, the *E. coli* K-12 was used as bacterial strain and obtained from bacterial library in the environment laboratory of Nanyang Technological University. *E. coli* was grown at 37° C in a liquid nutrient medium (Difco™ LM Broth, Miller (Luria Bertani)) for 24 h. After incubation, concentration of the culture was adjusted by dilution to reach the same initial concentration for all groups.

E. coli disinfection experiments were carried out using a PTFE beaker of 250 ml as a batch reactor. A 500 W long arc xenon lamp with an UV/visible spectrum was used as the light source to mimic the sunlight, providing a light intensity of 20k lux at the surface of the sample. Different lightweight ECC samples containing 5% of TiO_2-P25 were firstly autoclaved to sterilize it. Subsequently, the samples were exposed to *E. coli* suspension and kept in contact with bacteria environment under dark conditions for 30 min to reach adsorption equilibrium. The system was then irradiated with visible light to investigate the photocatalytic efficiency. At regular time point the viable bacteria were evaluated by growing it in Luria Bertani (LB) agar plates by a series of dilution. The colony forming units (CFUs) were examined after 24-h incubation at 37 °C. Figure 6-2 summarize the experimental procedure for antibacterial test of lightweight engineered cementitious composites (PL-ECC).

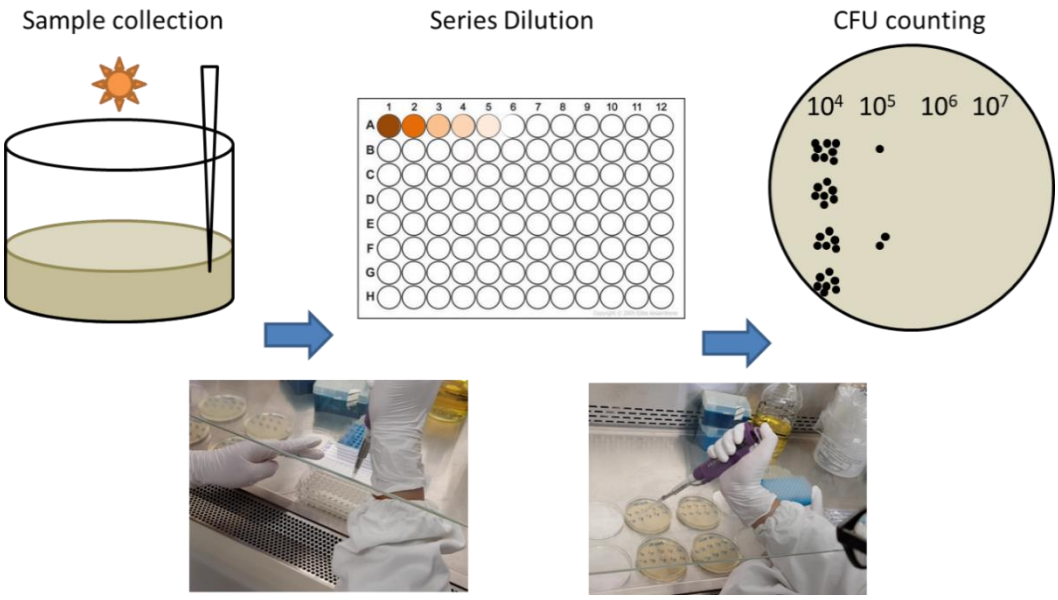

Figure 6-2 Antibacterial experiment

6.3. Result and discussion

6.3.1. Density and thermal conductivity

As one of the essential properties in the lightweight materials, the density of PL-ECC specimens was measured after 28 days curing under laboratory environment. Figure 6-3(a) show the density of PL-ECC in the range of 890 to 1547 kg/m^3 and it is approximately 30% - 60% lower than that of normal weight ECC (Mix 1) with a density of 2212 kg/m^3. In Mix 2, air entraining admixture was used to introduce air bubbles into ECC matrix. Density of PL-ECC made with AEA is 1455 kg/m^3, which is about 34% less than that of normal ECC (mix 1). The following mixes were produced using microsphere materials like fly ash cenospheres and glass bubble, with particle size smaller than 200 µm. The use of these small spherical microparticles produce stable air voids due to its hollow-spheres structure. Fly ash cenospheres is typically produced as industrial by-product from combustion of the coal, while glass bubble has been made from a soda-lime-borosilicate glass. PL-ECC produced using FAC (mix 4) has a density of 1547 kg/m^3 - around 30% lower that of normal weight ECC. Furthermore, the density of mix 6 using 20% of glass bubble to cement weight result in a very low density around 890 kg/m^3.

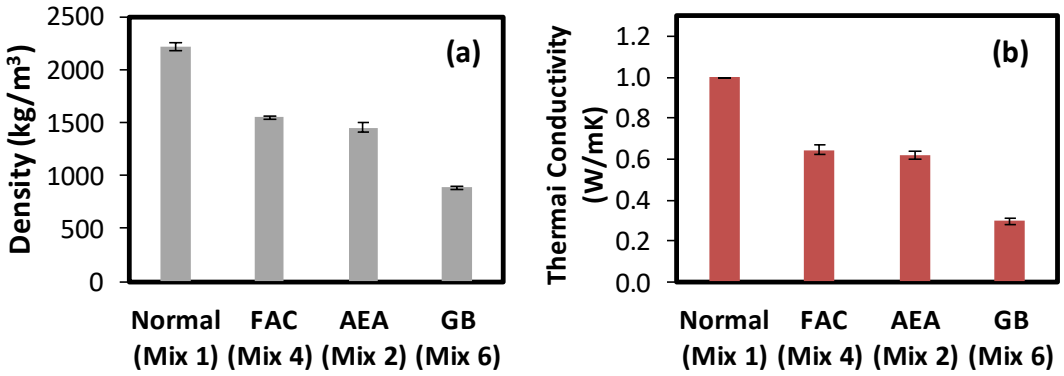

Figure 6-3 (a) Density and (b) thermal conductivity of photocatalytic lightweight ECC

In general, the reduction of the dry density is followed by the reduction of their thermal conductivity. Figure 6-3 clearly shows a positive correlation between the density and thermal conductivity of PL-ECC. Low thermal conductivity of PL-ECC is associated with the lower thermal conductivity of lightweight materials embedded in the ECC matrix, such as air bubble due to the use of AEA (k_c-$_{air}$ = 0.03 W/m. K), hollow cenospheres (k_c-$_{FAC}$ = 0.08 W/m.K), and glass bubble (k_c-$_{GB}$ = 0.04 W/m. K). This result is consistent with previous study demonstrated that thermal conductivity of concrete materials is dependent on the type of aggregate used in the concrete mixture (Rudolph, 1980). The concrete made with different aggregate could have different thermal conductivity values even for the concrete with same density. It might be due to the differences between the thermal properties of typical mineral in the aggregate.

6.3.2. Microscopic observation

As mentioned in previous section, air entraining admixture was used in mix 2 to introduce air bubbles into ECC matrix as a lightweight filler. Figure 6-4(a) presents the fracture surface of PL-ECC mix 2 showing the air bubble induced by AEA in ECC matrix. It can be seen that the air bubbles were formed in different size, ranging from tens of micron to hundreds of microns. The size distribution of air bubble could not be controlled during mixing process. Mechanical force of mixing and period of handling process significantly influence the formation and distribution of air bubble in ECC matrix (Wang and Li, 2003).

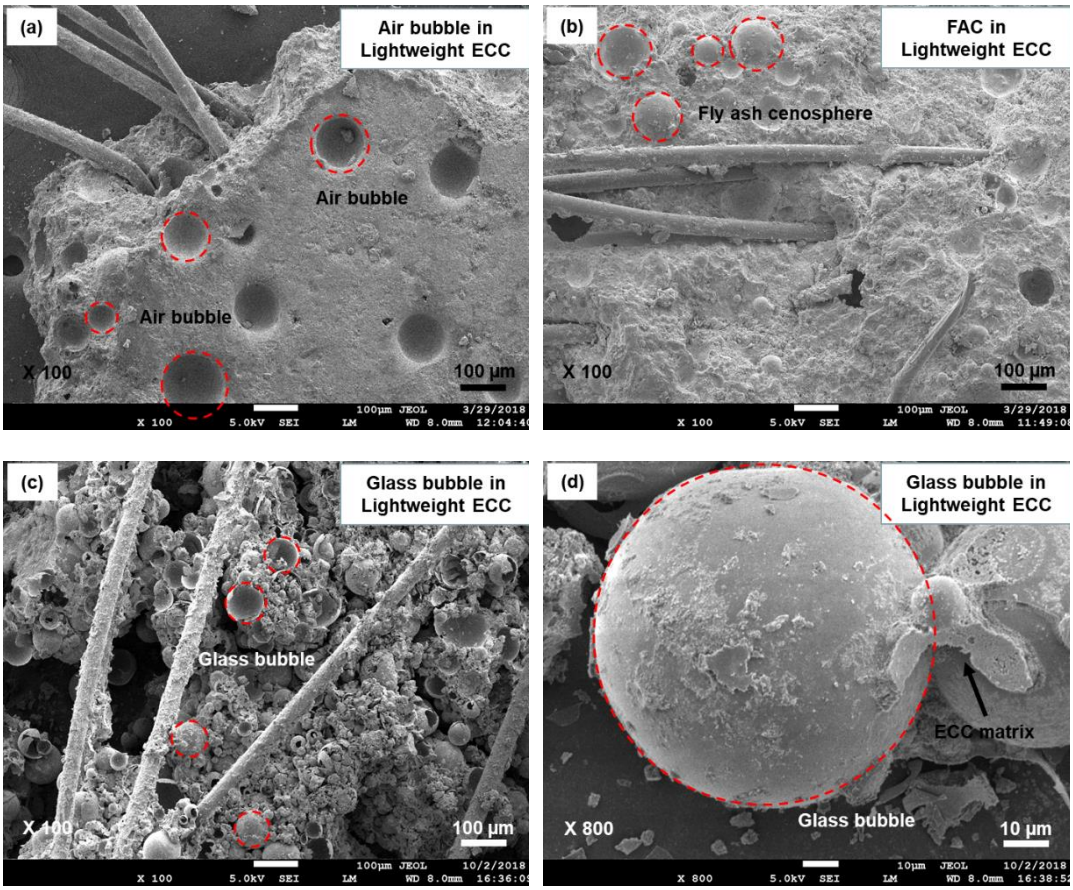

Figure 6-4 Fracture surface of photocatalytic lightweight ECC (PL-ECC) : (a) air bubbles induced by AEA in ECC matrix, (b) FAC detection in ECC matrix, (c) glass bubbles in ECC matrix and (d) enlarged section of glass bubbles

The remaining mixtures was prepared using microsphere materials, for example fly ash cenospheres and glass bubble. Previous study (Wang et al., 2012, Wang et al., 2011) found that these microsphere materials showed a stability against alkali-silica environment and can be considered as inert filler in the lightweight ECC evaluated in this study. It can be seen from Figure 6-4(b) and Figure 6-4(c), cenospheres and glass bubble were uniformly dispersed in ECC matrix and can be easily observed in the sample. Some of them are intact while the others were broken. Enlarged section of glass bubble (Figure 6-4(d)) show the microstructure of the transition zone between ECC matrix and glass bubble, which is similar to interfacial part between cement paste and aggregate.

6.3.3. Mechanical test

The compressive strength of PL-ECC mixtures at 28 curing days are presented as bar graph in Figure 6-5. In general, it could be seen that the use of lightweight aggregates (AEA, FAC, and Glass bubbles) exhibited a decrease in compressive strength. It can be attributed to the reduction of hydration product as the amount of cement used is reduced. On the other hand, the lightweight ECC mixtures with TiO_2 also shows a lower compressive strength than the mixtures without TiO_2. This might be ascribed to the agglomeration of nanoparticles which introduces weak zone in the ECC matrix, leading to reduction of compressive strength (Zhao et al., 2015).

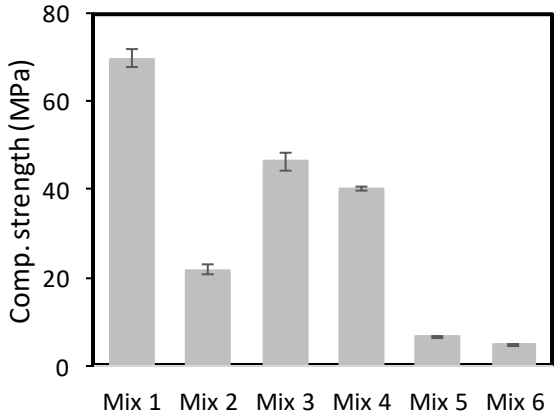

Figure 6-5 Compressive strength of PL-ECC at 28 days

It was noticed that PL-ECC with glass bubble (mix 5 and mix 6) display a unique foam-structure behaviour under compression, which is totally distinct behaviour from those commonly brittle failure observed in cementitious materials. During the test, the testing specimen was fully deformed from cube specimen into a disk shape specimen, as shown in Figure 6-6(a). Previous study explained that the mechanism of stress-strain curve of foam structure are related to the properties of cell wall material and geometry (Ashby and Medalist, 1983). Under compression, at first, the foam deform in a linear-elastic way; then its cell buckle or even fracture to give nonlinear elasticity; at the end the complete failure is achieved and it forces a full contact of cell wall; as a result, there is rapid increase in the compressive strength. The influence of porosity on fracture mode of materials is depicted in Figure 6-6(b) (Meille et al., 2012). if material porosity increases, it lessened the mean size of solid wall. Then, the crack can directly link two neighbour pores and it can break another

solid wall, leading a cellular like fracture. Hence, high porosity and smaller pore size are favourable for achieving the ductile cellular-like behaviour.

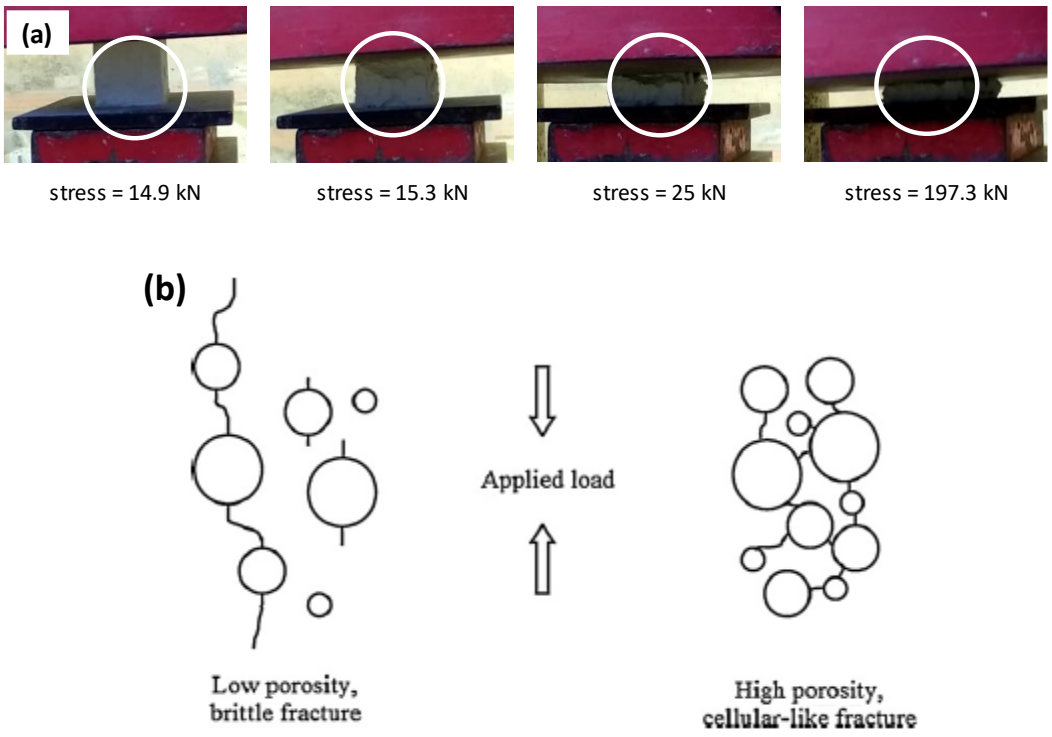

Figure 6-6 (a) Ductile compressive behavior of PL-ECC with glass bubble (mix 5) and (b) brittle and ductile fracture mode of matrix foam materials (Meille et al., 2012)

The tensile stress-strain curves of PL-ECC mixtures are shown in Figure 6-7. The first cracking strength, ultimate tensile strength, and tensile strain capacity of PL-ECC mixtures are derived from these curves. The first cracking strength is defined as the tensile stress at the end of initial elastic stage, which associated with matrix properties. All these properties are summarized in

Table 6-3. Under uniaxial tensile loading, all mixtures exhibit strain hardening behaviour through multiple cracking process. As can be seen, the introduction of TiO_2-P25 nanoparticle in general reduce the first cracking strength of PL-ECC mixtures.

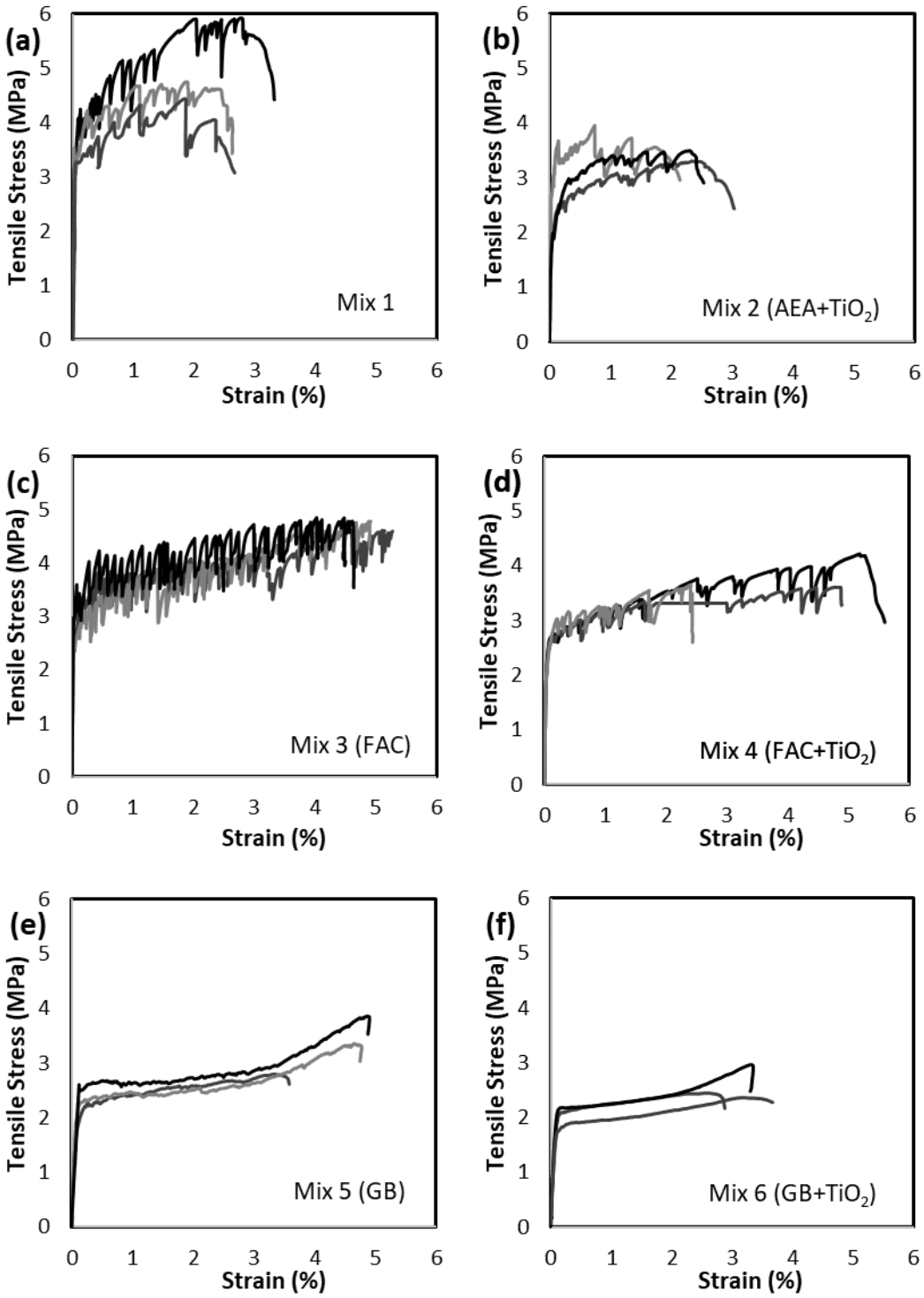

Figure 6-7 PL-ECC mixes exhibit ductile tensile behavior with high tensile strength

Table 6-3 Summary of tensile properties of ECC mixtures

	Mix 1	Mix 2	Mix 3	Mix 4	Mix 5	Mix 6
First cracking strength (MPa)	3.41±0.07	2.08±0.32	2.68±0.15	2.22±0.39	2.36±0.12	2.01±0.13
Tensile strength (MPa)	5.03±0.45	3.59±0.19	4.82±0.02	3.83±0.20	3.33±0.31	2.59±0.19
Strain capacity (%)	2.88±0.22	2.57±0.26	5.05±0.25	4.33±0.97	4.42±0.42	3.30±0.23

Figure 6-8 shows the comparison of tensile behaviour between mix 1 and 2, along with the result from Yang et al. (2014) as mixing reference. As can be seen, a strain-hardening behaviour with an average tensile strain capacity over 2.5% was observed for three of them. However, compared to their result, the first cracking strength decreased from 4.6 MPa to 3.41 MPa and 2.08 MPa from reference mix to mix 1 and 2. This finding is consistent with earlier findings suggesting that the introduction of TiO_2 lower matrix fracture toughness as well as first cracking strength, as evidenced by the reduction of compressive strength (Zhao et al., 2015). These conditions are favourable for achieving multiple fine cracking and improving tensile strain capacity.

The use of air entraining agent generates air bubbles in the ECC matrix and however the size distribution of the air bubble could not be controlled. Previous study found that the higher water content cause even more large bubbles, leading to a loss of bond strength when the fiber is in contact with air bubbles (Wang and Li, 2003). Hence, the formation of large air bubble can diminish the strain hardening potential and as consequence limit the strain capacity. Less water cement ratio was adopted for mix 2 to suppress the formation of large bubbles and maintain strain capacity to be comparable with the reference mix.

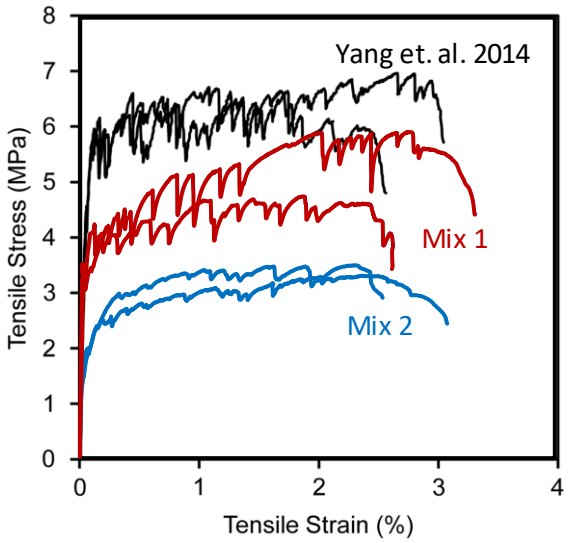

Figure 6-8: Uniaxial tensile stress-strain curves of lightweight ECC with AEA

Mix 3 and 4 adopted the strategy of using fly ash cenospheres (FAC) as lightweight ingredients. Figure 6-9 illustrates the uniaxial tensile stress-strain curves of lightweight ECC contains FAC. One of the Green Lightweight ECC (GL-ECC) studied by Huang et al. (2013) was adopted as reference for mix 3 with slight modification on the type of cement and fiber oil coating. Mix 3 exhibited a slightly higher tensile strain capacity compared to the result of Huang et al. (2013). Previous study suggested that lowering the oil coating of fiber surface could increase the interface frictional bond strength, leading to an increase of tensile strain capacity (Yang et al., 2014). As can be seen, compared to mix 3, the addition of TiO_2 in mix 4 lowered first cracking strength and ultimate tensile strength with small increase of strain capacity.

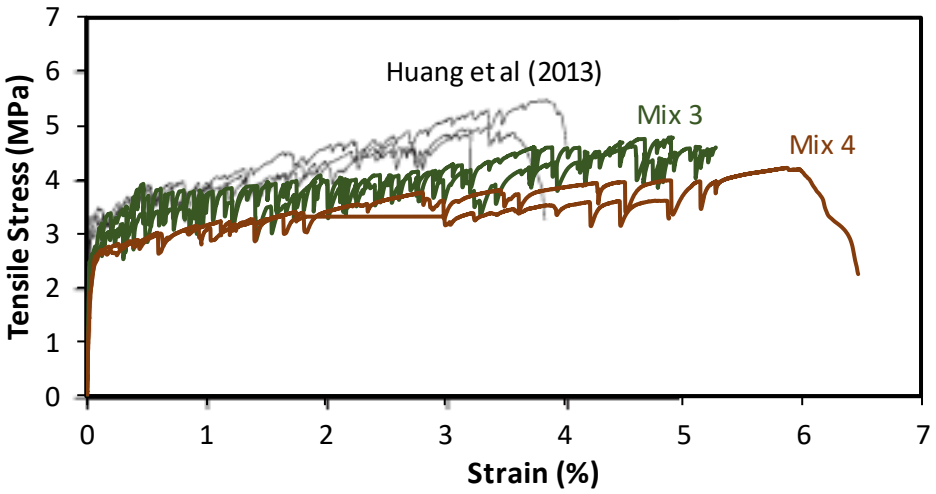

Figure 6-9: Uniaxial tensile stress-strain curves of lightweight ECC with FAC

Mix 5 and 6 incorporated the strategy of using glass bubbles as lightweight aggregates. Uniaxial tensile-strain curve of both mixes is plotted in Figure 6-10. A reference result was also plotted from the work of Zhang and Li (2015). Lightweight ECC made with glass bubble still exhibited a robust tensile-strain hardening behaviour with a tensile strain above 3 %. PL-ECC with glass bubble still show moderate first cracking strength compared to reference mix. Compared to mix 2, glass bubbles, the microspheres material, have less resistance to crack propagation which are favourable for achieving multiple cracking and strain hardening behaviour.

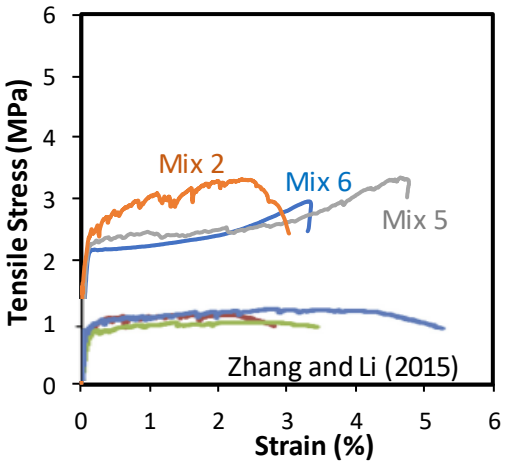

Figure 6-10: Uniaxial tensile stress-strain curves of lightweight ECC with Glass bubbles

6.3.4. Antibacterial activity of photocatalytic lightweight ECC

Due to the presence of transition metal in ordinary Portland cement (OPC) that have a potency to decrease the photocatalytic activity by blocking the incident photon or increasing electron-hole recombination, the use of white cement in developing photocatalytic cementitious material was preferred instead of using OPC (Chen and Poon, 2009a, Guo and Poon, 2013). For that reason, white cement was used for all the mixtures in this study. In order to introduce a photocatalytic functionality into lightweight ECC material, 5% of TiO_2-P25 was added into the mix.

TiO_2-P25 has been widely used as a standard material in the field of photocatalysis because it exhibit high activity in various applications (Ohno et al., 2001). It consists of anatase and rutile phases with the ratio of 80% to 20%. TiO_2-P25 has a relatively high specific surface area, approximately 46.9 m^2/g with an average primary particle size around 20-40 nm. However, the particle has a strong tendency to agglomerate into larger particle, as shown in Figure 6-11(a). This might be due to a weak Van der Waals bond between primary particles (Jiang et al., 2009). Further, the hydrodynamic size of TiO_2 nanoparticle dispersion during mixing process can have an effect on its interaction with ECC matrix. In high pH environment during mixing process, the agglomeration can be suppressed as the repulsive force in TiO_2 become more dominant than the van der Waals force under strong alkaline condition (Jiang et al., 2009). Smaller TiO_2 cluster (Figure 6-11(b)) was observed on the fiber-matrix interface of PL-ECC compared to TiO_2-cluster in the dry state (Figure 6-11(a)).

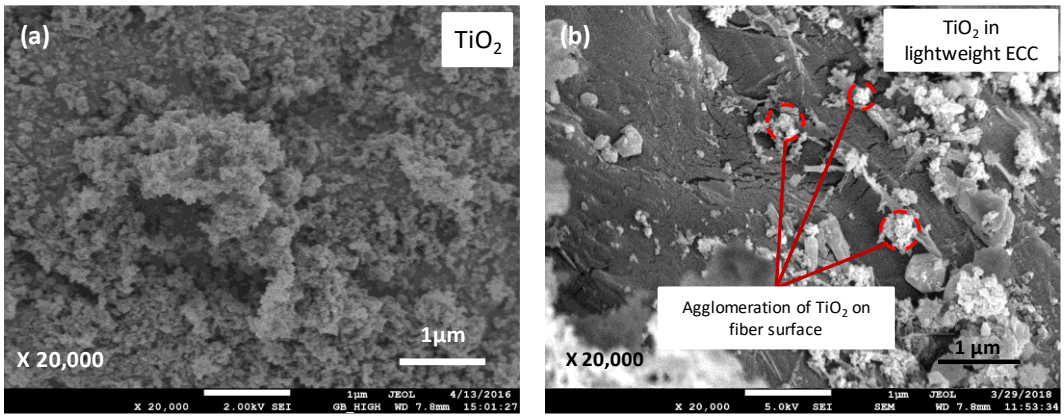

Figure 6-11 (a) Morphology of TiO_2 particle in and (b) agglomeration of TiO_2 on fiber interface

The antibacterial activities of PL-ECC are evaluated for E. coli inactivation. Three different type of lightweight materials are used including air entraining agents (AEA), fly ash cenospheres (FAC), and glass bubbles (GB). The effect of using different type lightweight materials on antibacterial activity is presented in Figure 6-12. The viability of E. coli is estimated by bacterial counting method on agar plates and expressed in logarithmic scale. The application of UV/visible light on E. coli strain did not affect the viability of living cell in the absence of TiO_2 (sample C) while strong antibacterial effect was observed for E. coli strain in contact directly with TiO_2 powder under UV/visible light exposure (sample C2).

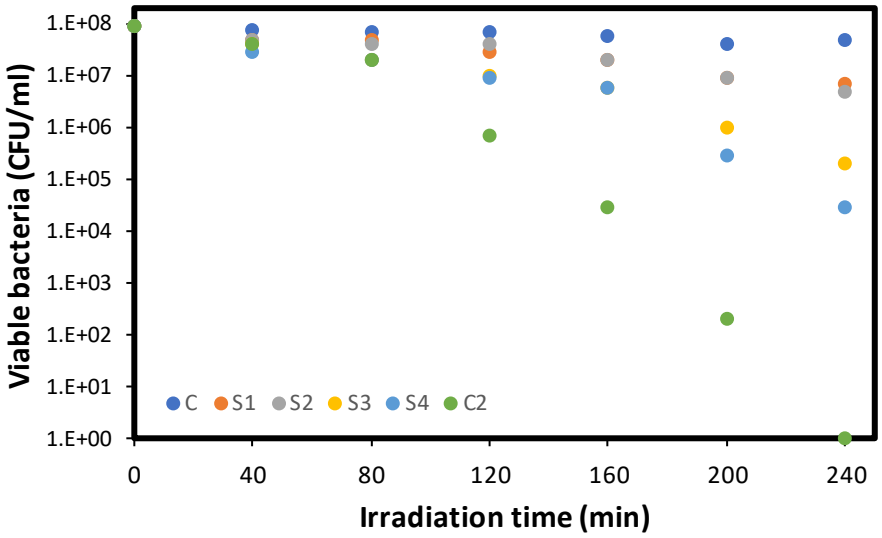

Figure 6-12 Antibacterial activity of photocatalytic lightweight ECC

As mentioned before, the loss of cell viability has a direct relationship with the duration of light exposure, longer exposure time result in a significant decrease of survival ratio. Lightweight ECC using glass bubbles (mix 6 was coded as S4 in this test) show the smallest number of viable bacteria after 240 min of UV/visible light exposure. Smallest number of viable bacteria indicates it has highest antibacterial activity among all four photocatalytic lightweight ECC materials. It is followed by antibacterial ECC with AEA (mix 2 was coded as S3). The lowest antibacterial activity was observed for the lightweight ECC with FAC as lightweight filler (mix 4 was coded as S2).

The principle techniques of producing lightweight concrete is by utilizing materials to create a large proportion of void/pore into the cement matrix (Newman and Owens, 2003). The pore structure of cementitious material is one of the important factors to determine the surface area accessible for photocatalytic process. Generally, increasing total porosity could enhance the photocatalytic performance due to the increase of accessible active-surface-area (Lucas et al., 2013, Sugrañez et al., 2013). TiO_2 surface can have a better access to the light irradiation, as the light photon could pass along the pore to activate more TiO_2 particles. The connectivity of pores also determines the rates of intrusion, the rate of bacteria accessing the mass of ECC matrix. Insufficient porosity for adsorption of contaminant may lead to negligible effect of photocatalytic activity (Rachel et al., 2002). Hence, high porosity is favourable for bacteria accessing the internal structure of cement matrix (Poon and Cheung, 2007).

Furthermore, previous study demonstrate that the use of transparent glass cullet show higher photocatalytic NOx degradation than coloured glass cullet due to higher light transmittance for the transparent one (Guo and Poon, 2013). Due to a better light transmittance property, the incident photon penetrates through the matrix of lightweight ECC with glass bubbles can illuminate higher TiO_2 surface area, resulting in higher photocatalytic activity. However, in the case of photocatalytic lightweight ECC with fly ash cenospheres, the gray pigment of FAC may absorb the incident light/photon energy and hence blocking it to be absorbed by TiO_2 nanoparticles.

6.4. Summary

In this study, the photocatalytic lightweight engineered cementitious composites (PL-ECC) for antibacterial application was investigated. Three types of lightweight aggregates were evaluated such as fly ash cenospheres (FAC), glass bubbles K-1, and air entraining agent (AEA). TiO_2 nanomaterials (Aeroxide P25) was incorporated into lightweight ECC materials to introduce photocatalytic function for antibacterial application. In term of balanced strength and strain capacity, the use of FAC in producing lightweight ECC is preferred. However, use of FAC was hindered by a significant reduction of antibacterial activity. For antibacterial purpose, light-coloured lightweight materials with white cement and glass bubbles are preferable to

maintain the photocatalytic activity. The use of glass bubble is also preferable to prepare lightweight ECC with density lower than 1000 kg/m^3 while maintaining the tensile strain capacity more than 3%. It should be noted that the antibacterial experiment in this study has been primarily concerned with E. coli strain only. Further study could be done to investigate the efficiency of TiO_2 based cementitious material for another pathogenic bacteria or microorganism.

Chapter 7. Conclusion and future work

7.1. Conclusion

The main objective of this research program is to develop multifunctional photocatalytic cementitious materials for self-cleaning and anti-microbial application. To achieve these goals, it is imperative to start the research program by synthesizing visible light activated photocatalyst. Following chemical synthesis, a good dispersion in cementitious materials should be achieved to formulate functional cementitious coating. Finally, their photocatalytic performance in self-cleaning and anti-microbial will be evaluated; further, the influence of some parameters like loading content, TiO_2 type, and mixing procedure will be assessed.

In chapter 3, the research program establishes a clear link between the nanostructure of TiO_2 and its photocatalytic performance in cementitious material for self-cleaning and anti-bacterial application. The first part deals with the nanoscale analysis of different TiO_2 materials. In particular, the hydroxyl radical production by various TiO_2 with respect to the TiO_2 surface area, morphology, and optical properties is investigated. Further, the effect of incorporating TiO_2 into cement-based composite on its microstructure is evaluated. In the last part, photocatalytic performance for self-cleaning and anti-bacterial application is assessed. Nanoscale analysis demonstrated that Aeroxide P25 showed the highest rate of hydroxyl radical production (by means of p-nitrosodimethylaniline/RNO bleaching) owing to its high specific surface area. Considering the band-energy level of P25 and RNO, oxidation of RNO by trapped holes or hydroxyl radicals is thermodynamically favorable. As a result, cement sample containing Aeroxide P25 achieved much higher Rhodamine B (RhB) degradation compared to TiO_2-anatase and TiO_2-rutile with the same loading. The addition of TiO_2 also improves photoinduced hydrophilicity effect which is favorable to enhance self-cleaning activity. Lastly, the strategy to use TiO_2-based cementitious materials for the exterior building is promising to prevent biofilm formation on the surface. Cement surface containing Aeroxide P25 generally displays much less infected area / lower bacteria survival compared to control specimen.

In chapter 4, graphene oxide–TiO_2 (GO–TiO_2) composites prepared by a simple solution mixing method are evaluated for methylene blue (MB) degradation and *Escherichia coli* (*E. coli*) decomposition under visible-light irradiation. It is shown that particle size, pore structure, and surface charge of TiO_2 material plays an important role in the photocatalytic performance. The performance improvement can be explained by two aspects. Firstly, in addition to strong absorption in the visible light range, GO can serve as photosensitizer through which strong Ti-O-C bonds formed between TiO_2 and GO as confirmed from the redshift of the absorption edge to higher wavelength region. Secondly, GO addition can significantly increase the dye adsorption capability which can not only be attributed to the increased specific surface area of the composites but also the non-covalent interactions between graphene layer and MB. The synergy between improved photodegradation activity and enhanced dye adsorption capability leads to the excellent photocatalytic performance for GO-TiO_2 nanocomposite materials. The preliminary study on application of GO-TiO_2 into cement-based construction materials confirms the effectiveness of the composites for disinfection of *E. coli*. This finding is of considerable importance since it suggests that the simple synthesis process still provides remarkable improvement in the photocatalytic activity. This simple chemical process can be easily scaled up and hence promotes potential wider practical applications of GO-TiO_2 composites.

In chapter 5, the work focuses on a study of antibacterial effect of cement-based surface mixed with TiO_2-based composite. Cement-based samples mixed with different TiO_2 type such as GO-P25, Krono, and P25 were used for *Escherichia coli* inactivation under visible light irradiation. Specimen with GO-P25 outperformed specimens with TiO_2-Krono and TiO_2-P25 for the antibacterial of *E. coli* under visible light. It is likely that hydrophobicity significantly influences the adhesion of cell onto the surfaces. Increasing TiO_2 loading results in the increase of water contact angle and improve the level of hydrophobicity. More hydrophobic surface prevents the fast contact and adhesion of cell onto cement-based surface, limiting antibacterial effect at early stage. It was found that there is a slight reduction of optical bandgap of TiO_2 mixed with cementitious materials in comparison with pure TiO_2. The bandgap lowering can be due to the presence of localised defect state near the valence and/or

the conduction band of TiO_2. The presence of the defect states causes the formation of an absorption tail that extend the conduction band or valence band into the forbidden gap. The defect states could be beneficial for initiating the photocatalysis process by reducing the energy needed for photoexcitation through a band-to-tail or tail-to-tail transition.

In chapter 6, TiO_2 photocatalyst was incorporated into lightweight ECC materials for antibacterial application. In term of, strength performance and strain capacity, the use of FAC in producing lightweight ECC is preferred. However, the use of FAC was followed by a significant reduction of antibacterial activity. For photocatalytic purpose, lighter lightweight materials are preferable to maintain the photocatalytic activity.

7.2. Future Work

To further promote the potential practical applications of TiO_2-based cementitious materials for more wide range of applications, several recommendations for the future study have been proposed.

- It should be noted that the antibacterial experiment in this study has been primarily concerned with *E. coli* strain only. Further study could be done to investigate the efficiency of TiO_2 based cementitious material for another pathogenic bacteria or microorganism.
- The influence factors such as temperature, humidity and UV radiation affecting the test results under extreme interaction need to be investigated in the future study as this is crucial for the practical application of materials
- The findings of this study are restricted to the application of TiO_2 based cementitious materials in laboratories scale, pilot study in a real environmental condition should be conducted to analyse a significant environmental factor governing the photocatalytic performance.
- It is recommended that further study could be done to study the effect of weathering process on photocatalytic removal of the dye under visible light irradiation for maintaining the long-term performance. The photocatalyst lifespan

is obviously important point for economic reason, as it sets optimum run times between catalyst regeneration and replacement.

- Life cycle analysis (LCA) and life cycle cost analysis (LCCA) should be considered in the future study to quantify holistically the environmental impact and cost effectiveness of the application of photocatalytic-based cementitious materials for building construction.
- The physic-mechanical properties (bondability, wettability, and paintability) of the cementitious paints should be optimized by tuning mixing conditions and composition.

APPENDIX A

Supporting Information

for

TiO_2-based cementitious materials for self-cleaning and anti-bacterial application: Effect of TiO_2 nanostructures on photocatalytic performances

Figure S 1: Light source with UV/vis light spectrum for photocatalytic experiment

Figure S 2: Portable spectrophotometer (Miniscan EZ 4000S, Hunterlab, USA) to measure dye intensity

Figure S 3: Light meter (Lutron Digital Instruments) to measure light intensity

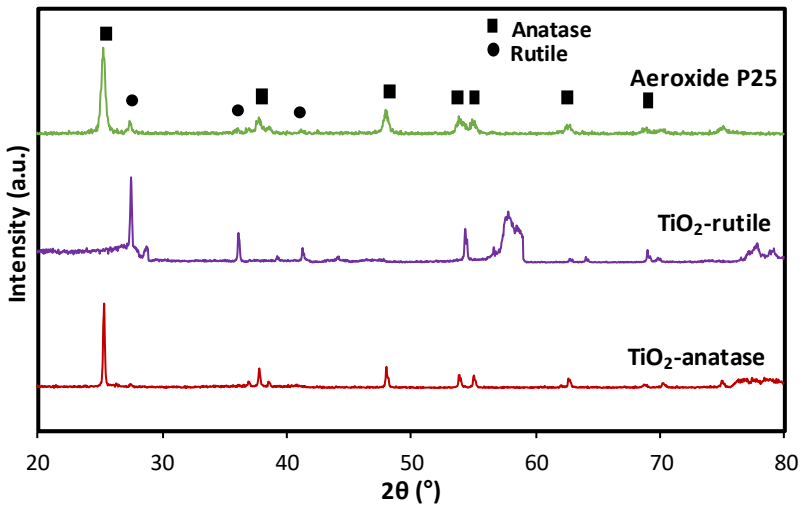

Figure S 4: XRD analysis of different TiO_2 materials showing the crystallinity of various commercial TiO_2 materials

Quantachrome QuadraWin - Data Acquisition and Reduction
for QuadraSorb SI
©2000-13, Quantachrome Instruments. All rights reserved.
version 6.0

Analysis			Report		
Operator:	Chew Wang	Date:3/29/2016	Operator: Dany	Date:2016/04/05	
Sample ID:	Dany_TiO2 P25	Filename:	Dany_TiO2 P25.QPS		
Sample Desc:		Comment:			
Sample weight:	0.0326 g				
Analysis Time:	315.4 min	End of run:	3/29/2016 7:44:46	Instrument:	QuadraSorb Station 1
Void Vol.:	He Mode.Cell: 6mm small bulbRun mode:Standard			Instrument version:6.00	
Cold Zone Vol.:	4.6785	Warm Zone Vol.:	5.8136		
Thermal delay:	30 sec	He evac time:	3 min		
Outgas Time:	18.0 hrs	OutgasTemp:	150.0 C		
Analysis gas:	Nitrogen	Bath Temp:	77.3 K		

Press. Tolerance:0.050/0.050 (ads/des)Equil time: 200/200 sec (ads/des)Equil timeout:400/400 sec (ads/des)

Data Reduction Parameters

Adsorbate	Nitrogen	Temperature	77.350K		
	Molec. Wt.: 28.013	Cross Section: 16.200 Å²		Liquid Density: 0.806 g/cc	

Relative Pressure P/Po	Volume @ STP cc/g	1 / [W((Po/P) - 1)]
5.02636e-02	8.5210	4.9695e+00
9.69551e-02	9.7945	8.7706e+00
1.44100e-01	10.9772	1.2272e+01
1.91290e-01	12.0650	1.5686e+01
2.39415e-01	13.1966	1.9085e+01
2.90010e-01	14.5757	2.2422e+01

BET summary

Slope =	72.653
Intercept =	1.613e+00
Correlation coefficient, r =	0.999430
C constant=	46.043
Surface Area =	46.892 m²/g

Figure S 5: Surface area calculation for Aeroxide P25 using BET Method

Quantachrome QuadraWin - Data Acquisition and Reduction
for QuadraSorb SI
©2000-13, Quantachrome Instruments. All rights reserved.
version 6.0

Analysis Report
Operator: Chew Wang Date:3/29/2016 Operator: Dany Date:2016/04/05
Sample ID: TiO2 Anatase Filename: Dany_TiO2 Anatase.QPS
Sample Desc: Comment:
Sample weight: 0.1440 g
Analysis Time: 275.4 min End of run: 3/29/2016 7:04:49 Instrument: QuadraSorb Station 3
Void Vol.: He Mode.Cell: 6mm small bulbRun mode:Standard Instrument version:6.00
Cold Zone Vol.:5.8295 Warm Zone Vol.:6.0989
Thermal delay: 30 sec He evac time: 3 min
Outgas Time: 18.0 hrs OutgasTemp: 150.0 C
Analysis gas: Nitrogen Bath Temp: 77.3 K
Press. Tolerance:0.050/0.050 (ads/des)Equil time: 200/200 sec (ads/des)Equil timeout:400/400 sec (ads/des)

Data Reduction Parameters

Adsorbate Nitrogen Temperature 77.350K

Molec. Wt.: 28.013 Cross Section: 16.200 Å² Liquid Density: 0.806 g/cc

Relative Pressure P/Po	Volume @ STP cc/g	1 / [W((Po/P) - 1)]
5.04184e-02	1.4428	2.9444e+01
9.69422e-02	1.6988	5.0559e+01
1.45135e-01	1.9114	7.1069e+01
1.92305e-01	2.0954	9.0913e+01
2.39804e-01	2.2636	1.1150e+02
2.86245e-01	2.4679	1.3002e+02

BET summary
Slope = 426.351
Intercept = 8.755e+00
Correlation coefficient, r = 0.999863
C constant= 49.700

Surface Area = 8.004 m²/g

Figure S 6: Surface area calculation for TiO2-anatase using BET Method

Quantachrome QuadraWin - Data Acquisition and Reduction
for QuadraSorb SI
©2000-13, Quantachrome Instruments. All rights reserved.
version 6.0

Analysis Report
Operator: Dany Date:3/30/2016 Operator: Dany Date:2016/04/05
Sample ID: TiO2 Rutile Filename: 20160330 Dany_TiO2 Rutile .QPS
Sample Desc: Comment:
Sample weight: 0.3497 g
Analysis Time: 297.8 min End of run: 3/30/2016 5:44:35 Instrument: QuadraSorb Station 3
Void Vol.: He Mode.Cell: 6mm small bulbRun mode:Standard Instrument version:6.00
Cold Zone Vol.:5.3283 Warm Zone Vol.:6.1081
Thermal delay: 30 sec He evac time: 3 min
Outgas Time: 18.0 hrs OutgasTemp: 150.0 C
Analysis gas: Nitrogen Bath Temp: 77.3 K
Press. Tolerance:0.050/0.050 (ads/des)Equil time: 200/200 sec (ads/des)Equil timeout:400/400 sec (ads/des)

Data Reduction Parameters

Adsorbate Nitrogen Temperature 77.350K

Molec. Wt.: 28.013 Cross Section: 16.200 Å² Liquid Density: 0.806 g/cc

Relative Pressure P/Po	Volume @ STP cc/g	1 / [W((Po/P) - 1)]
4.95970e-02	1.9410	2.1511e+01
9.86055e-02	2.2787	3.8410e+01
1.46653e-01	2.5332	5.4281e+01
1.91138e-01	2.7335	6.9168e+01
2.41562e-01	2.9704	8.5792e+01
2.87486e-01	3.1625	1.0208e+02

BET summary

Slope = 336.700
Intercept = 4.913e+00
Correlation coefficient, r = 0.999950
C constant= 69.535

Surface Area = 10.194 m²/g

Figure S 7: Surface area calculation for TiO_2-rutile using BET Method

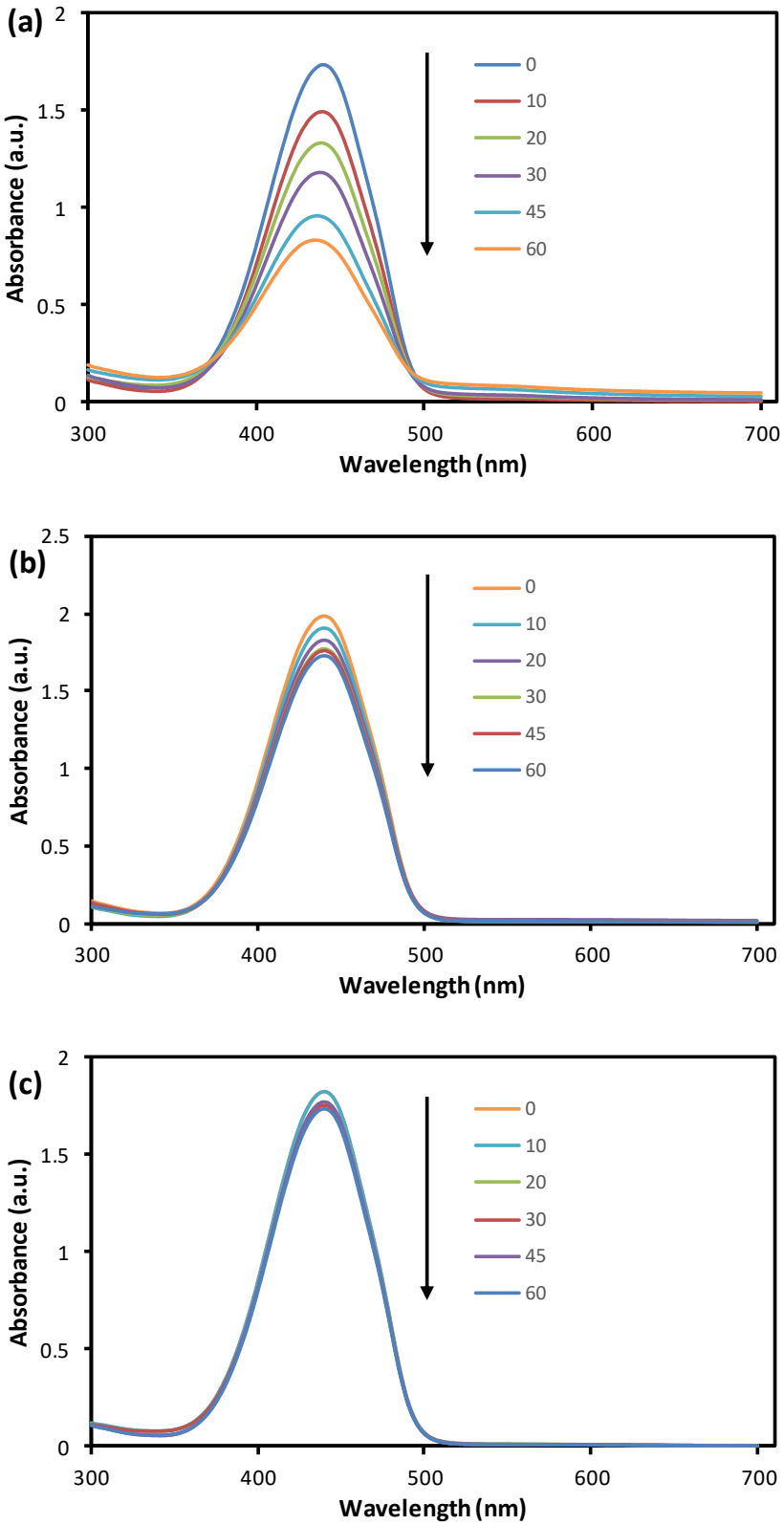

Figure S 8: Absorption spectra of RNO bleaching in aqueous TiO_2 suspension (a) TiO_2-anatase, (b) TiO_2-rutile, (c) control – A decrease of peak intensity at 440nm indicates the formation of OH radicals

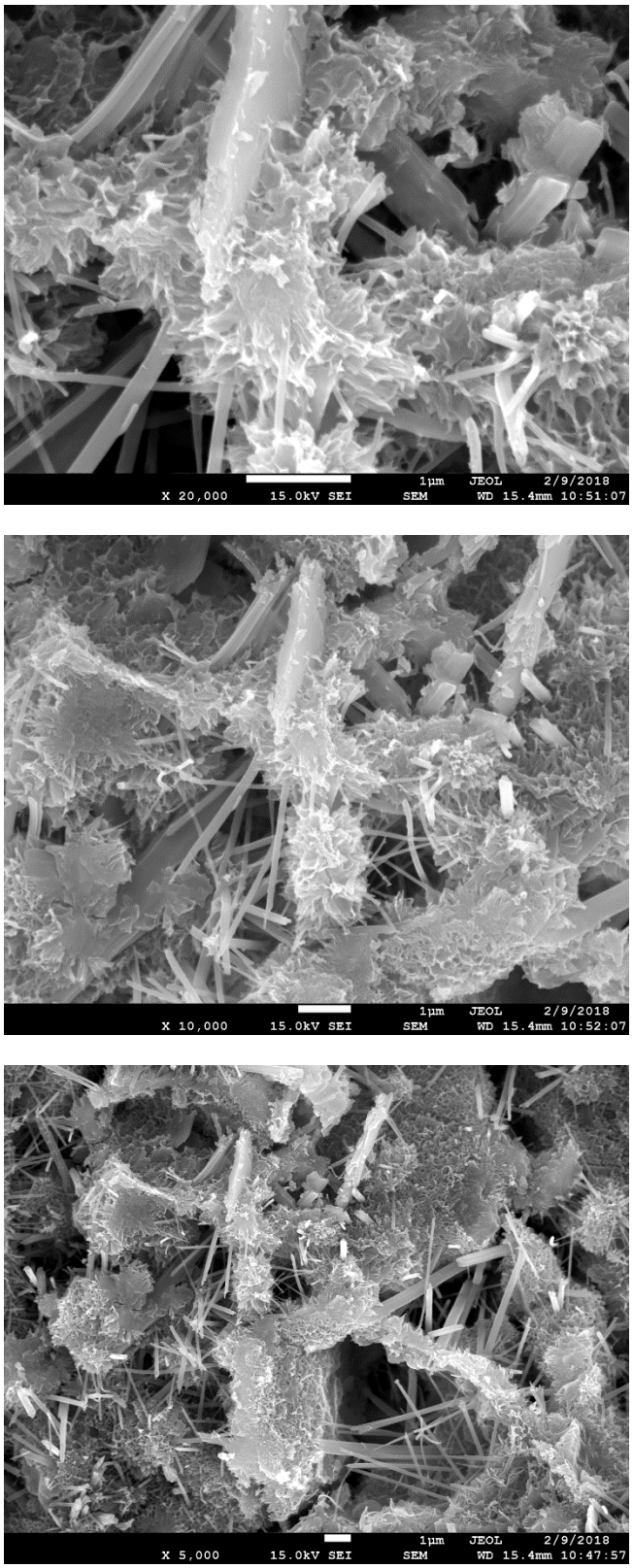

Figure S 9: SEM images of control specimen (cement paste without TiO_2) with 20k, 10k, and 5k magnification

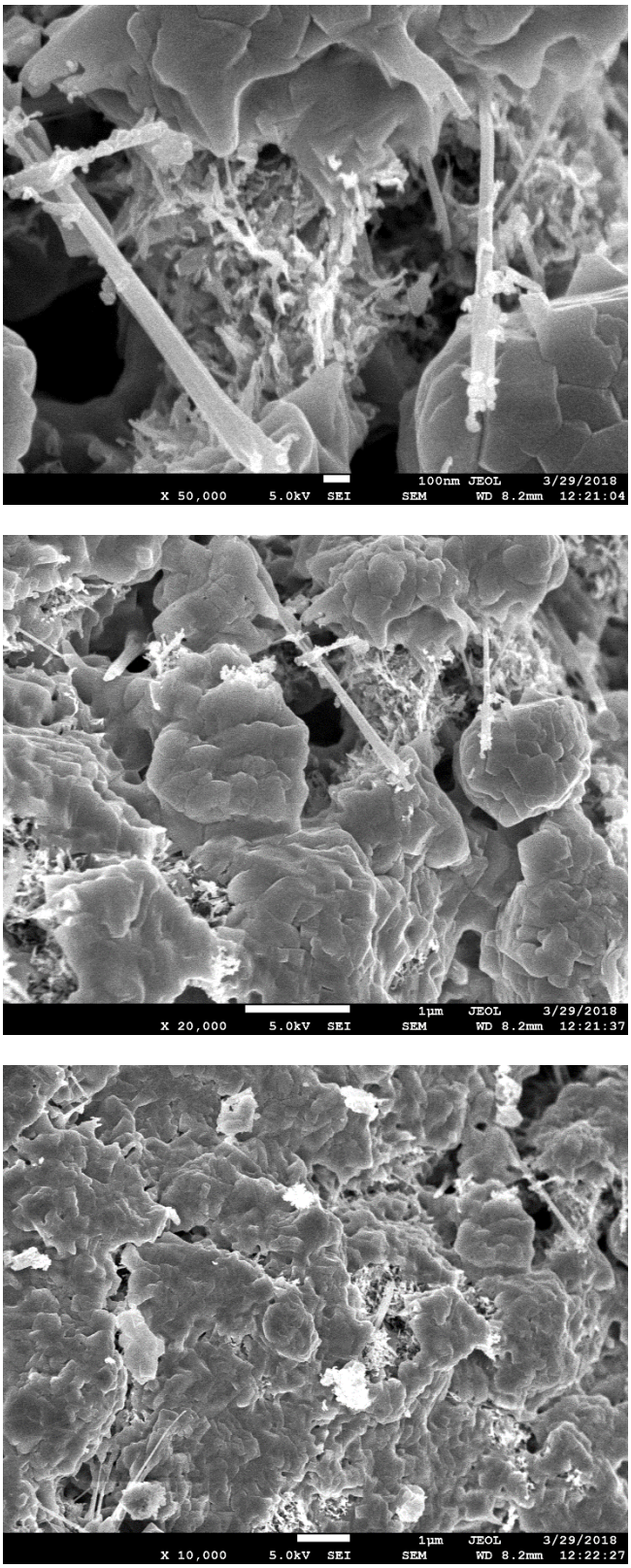

Figure S 10: SEM images of cement paste specimen with 5% Aeroxide P25 showing the agglomeration of nanoparticles and densify cement matrix (50k, 20k, and 10k magnification)

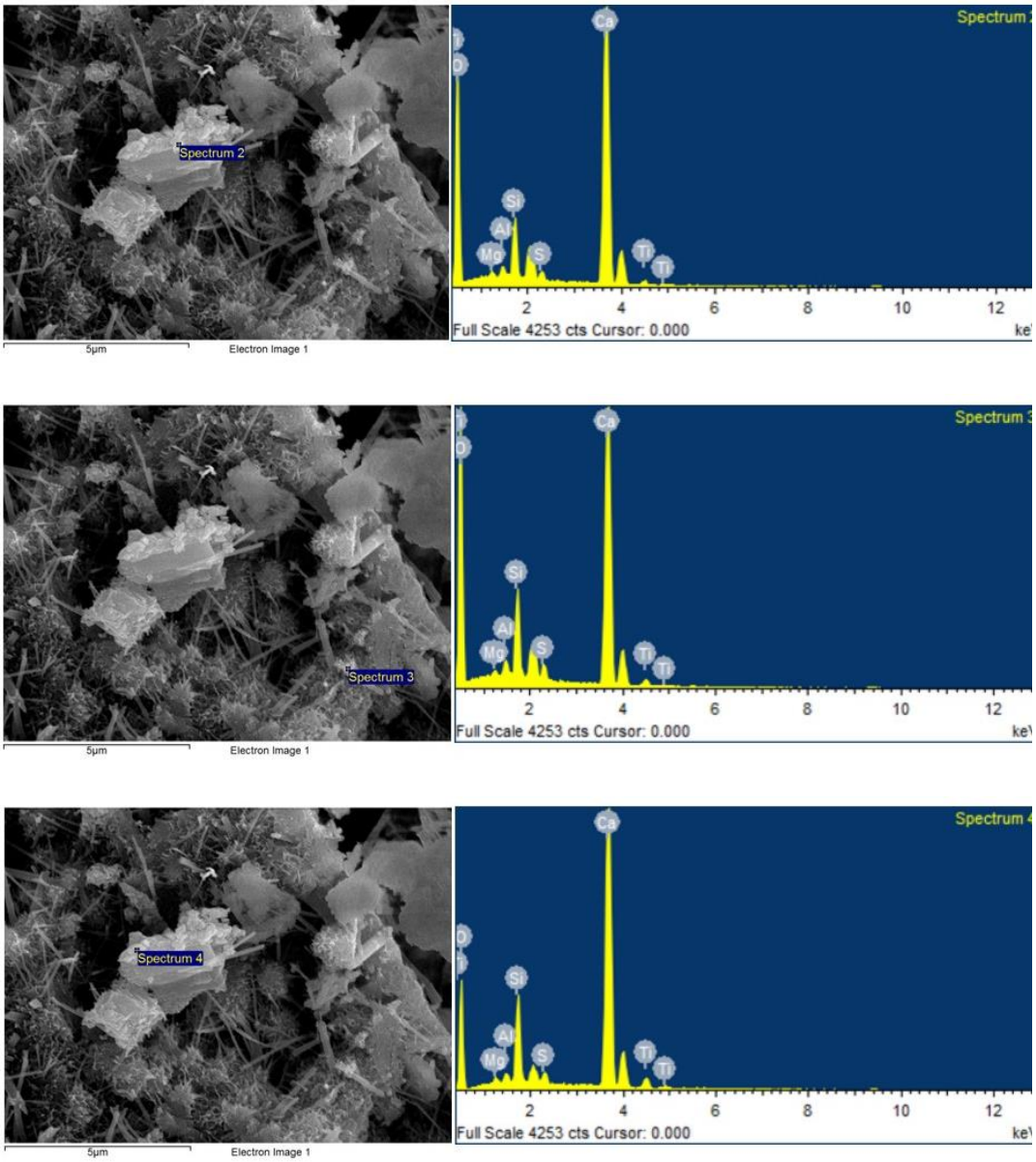

Figure S 11: EDX spectrum analysis for cement paste containing 5% Aeroxide P25 showing a presence of Ca, O, Si, and low level of Ti element

Bacterial Growth Experiments

Outdoor	Laboratory	Classroom	Bio-safety hood (Negative control)

Exposing the medium to the air for 5 mins

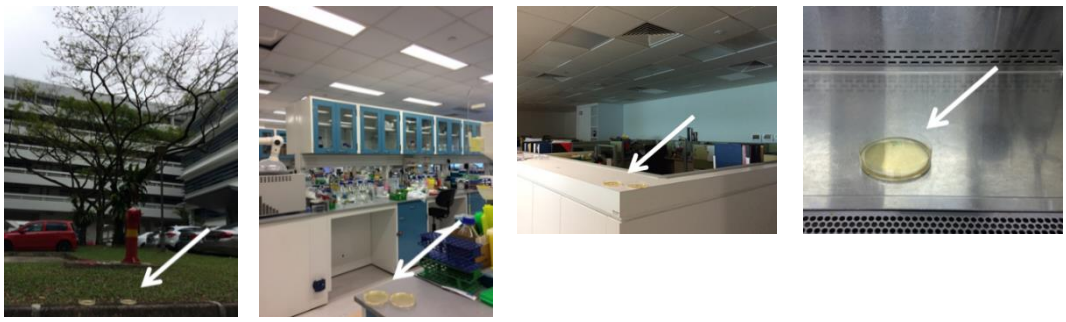

Bacterial growth after 1-day incubation

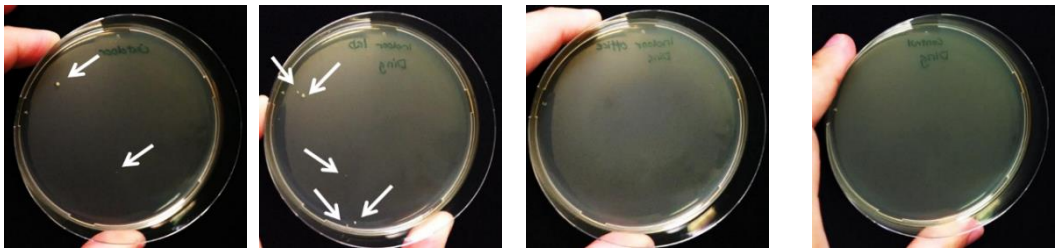

Bacterial growth after 5-day incubation

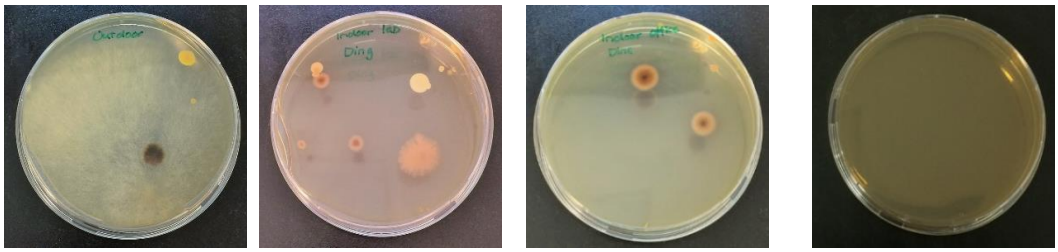

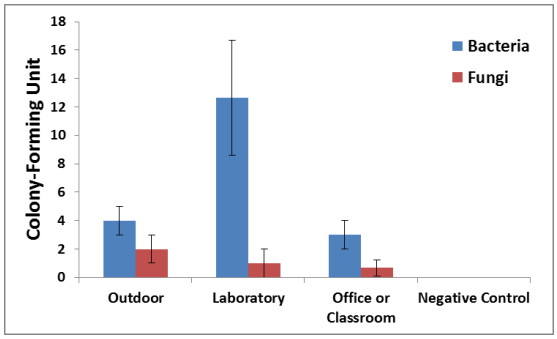

Figure S 12: Preliminary study on bacterial growth experiment to evaluate the airborne bacteria in several locations (indoor and outdoor)

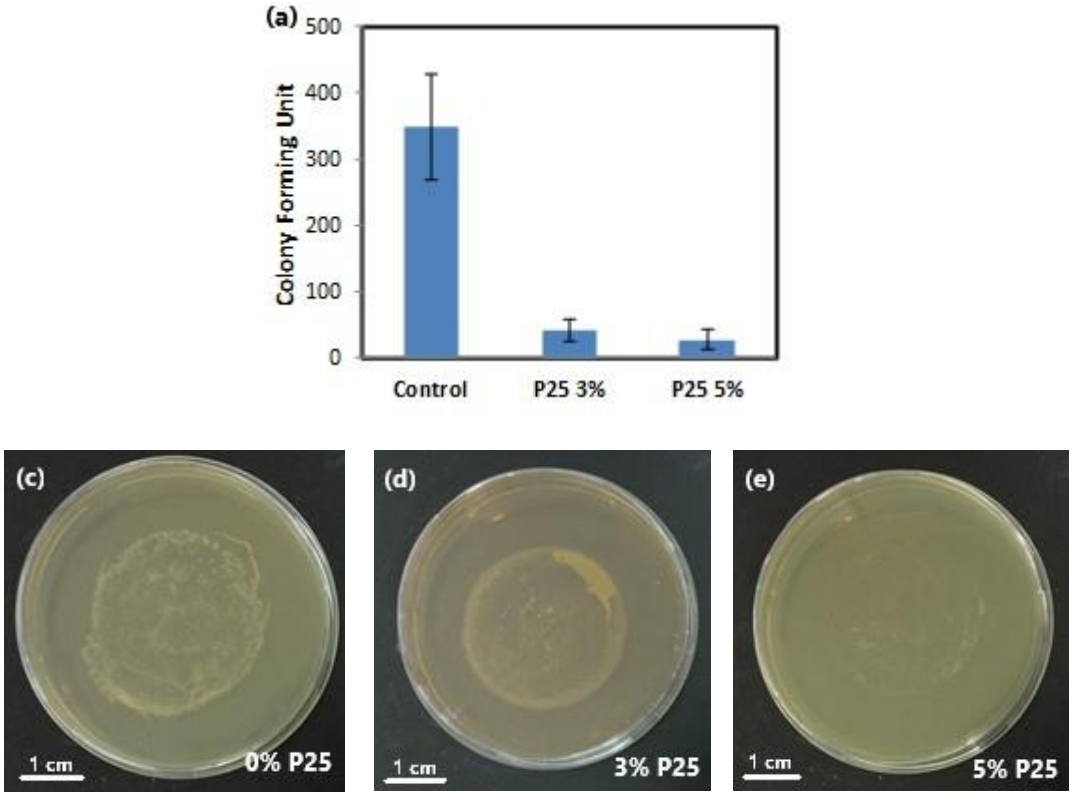

Figure S 13: The viability of *E. coli* after 24-h incubation

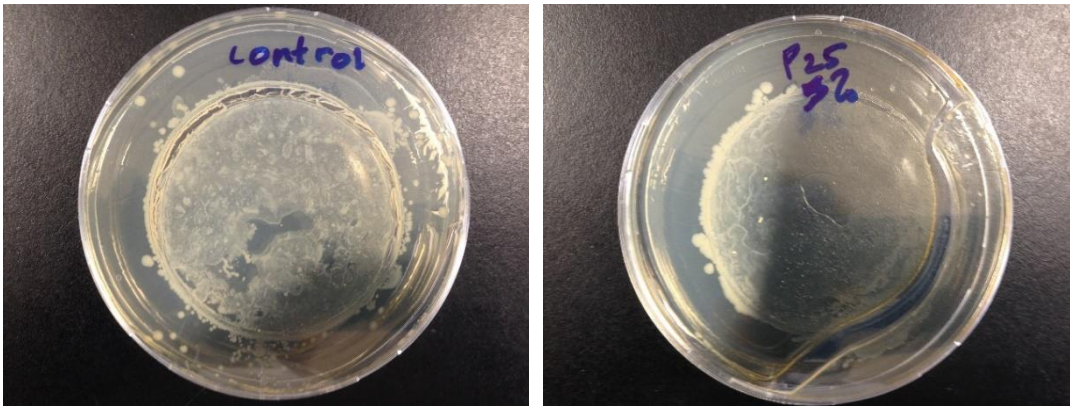

Figure S 14: The viability of *E. coli* after 24-h incubation without UV/vis irradiation for control specimen and cement sample with 5% Aeroxide P25

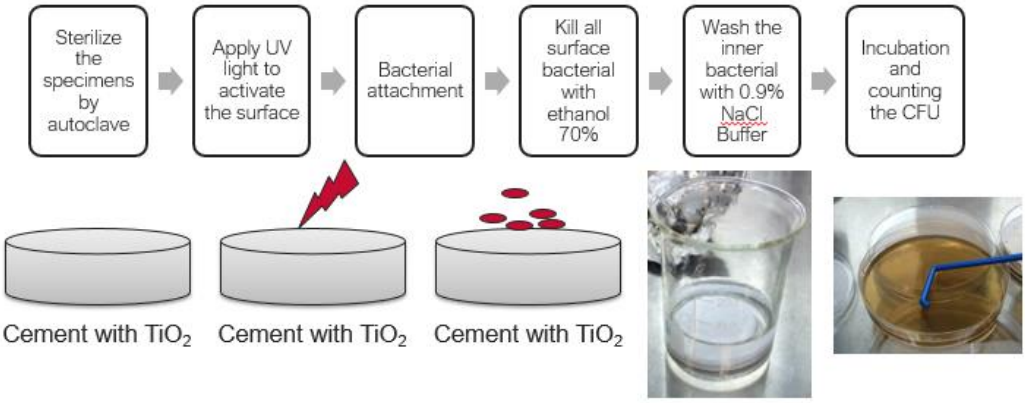

Figure S 15: Experimental procedure to study the effect of cement pores on antibacterial activity

APPENDIX B

Supporting Information

for

Graphene-based TiO_2 nanocomposites for enhanced visible light degradation of organic dye and antibacterial effect of *Escherichia coli*

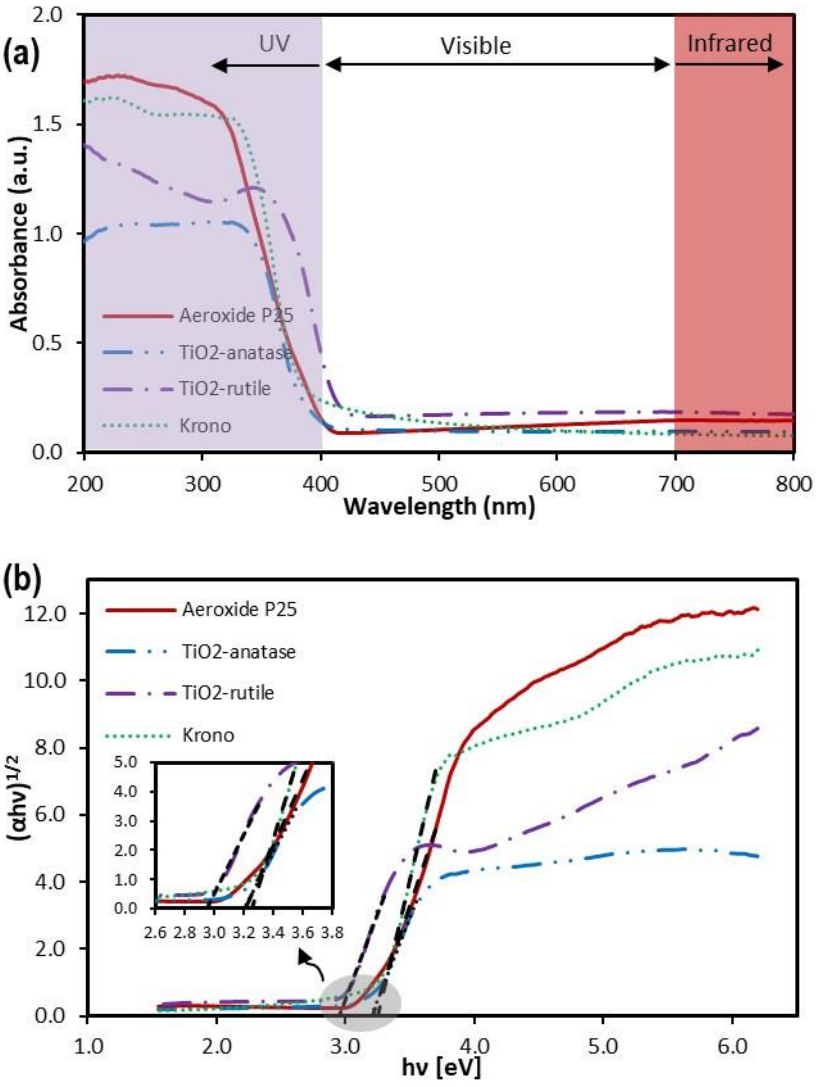

Figure S 16: (a) UV/visible absorption spectra and (b) Bandgap determination of various TiO_2

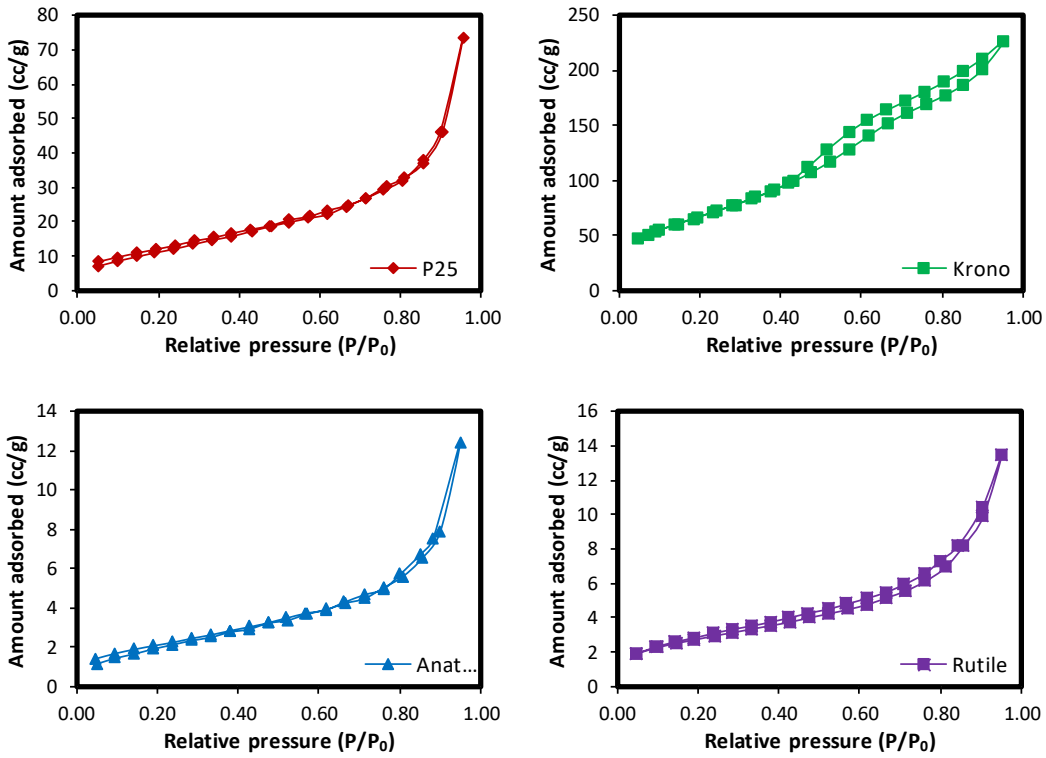

Figure S 17: N2 adsorption isotherms of TiO2-P25, TiO2-Krono, TiO2-anatase, and TiO2-rutile

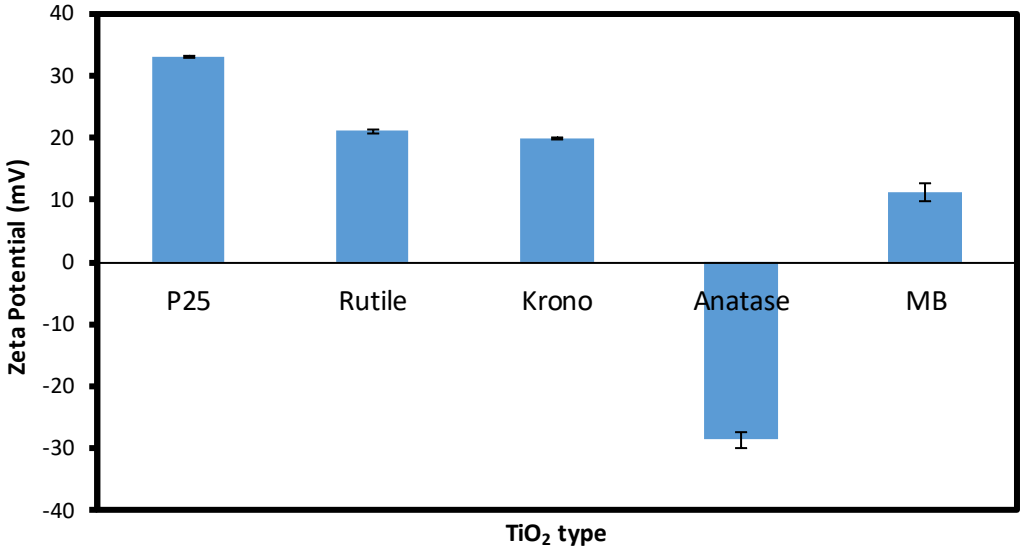

Figure S 18: Surface charge of various commercial TiO_2

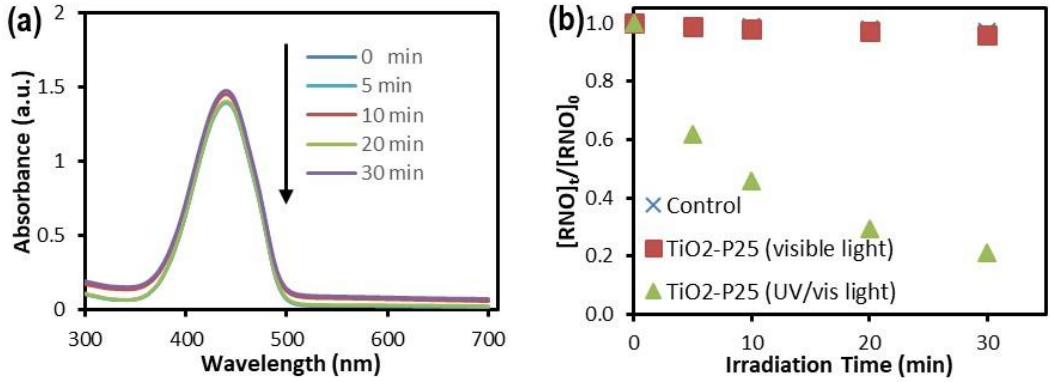

Figure S 19: (a) Absorption spectra of RNO bleaching in aqueous TiO_2 suspension under visible light irradiation and (b) Hydroxyl radical detection by means of RNO bleaching

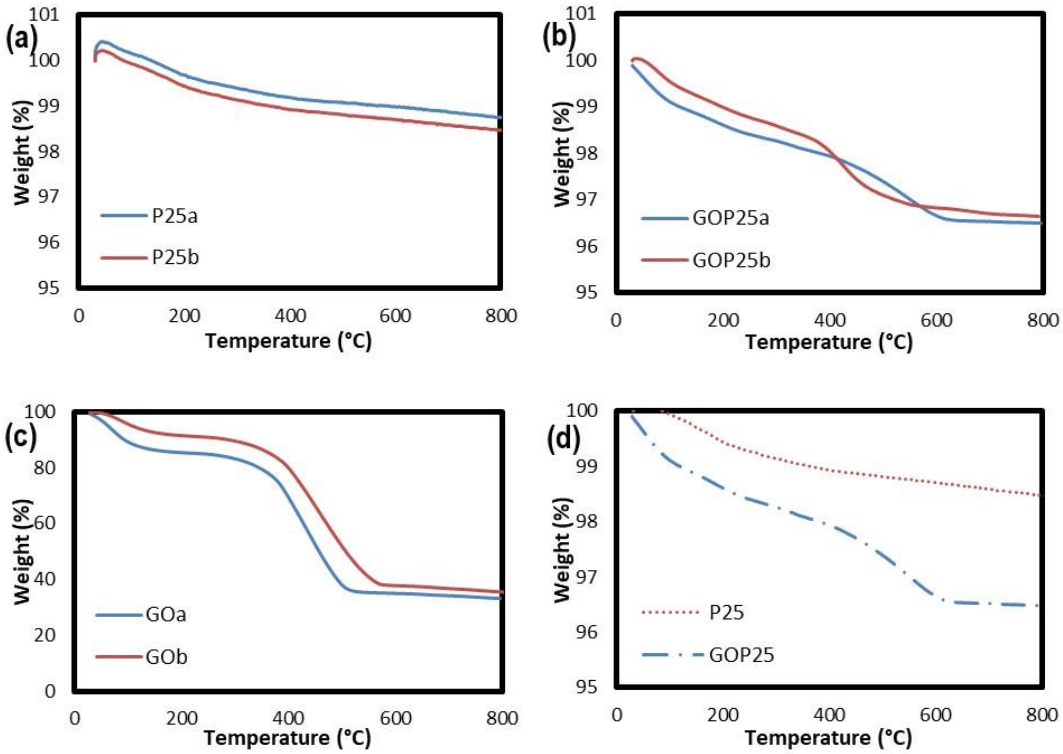

Figure S 20: TGA curves of (a) TiO_2-P25, (b) GO-P25, (c) GO and (d) TiO_2-P25 and GO-P25

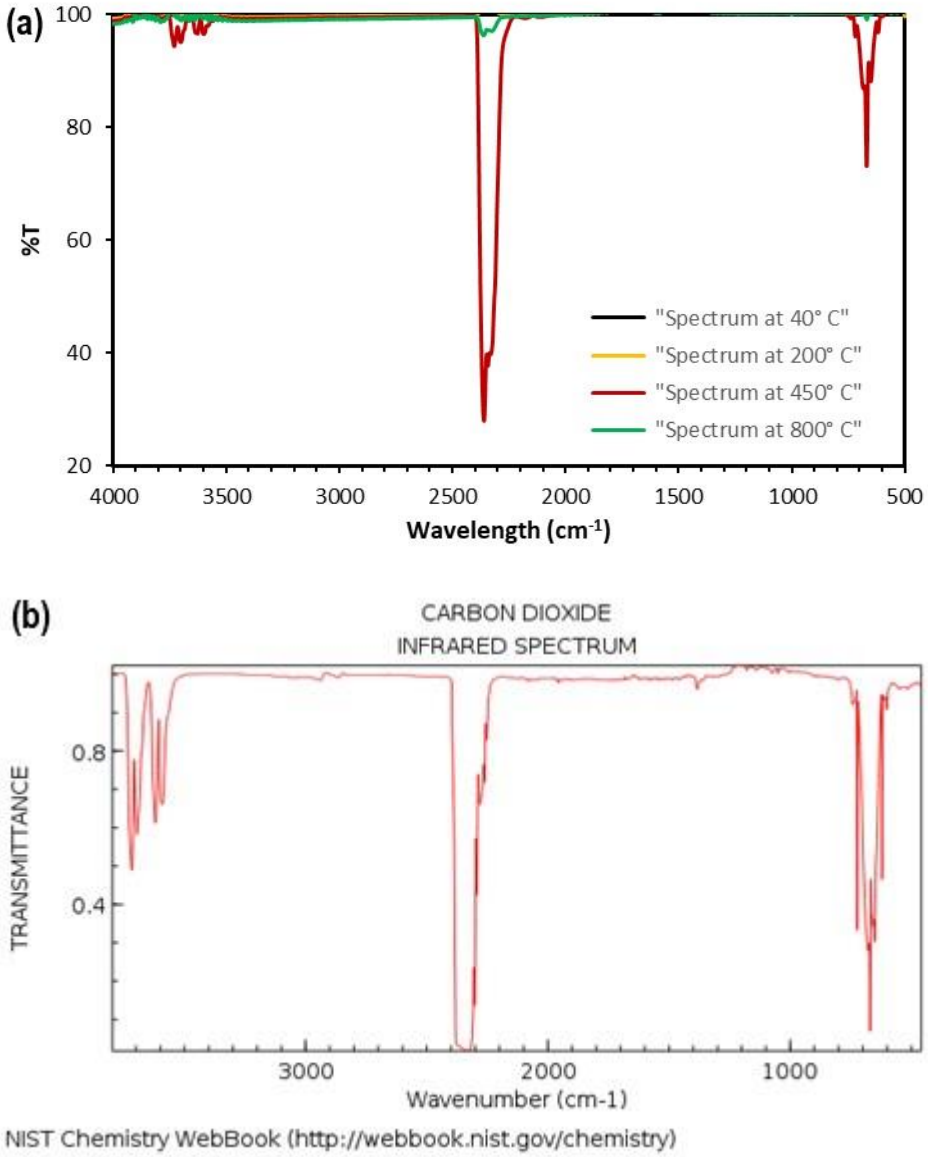

Figure S 21: (a) TGA-IR result of GO and (b) CO_2 spectrum

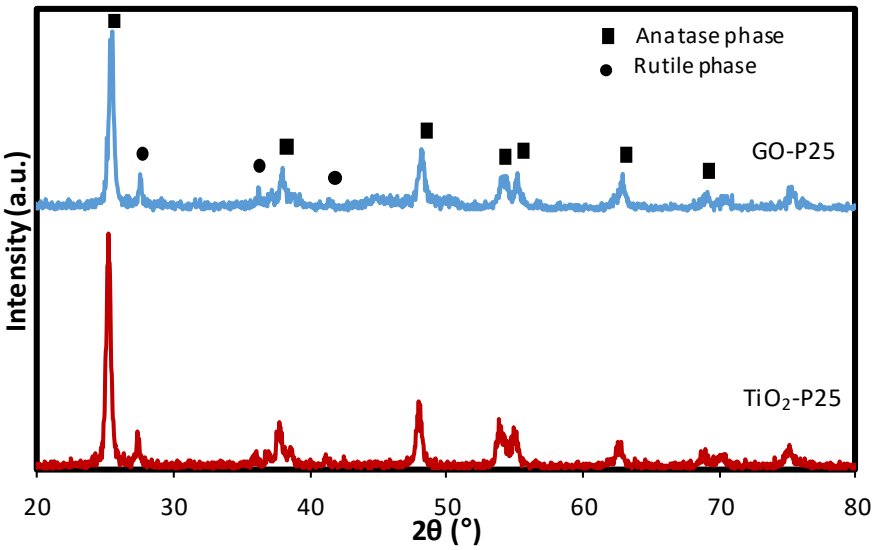

Figure S 22: XRD patterns of TiO2-P25 and GO-P25

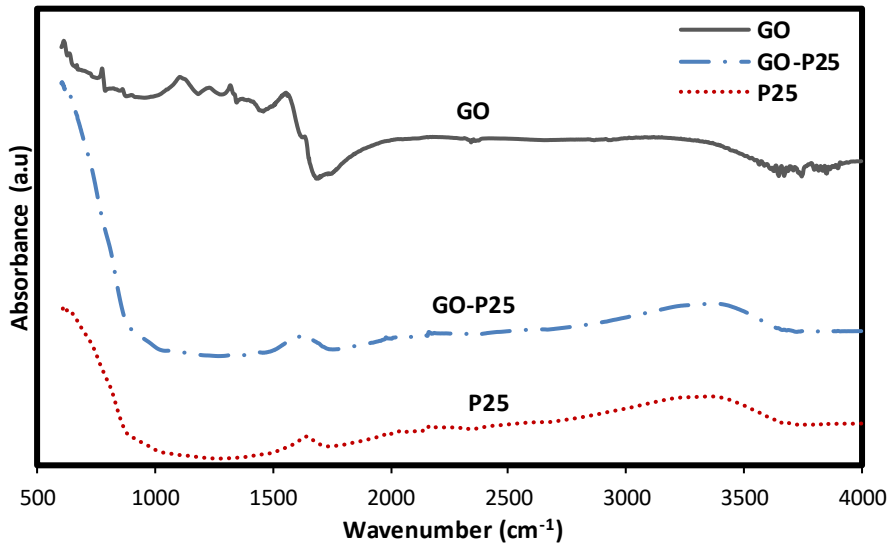

Figure S 23: FTIR spectra of GO, TiO_2-P25, and GO-P25

Table S 1: Surface area of pristine P25, GO, and GO-P25

TiO_2 sample	BET-surface area (m^2/g)
TiO_2-P25	46.89
GO	44.96
GO-P25	54.92

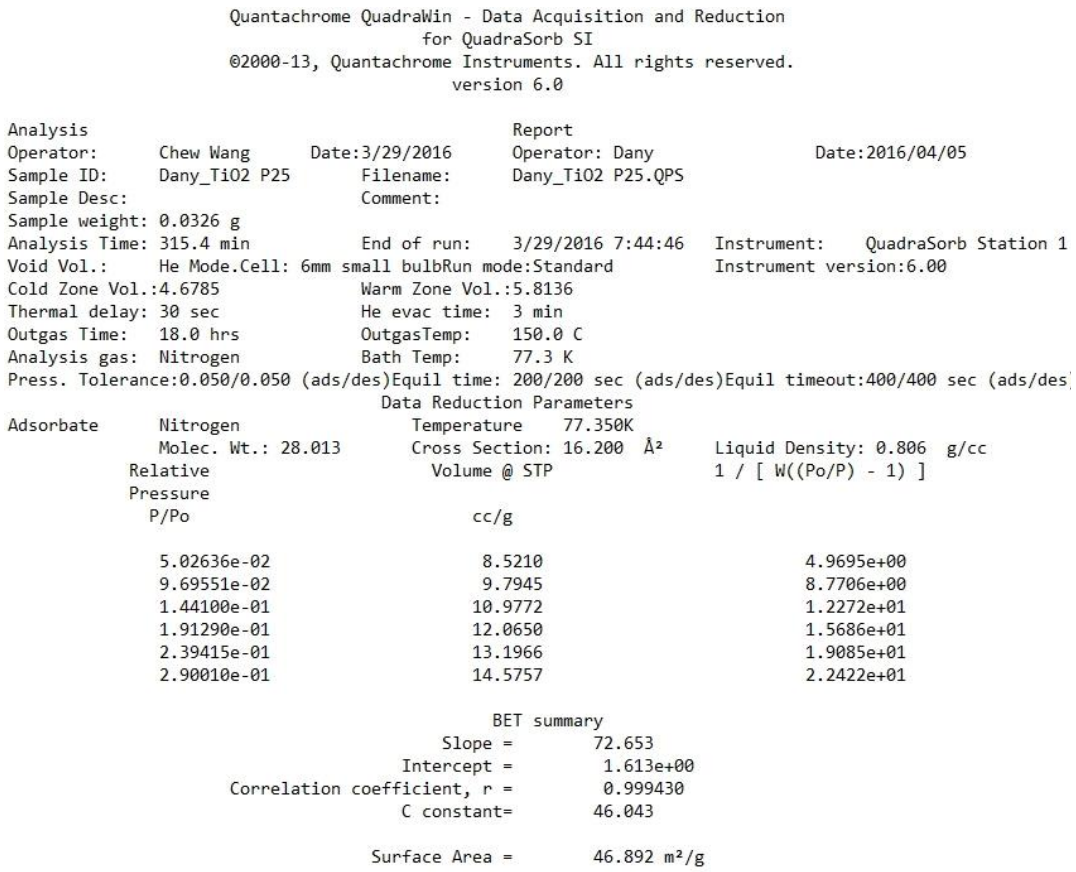

```
                    Quantachrome QuadraWin - Data Acquisition and Reduction
                                    for QuadraSorb SI
                    ©2000-13, Quantachrome Instruments. All rights reserved.
                                      version 6.0

Analysis                                          Report
Operator:      Chew Wang      Date:3/29/2016      Operator: Dany               Date:2016/04/05
Sample ID:     Dany_TiO2 P25       Filename:      Dany_TiO2 P25.QPS
Sample Desc:                       Comment:
Sample weight: 0.0326 g
Analysis Time: 315.4 min           End of run:    3/29/2016 7:44:46   Instrument:    QuadraSorb Station 1
Void Vol.:     He Mode.Cell: 6mm small bulbRun mode:Standard          Instrument version:6.00
Cold Zone Vol.:4.6785              Warm Zone Vol.:5.8136
Thermal delay: 30 sec              He evac time:  3 min
Outgas Time:   18.0 hrs            OutgasTemp:    150.0 C
Analysis gas:  Nitrogen            Bath Temp:     77.3 K
Press. Tolerance:0.050/0.050 (ads/des)Equil time: 200/200 sec (ads/des)Equil timeout:400/400 sec (ads/des)
                                  Data Reduction Parameters
Adsorbate      Nitrogen               Temperature    77.350K
               Molec. Wt.: 28.013     Cross Section: 16.200  Å²     Liquid Density: 0.806  g/cc
            Relative                    Volume @ STP               1 / [ W((Po/P) - 1) ]
            Pressure
              P/Po                          cc/g

               5.02636e-02                   8.5210                        4.9695e+00
               9.69551e-02                   9.7945                        8.7706e+00
               1.44100e-01                  10.9772                        1.2272e+01
               1.91290e-01                  12.0650                        1.5686e+01
               2.39415e-01                  13.1966                        1.9085e+01
               2.90010e-01                  14.5757                        2.2422e+01

                                         BET summary
                                   Slope =        72.653
                                 Intercept =       1.613e+00
                        Correlation coefficient, r =       0.999430
                                 C constant=       46.043

                               Surface Area =       46.892 m²/g
```

Figure S 24: Surface area calculation using BET theory for TiO2-P25

Quantachrome QuadraWin - Data Acquisition and Reduction
for QuadraSorb SI
©2000-13, Quantachrome Instruments. All rights reserved.
version 6.0

Analysis Report
Operator: Chew Wang Date:11/25/2016 Operator: Chew Wang Date:2016/12/12
Sample ID: GO Filename: GO.QPS
Sample Desc: Comment:
Sample weight: 0.1240 g
Analysis Time: 422.4 min End of run: 11/25/2016 6:46:19 Instrument: QuadraSorb Station 4
Void Vol.: He Mode.Cell: 6mm small bulbRun mode:Standard Instrument version:6.00
Cold Zone Vol.:5.3797 Warm Zone Vol.:5.9201
Thermal delay: 30 sec He evac time: 3 min
Outgas Time: 24.0 hrs OutgasTemp: 150.0 C
Analysis gas: Nitrogen Bath Temp: 77.3 K
Press. Tolerance:0.050/0.050 (ads/des)Equil time: 200/200 sec (ads/des)Equil timeout:400/400 sec (ads/des

Data Reduction Parameters

Adsorbate Nitrogen Temperature 77.350K
Molec. Wt.: 28.013 Cross Section: 16.200 Å² Liquid Density: 0.806 g/cc

Relative Pressure P/Po	Volume @ STP cc/g	1 / [W((Po/P) - 1)]
5.25776e-02	-0.0873	-5.0866e+02
1.00415e-01	-0.2346	-3.8077e+02
1.45779e-01	-0.4057	-3.3659e+02
1.95969e-01	-0.6261	-3.1145e+02
2.42326e-01	-0.7599	-3.3677e+02
2.89623e-01	-0.9069	-3.5970e+02

BET summary
Slope = 542.633
Intercept = -4.652e+02
Correlation coefficient, r = 0.680559
C constant= -0.167

Surface Area = 44.960 m²/g

Figure S 25: Surface area calculation using BET theory for GO

Quantachrome QuadraWin - Data Acquisition and Reduction
for QuadraSorb SI
©2000-13, Quantachrome Instruments. All rights reserved.
version 6.0

Analysis			Report		
Operator:	Chew Wang	Date:11/25/2016	Operator: Chew Wang		Date:2016/12/12
Sample ID:	GOP25	Filename:	GOP25.QPS		
Sample Desc:		Comment:			
Sample weight:	0.2116 g				
Analysis Time:	411.2 min	End of run:	11/25/2016 6:35:00	Instrument:	QuadraSorb Station 1
Void Vol.:	He Mode.Cell: 6mm small bulbRun mode:Standard			Instrument version:6.00	
Cold Zone Vol.:	5.5017	Warm Zone Vol.:	5.8845		
Thermal delay:	30 sec	He evac time:	3 min		
Outgas Time:	24.0 hrs	OutgasTemp:	150.0 C		
Analysis gas:	Nitrogen	Bath Temp:	77.3 K		
Press. Tolerance:	0.050/0.050 (ads/des)	Equil time:	200/200 sec (ads/des)	Equil timeout:	400/400 sec (ads/des)

Data Reduction Parameters

Adsorbate	Nitrogen	Temperature	77.350K		
	Molec. Wt.: 28.013	Cross Section:	16.200 Å²	Liquid Density:	0.806 g/cc

Relative Pressure P/Po	Volume @ STP cc/g	1 / [W((Po/P) - 1)]
5.09108e-02	11.4309	3.7547e+00
9.74374e-02	12.6361	6.8357e+00
1.45538e-01	13.8013	9.8745e+00
1.92269e-01	14.9585	1.2732e+01
2.40519e-01	16.1166	1.5722e+01
2.86225e-01	17.2584	1.8591e+01

BET summary

Slope =	62.749
Intercept =	6.586e-01
Correlation coefficient, r =	0.999927
C constant=	96.276
Surface Area =	54.923 m²/g

Figure S 26: Surface area calculation using BET theory for GO-P25

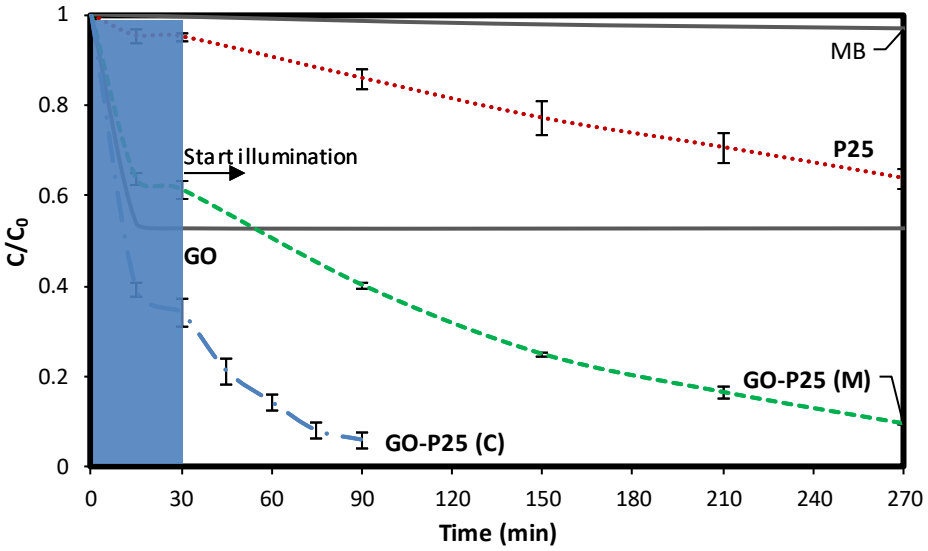

Figure S 27: Comparison of GO-TiO2 activity prepared by chemical synthesis (GO-P25 (C)) and mechanical mixing (GO-P25 (M))

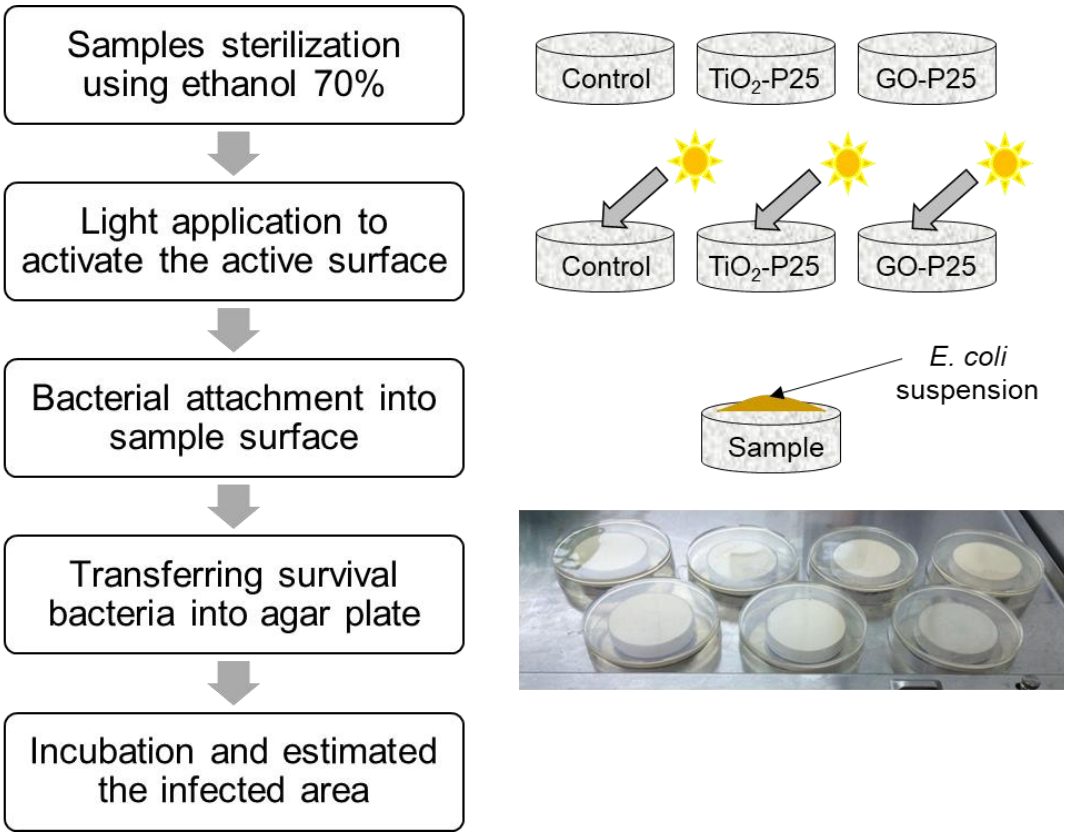

Figure S 28: Experimental procedure for the surface study on anti-bacterial concrete

Visible Light Treatment

0% TiO_2 5% TiO_2 5% GO-TiO_2

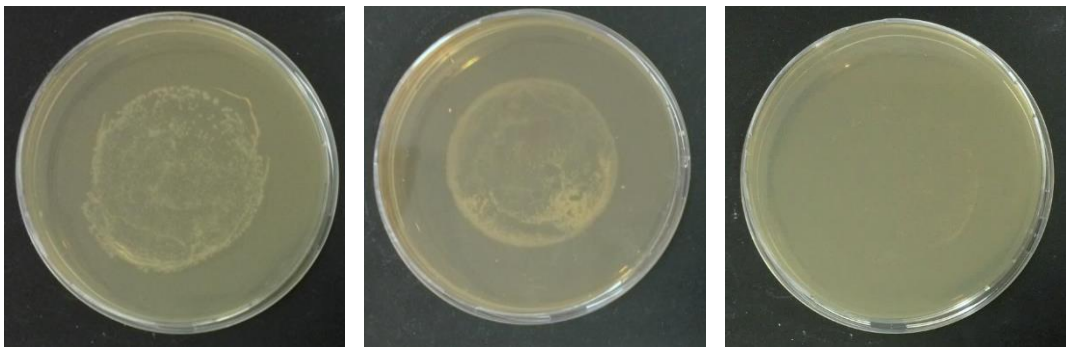

No Light Treatment (Dark Condition)

0% TiO_2 5% TiO_2 5% GO-TiO_2

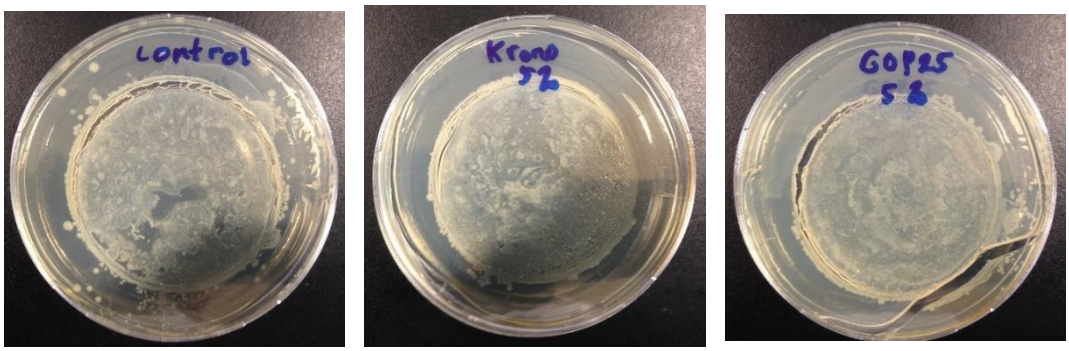

Figure S 29: The viability of E. coli after 24-h incubation

APPENDIX C

Supporting Information

for

Antibacterial potential of cementitious materials containing GO-TiO_2 composites for self-sterilization surface

Calculation of effect estimation

Using the total under the treatment combinations shown in Table 5-2, the factor effects may be estimated as follows:

$$A = \frac{1}{4n}[Contrast_A] = \frac{1}{4n}[a - (1) + ab - b + ac - c + abc - bc]$$

$$= \frac{1}{8}[102\% - 159\% + 120\% - 110\% + 92\% - 157\% + 76\% - 87\%]$$

$$= \frac{1}{8}[-121\%] = -15.2\%$$

$$B = \frac{1}{4n}[Contrast_B] = \frac{1}{4n}[b + ab + bc + abc - (1) - a - c - ac]$$

$$= \frac{1}{8}[-117\%] = -14.6\%$$

$$C = \frac{1}{4n}[Contrast_C] = \frac{1}{4n}[c + ac + bc + abc - (1) - a - b - ab]$$

$$= \frac{1}{8}[-79\%] = -9.9\%$$

$$AB = \frac{1}{4n}[Contrast_{AB}] = \frac{1}{4n}[ab - a - b + (1) + abc - bc - ac + c]$$

$$= \frac{1}{8}[121\%] = 15.1\%$$

$$AC = \frac{1}{4n}[Contrast_{AC}] = \frac{1}{4n}[(1) - a + b - ab - c + ac - bc + abc]$$

$$= \frac{1}{8}[-31\%] = -3.8\%$$

$$BC = \frac{1}{4n}[Contrast_{BC}] = \frac{1}{4n}[(1) + a - b - ab - c - ac + bc + abc]$$

$$= \frac{1}{8}[-55\%] = -6.8\%$$

$$ABC = \frac{1}{4n}[Contrast_{ABC}] = \frac{1}{4n}[(1) + a - b - ab - c - ac + bc + abc]$$

$$= \frac{1}{8}[-12\%] = -1.6\%$$

Calculation of sum of squares

The replicate n is the number of observations at each run, which is equal to two. The sums of squares are calculated as follows:

$$SS_A = \frac{(Contrast_A)^2}{8n} = \frac{(-121\%)^2}{16} = 9.2\%$$

$$SS_B = \frac{(Contrast_B)^2}{8n} = \frac{(-117\%)^2}{16} = 8.5\%$$

$$SS_C = \frac{(Contrast_C)^2}{8n} = \frac{(-79\%)^2}{16} = 3.9\%$$

$$SS_{AB} = \frac{(Contrast_{AB})^2}{8n} = \frac{(121\%)^2}{16} = 9.2\%$$

$$SS_{AC} = \frac{(Contrast_{AC})^2}{8n} = \frac{(-31\%)^2}{16} = 0.6\%$$

$$SS_{BC} = \frac{(Contrast_{BC})^2}{8n} = \frac{(-55\%)^2}{16} = 1.9\%$$

$$SS_{ABC} = \frac{(Contrast_{ABC})^2}{8n} = \frac{(-12\%)^2}{16} = 0.1\%$$

$$SS_T = \sum_{i=1}^{a}\sum_{j=1}^{b}\sum_{k=1}^{c}\sum_{l=1}^{l} y_{ijkl}^2 - \frac{y^2_{\dots}}{abcn} = [(82.5)^2 + (76.1)^2 + \cdots + (50.6)^2] - \frac{902^2}{16}$$

The total sum of squares is SS_T = 42.5% and by subtraction SS_E = 9.1%.

Analysis of variance (ANOVA)

ANOVA is the most important statistic tool used in DOE. Its task is to decide whether and which factors or interactions have significant effect (influence) on the response. Table S 2 ANOVA for a three-factor factorial design shows the ANOVA for a three-factor factorial design.

Table S 2 ANOVA for a three-factor factorial design

Source of Variation	Sum of Square	Degree of freedom	Mean Square	F_0
A	SS_A	a-1	$SS_A/(a-1)$	MS_A/MS_E
B	SS_B	b-1	$SS_B/(b-1)$	MS_B/MS_E
C	SS_C	c-1	$SS_C/(c-1)$	MS_C/MS_E
AB	SS_{AB}	(a-1)(b-1)	$SS_{AB}/(a-1)(b-1)$	MS_{AB}/MS_E
AC	SS_{AC}	(a-1)(c-1)	$SS_{AC}/(a-1)(c-1)$	MS_{AC}/MS_E
BC	SS_{BC}	(b-1)(c-1)	$SS_{BC}/(b-1)(c-1)$	MS_{BC}/MS_E
ABC	SS_{ABC}	(a-1)(b-1)(c-1)	$SS_{ABC}/(a-1)(b-1)(c-1)$	MS_{ABC}/MS_E
Error	SS_E	abc(n-1)	$SS_E/abc(n-1)$	
Total	SS_T	abcn-1	SS_T	

In this case, each factor comprises two levels (a = b = c = 2).

REFERENCES

AGRIOS, A. & PICHAT, P. 2005. State of the art and perspectives on materials and applications of photocatalysis over TiO2. *Applied Electrochemistry,* 35**,** 655-663.

AHMADI, N., NEMATI, A. & BAGHERZADEH, M. 2018. Synthesis and properties of Ce-doped TiO2-reduced graphene oxide nanocomposite. *Journal of Alloys and Compounds,* 742**,** 986-995.

AKHTER, P., HUSSAIN, M., SARACCO, G. & RUSSO, N. 2015. Novel nanostructured-TiO2 materials for the photocatalytic reduction of CO2 greenhouse gas to hydrocarbons and syngas. *Fuel,* 149**,** 55-65.

ALBRIGHT, J. F. & GOLDSTEIN, R. A. 1996. Airborne Pollutants and the Immune System. *Otolaryngology–Head and Neck Surgery,* 114**,** 232-238.

AMORY, D. E. & ROUXHET, P. G. 1988. Surface properties of Saccharomyces cerevisiae and Saccharomyces carlbergensis: chemical composition, electrostatic charge and hydrophobicity. *Biochimica et Biophysica Acta (BBA) - Biomembranes,* 938**,** 61-70.

ARANDIGOYEN, M., BICER-SIMSIR, B., ALVAREZ, J. I. & LANGE, D. A. 2006. Variation of microstructure with carbonation in lime and blended pastes. *Applied Surface Science,* 252**,** 7562-7571.

ASAKA RIKEN CO., L. Available: https://www.asaka.co.jp/english/environmental/02.html [Accessed 22 September 2018].

ASHBY, M. F. & MEDALIST, R. F. M. 1983. The mechanical properties of cellular solids. *Metallurgical Transactions A,* 14**,** 1755-1769.

ASSOCIATION, P. C. 2002. Types and causes of concrete deterioration. *PCA R&D Serial No. 2617* [Online].

BANERJEE, S., DIONYSIOU, D. D. & PILLAI, S. C. 2015. Self-cleaning applications of TiO2 by photo-induced hydrophilicity and photocatalysis. *Applied Catalysis B: Environmental,* 176–177**,** 396-428.

BO YEON, L. & KURTIS, K. E. 2010. Influence of TiO_2 Nanoparticles on Early C_3S Hydration. *Journal of the American Ceramic Society,* 93**,** 3399-3405.

BOONEN, E., AKYLAS, V., BARMPAS, F., BORÉAVE, A., BOTTALICO, L., CAZAUNAU, M., CHEN, H., DAËLE, V., DE MARCO, T., DOUSSIN, J. F., GAIMOZ, C., GALLUS, M., GEORGE, C., GRAND, N., GROSSELIN, B., GUERRINI, G. L., HERRMANN, H., IFANG, S., KLEFFMANN, J., KURTENBACH, R., MAILLE, M., MANGANELLI, G., MELLOUKI, A., MIET, K., MOTHES, F., MOUSSIOPOULOS, N., POULAIN, L., RABE, R., ZAPF, P. & BEELDENS, A. 2015. Construction of a photocatalytic de-polluting field site in the Leopold II tunnel in Brussels. *Journal of Environmental Management,* 155**,** 136-144.

BOONEN, E. & BEELDENS, A. 2013. Photocatalytic roads: from lab tests to real scale applications. *European Transport Research Review***,** 79.

BOUBAKER, K. 2011. A physical explanation to the controversial Urbach tailing universality. *The European Physical Journal Plus,* 126**,** 10.

BRASLAVSKY, S. E. 2007. Glossary of terms used in photochemistry, 3rd edition (IUPAC Recommendations 2006). *Pure & Applied Chemistry,* 79**,** 293-465.

BUTMAN, M. F., OVCHINNIKOV, N. L., KARASEV, N. S., KOCHKINA, N. E., AGAFONOV, A. V. & VINOGRADOV, A. V. 2018. Photocatalytic and adsorption properties of TiO2-pillared montmorillonite obtained by hydrothermally activated intercalation of titanium polyhydroxo complexes. *Beilstein Journal of Nanotechnology,* 9**,** 364-378.

CABIR, B., YURDERI, M., CANER, N., AGIRTAS, M. S., ZAHMAKIRAN, M. & KAYA, M. 2017. Methylene blue photocatalytic degradation under visible light irradiation on copper phthalocyanine-sensitized TiO2 nanopowders. *Materials Science and Engineering: B,* 224**,** 9-17.

CARP, O., HUISMAN, C. L. & RELLER, A. 2004. Photoinduced reactivity of titanium dioxide. *Progress in Solid State Chemistry,* 32**,** 33-177.

CARRE, G., ESTNER, M., GIES, J.-P., ANDRE, P., HAMON, E., ENNAHAR, S., KELLER, V., KELLER, N., LETT, M.-C. & HORVATOVICH, P. 2014. TiO2 Photocatalysis Damages Lipids and Proteins in Escherichia coli. *APPLIED AND ENVIRONMENTAL MICROBIOLOGY,* 80**,** 2573-2581.

CASSAR, L. 2004. Photocatalysis of Cementitious Materials: Clean Buildings and Clean Air. *MRS Bulletin,* 29**,** 328-331.

CASSAR, L., BEELDENS, A., PIMPINELLI, N. & GUERRINI, G. L. Photocatalysis of cementitious materials. *In:* BAGLIONI, P. & CASSSAR, L., eds. International RILEM Symposium on Photocatalysis, Environment and Construction Material, 2007. RILEM Publications SARL, 131 - 145.

CHANG, S.-S., CLAIR, B., RUELLE, J., BEAUCHÊNE, J., RENZO, F. D., QUIGNARD, F., GUANG-JIE, Z., YAMAMOTO, H. & GRIL, J. 2009. Mesoporosity as a new parameter for understanding tension stress generation in trees. *Journal of Experimental Botany,* 60**,** 3023-3030.

CHEN, C., CAI, W., LONG, M., ZHOU, B., WU, Y., WU, D. & FENG, Y. 2010. Synthesis of Visible-Light Responsive Graphene Oxide/TiO2 Composites with p/n Heterojunction. *ACS Nano,* 4**,** 6425-6432.

CHEN, C., LONG, M., ZENG, H., CAI, W., ZHOU, B., ZHANG, J., WU, Y., DING, D. & WU, D. 2009. Preparation, characterization and visible-light activity of carbon modified TiO2 with two kinds of carbonaceous species. *Journal of Molecular Catalysis. A, Chemical,* 314**,** 35-41.

CHEN, J. & POON, C.-S. 2009a. Photocatalytic Cementitious Materials: Influence of the Microstructure of Cement Paste on Photocatalytic Pollution Degradation. *Environmental Science & Technology,* 43**,** 8948-8952.

CHEN, J. & POON, C. S. 2009b. Photocatalytic construction and building materials: From fundamentals to applications. *Building and Environment,* 44**,** 1899-1906.

CHOUDHURY, B. & CHOUDHURY, A. 2014. Oxygen defect dependent variation of band gap, Urbach energy and luminescence property of anatase, anatase–rutile mixed phase and of rutile phases of TiO2 nanoparticles. *Physica E: Low-dimensional Systems and Nanostructures,* 56**,** 364-371.

CRUZ-ORTIZ, B. R., HAMILTON, J. W. J., PABLOS, C., DÍAZ-JIMÉNEZ, L., CORTÉS-HERNÁNDEZ, D. A., SHARMA, P. K., CASTRO-ALFÉREZ, M., FERNÁNDEZ-IBAÑEZ, P., DUNLOP, P. S. M. & BYRNE, J. A. 2017. Mechanism of photocatalytic disinfection using titania-graphene composites under UV and visible irradiation. *Chemical Engineering Journal,* 316**,** 179-186.

DAI, M. 1994. The Effect of Zeta Potential of Activated Carbon on the Adsorption of Dyes from Aqueous Solution. *Journal of Colloid and Interface Science,* 164**,** 223.

DALY, M. J., GAIDAMAKOVA, E. K., MATROSOVA, V. Y., VASILENKO, A., ZHAI, M., LEAPMAN, R. D., LAI, B., RAVEL, B., LI, S.-M. W., KEMNER, K. M. & FREDRICKSON, J. K. 2007. Protein Oxidation Implicated as the Primary Determinant of Bacterial Radioresistance. *PLOS Biology,* 5**,** e92.

DAVIDSON, H., POON, M., SAUNDERS, R., SHAPIRO, I. M., HICKOK, N. J. & ADAMS, C. S. 2015. Tetracycline tethered to titanium inhibits colonization by Gram-negative bacteria. *Journal of Biomedical Materials Research Part B: Applied Biomaterials,* 103**,** 1381-1389.

DEVAHASDIN, S., FAN, J. C., LI, K. & CHEN, D. H. 2003. TiO2 photocatalytic oxidation of nitric oxide: transient behavior and reaction kinetics. *Journal of Photochemistry & Photobiology, A: Chemistry,* 156**,** 161-170.

DIAS, W. P. S. 2000. Reduction of concrete sorptivity with age through carbonation. *Cement and Concrete Research,* 30**,** 1255-1261.

DING, S., CHEN, J. S., LUAN, D., BOEY, F. Y. C., MADHAVI, S. & LOU, X. W. 2011. Graphene-supported anatase TiO2 nanosheets for fast lithium storage. *Chemical Communications,* 47**,** 5780-5782.

DING, Y., PENG, N., DU, Y., JI, L. & CAO, B. 2014a. Disruption of putrescine biosynthesis in Shewanella oneidensis enhances biofilm cohesiveness and performance in Cr(VI) immobilization. *Applied And Environmental Microbiology,* 80**,** 1498-1506.

DING, Y. Z., PENG, N., DU, Y. H., JI, L. H. & CAO, B. 2014b. Disruption of Putrescine Biosynthesis in Shewanella oneidensis Enhances Biofilm Cohesiveness and Performance in Cr(VI) Immobilization. *Applied and Environmental Microbiology,* 80**,** 1498-1506.

DU, A., NG, Y. H., BELL, N. J., ZHU, Z., AMAL, R. & SMITH, S. C. 2011. Hybrid Graphene/Titania Nanocomposite: Interface Charge Transfer, Hole Doping, and Sensitization for Visible Light Response. *The Journal of Physical Chemistry Letters,* 2**,** 894-899.

ENDO, M., WEI, Z., WANG, K., KARABIYIK, B., YOSHIIRI, K., ROKICKA, P., OHTANI, B., MARKOWSKA-SZCZUPAK, A. & KOWALSKA, E. 2018. Noble metal-modified titania with visible-light activity for the decomposition of microorganisms. *Beilstein Journal of Nanotechnology,* 9**,** 829-841.

ENTRADAS, T., CABRITA, J. F., DALUI, S., NUNES, M. R., MONTEIRO, O. C. & SILVESTRE, A. J. 2014. Synthesis of sub-5 nm Co-doped SnO2 nanoparticles and their structural, microstructural, optical and photocatalytic properties. *Materials Chemistry and Physics,* 147**,** 563-571.

EVANS, R. C., DOUGLAS, P. & BURROW, H. D. 2013. *Applied Photochemistry [electronic resource] / edited by Rachel C. Evans, Peter Douglas, Hugh D. Burrow,* Dordrecht : Springer Netherlands : Imprint: Springer, 2013.

FAN, Y., LU, H.-T., LIU, J.-H., YANG, C.-P., JING, Q.-S., ZHANG, Y.-X., YANG, X.-K. & HUANG, K.-J. 2011. Hydrothermal preparation and electrochemical sensing properties of TiO2–graphene nanocomposite. *Colloids and Surfaces B: Biointerfaces,* 83**,** 78-82.

FLEMMING, H. C. & WINGENDER, J. 2010. The biofilm matrix. *Nature Reviews Microbiology,* 8**,** 623-633.

FOLLI, A., POCHARD, I., NONAT, A., JAKOBSEN, U. H., SHEPHERD, A. M. & MACPHEE, D. E. 2010. Engineering Photocatalytic Cements: Understanding TiO_2 Surface Chemistry to Control and Modulate Photocatalytic Performances. *Journal of the American Ceramic Society,* 93**,** 3360-3369.

FONSECA, A. J., PINA, F., MACEDO, M. F., LEAL, N., ROMANOWSKA-DESKINS, A., LAIZ, L., GÓMEZ-BOLEA, A. & SAIZ-JIMENEZ, C. 2010. Anatase as an alternative application for preventing biodeterioration of mortars: Evaluation and comparison with other biocides. *International Biodeterioration & Biodegradation,* 64**,** 388-396.

FOSTER, H. A., DITTA, I. B., VARGHESE, S. & STEELE, A. 2011. Photocatalytic disinfection using titanium dioxide: spectrum and mechanism of antimicrobial activity. *Applied Microbiology and Biotechnology,* 90**,** 1847-1868.

FU, X., CLARK, L. A., ZELTNER, W. A. & ANDERSON, M. A. 1996. Effects of reaction temperature and water vapor content on the heterogeneous

photocatalytic oxidation of ethylene. *Journal of Photochemistry and Photobiology A: Chemistry,* 97**,** 181-186.

FUJISHIMA, A. & HONDA, K. 1972. Electrochemical Photolysis of Water at a Semiconductor Electrode. *Nature,* 238**,** 37-38.

FUJISHIMA, A., RAO, T. N. & TRYK, D. A. 2000. Titanium dioxide photocatalysis. *Journal of Photochemistry & Photobiology, C: Photochemistry Reviews,* 1**,** 1-21.

FUJISHIMA, A. & ZHANG, X. 2006. Account / Revue: Titanium dioxide photocatalysis: present situation and future approaches. *Comptes rendus - Chimie,* 9**,** 750-760.

FUJISHIMA, A., ZHANG, X. & TRYK, D. A. 2007. Heterogeneous photocatalysis: From water photolysis to applications in environmental cleanup. *International Journal of Hydrogen Energy,* 32**,** 2664-2672.

FUJISHIMA, A., ZHANG, X. T. & TRYK, D. A. 2008. TiO_2 photocatalysis and related surface phenomena. *Surface Science Report,* 63**,** 515-582.

GALLUS, M., AKYLAS, V., BARMPAS, F., BEELDENS, A., BOONEN, E., BORÉAVE, A., CAZAUNAU, M., CHEN, H., DAËLE, V., DOUSSIN, J. F., DUPART, Y., GAIMOZ, C., GEORGE, C., GROSSELIN, B., HERRMANN, H., IFANG, S., KURTENBACH, R., MAILLE, M., MELLOUKI, A., MIET, K., MOTHES, F., MOUSSIOPOULOS, N., POULAIN, L., RABE, R., ZAPF, P. & KLEFFMANN, J. 2015. Photocatalytic de-pollution in the Leopold II tunnel in Brussels: NOx abatement results. *Building and Environment,* 84**,** 125-133.

GIANNANTONIO, D. J., KURTH, J. C., KURTIS, K. E. & SOBECKY, P. A. 2009. Effects of concrete properties and nutrients on fungal colonization and fouling. *International Biodeterioration & Biodegradation,* 63**,** 252-259.

GOGNIAT, G. & DUKAN, S. 2007. TiO₂ Photocatalysis Causes DNA Damage via Fenton Reaction-Generated Hydroxyl Radicals during the Recovery Period. *Applied and Environmental Microbiology,* 73**,** 7740-7743.

GRAZIANI, L., QUAGLIARINI, E., BONDIOLI, F. & D'ORAZIO, M. 2014. Durability of self-cleaning TiO2 coatings on fired clay brick façades: Effects

of UV exposure and wet & dry cycles. *Building and Environment,* 71**,** 193-203.

GREEN MILLENNIUM. 2018. *OUTDOOR / EXTERIOR APPLICATION* [Online]. Available: http://www.greenmillennium.com/outdoor-exterior/ [Accessed 16 July 2018].

GU, J.-D., FORD, T. E., BERKE, N. S. & MITCHELL, R. 1998. Biodeterioration of concrete by the fungus Fusarium. *International Biodeterioration & Biodegradation,* 41**,** 101-109.

GUAN, K. 2005. Relationship between photocatalytic activity, hydrophilicity and self-cleaning effect of TiO2/SiO2 films. *Surface and Coatings Technology,* 191**,** 155-160.

GUERRINI, G. L. 2012. Photocatalytic performances in a city tunnel in Rome: NO_x monitoring results. *Construction and Building Materials,* 27**,** 165-175.

GUO, J., ZHU, S., CHEN, Z., LI, Y., YU, Z., LIU, Q., LI, J., FENG, C. & ZHANG, D. 2011. Sonochemical synthesis of TiO2 nanoparticles on graphene for use as photocatalyst. *Ultrasonics Sonochemistry,* 18**,** 1082-1090.

GUO, M.-Z., LING, T.-C. & POON, C. S. 2017. Photocatalytic NOx degradation of concrete surface layers intermixed and spray-coated with nano-TiO2: Influence of experimental factors. *Cement and Concrete Composites,* 83**,** 279-289.

GUO, M.-Z., MAURY-RAMIREZ, A. & POON, C. S. 2016. Note from the field: Self-cleaning ability of titanium dioxide clear paint coated architectural mortar and its potential in field application. *Journal of Cleaner Production,* 112**,** 3583-3588.

GUO, M.-Z. & POON, C.-S. 2013. Photocatalytic NO removal of concrete surface layers intermixed with TiO2. *Building and Environment,* 70**,** 102-109.

GUO, M. Z., LING, T. C. & POON, C. S. 2013. Nano-TiO_2-based architectural mortar for NO removal and bacteria inactivation: Influence of coating and weathering conditions. *CEMENT AND CONCRETE COMPOSITES,* 36**,** 102-109.

GUSTAFSON, K. E. & DICKHUT, R. M. 1997. Particle/gas concentrations and distributions of PAHs in the atmosphere of southern Chesapeake Bay. *Environmental science & technology*.

GUTTERIDGE, W. A. & DALZIEL, J. A. 1990. Filler cement: The effect of the secondary component on the hydration of Portland cement. *Cement and Concrete Research,* 20**,** 778-782.

HAGFELDT, A. & GRATZEL, M. 1995. Light-induced redox reactions in nanocrystalline systems. *Chemical Reviews***,** 49.

HARRISON, J. J., TREMAROLI, V., STAN, M. A., CHAN, C. S., VACCHI-SUZZI, C., HEYNE, B. J., PARSEK, M. R., CERI, H. & TURNER, R. J. 2009. Chromosomal antioxidant genes have metal ion-specific roles as determinants of bacterial metal tolerance. *Environmental Microbiology,* 11**,** 2491-2509.

HERRMANN, J. M., TAHIRI, H., AIT-ICHOU, Y., LASSALETTA, G., GONZÁLEZ-ELIPE, A. R. & FERNÁNDEZ, A. 1997. Characterization and photocatalytic activity in aqueous medium of TiO2 and Ag-TiO2 coatings on quartz. *Applied Catalysis B, Environmental,* 13**,** 219-228.

HIRAKAWA, T. & NOSAKA, Y. 2002. Properties of O2•- and OH• Formed in TiO2 Aqueous Suspensions by Photocatalytic Reaction and the Influence of H2O2 and Some Ions. *Langmuir,* 18**,** 3247-3254.

HOFFMANN, M. R., MARTIN, S. T., CHOI, W. & BAHNEMANN, D. W. 1995. Environmental applications of semiconductor photocatalysis. *Chemical Reviews***,** 69-96.

HUANG, X., RANADE, R., ZHANG, Q., NI, W. & LI, V. C. 2013. Mechanical and thermal properties of green lightweight engineered cementitious composites. *Construction and Building Materials,* 48**,** 954-960.

HUANG, Z., MANESS, P.-C., BLAKE, D. M., WOLFRUM, E. J., SMOLINSKI, S. L. & JACOBY, W. A. 2000. Bactericidal mode of titanium dioxide photocatalysis. *Journal of Photochemistry & Photobiology, A: Chemistry,* 130**,** 163-170.

IBUSUKI, T. & TAKEUCHI, K. 1986. Toluene oxidation on u.v.-irradiated titanium dioxide with and without O2, NO2 OR H2O at ambient temperature. *Atmospheric Environment (1967),* 20**,** 1711-1715.

IKHMAYIES, S. J. & AHMAD-BITAR, R. N. 2013. A study of the optical bandgap energy and Urbach tail of spray-deposited CdS:In thin films. *Journal of Materials Research and Technology,* 2**,** 221-227.

IMLAY, J. A. 2003. Pathways of Oxidative Damage. *Annual Review of Microbiology,* 57**,** 395-418.

JANI, R. B., EGGLESTON, C. M., COLBERG, P. J. S., SHI, L. & REARDON, C. J. 2010. Microbial fuel cell study of the role of OmcA and MtrC in electron transfer from Shewanella oneidensis to oxide electrodes. *GEOCHIMICA ET COSMOCHIMICA ACTA,* 74**,** A457-A457.

JAYAPALAN, A. R., BO YEON, L., LAND, E. M., BERGIN, M. H. & KURTIS, K. E. 2015. Photocatalytic Efficiency of Cement-Based Materials: Demonstration of Proposed Test Method. *ACI Materials Journal,* 112**,** 219.

JIANG, J., OBERDORSTER, G. & BISWAS, P. 2009. Characterization of size, surface charge, and agglomeration state of nanoparticle dispersions for toxicological studies. *Journal of Nanoparticle Research: An Interdisciplinary Forum for Nanoscale Science and Technology***,** 77.

JIMENEZ-RELINQUE, E., LLORENTE, I. & CASTELLOTE, M. 2017. TiO2 cement-based materials: Understanding optical properties and electronic band structure of complex matrices. *Catalysis Today,* 287**,** 203-209.

JO, W.-K. & KANG, H.-J. 2013. Titanium dioxide–graphene oxide composites with different ratios supported by Pyrex tube for photocatalysis of toxic aromatic vapors. *Powder Technology,* 250**,** 115-121.

JOHANNESSON, B. & UTGENANNT, P. 2001. Microstructural changes caused by carbonation of cement mortar. *Cement and Concrete Research,* 31**,** 925-931.

JOOST, U., JUGANSON, K., VISNAPUU, M., MORTIMER, M., KAHRU, A., NOMMISTE, E., JOOST, U., KISAND, V. & IVASK, A. 2015. Photocatalytic antibacterial activity of nano-TiO2 (anatase)-based thin films: Effects on Escherichia coli cells and fatty acids. *Journal of Photochemistry and Photobiology B-Biology,* 142**,** 178-185.

JUN, C. & CHI-SUN, P. 2009. Photocatalytic Cementitious Materials: Influence of the Microstructure of Cement Paste on Photocatalytic Pollution Degradation. *Environmental Science & Technology,* 43**,** 8948-8952.

KAMAT, P. V. 1993. Photochemistry on nonreactive and reactive (semiconductor) surfaces. *Chemical Reviews***,** 267.

KARACA, S., GÜRSES, A., AÇıKYıLDıZ, M. & EJDER, M. 2008. Adsorption of cationic dye from aqueous solutions by activated carbon. *Microporous and Mesoporous Materials,* 115**,** 376-382.

KARAPATI, S., GIANNAKOPOULOU, T., TODOROVA, N., BOUKOS, N., ANTIOHOS, S., PAPAGEORGIOU, D., CHANIOTAKIS, E., DIMOTIKALI, D. & TRAPALIS, C. 2014. TiO2 functionalization for efficient NOx removal in photoactive cement. *Applied Surface Science,* 319**,** 29-36.

KAZUHITO, H., HIROSHI, I. & AKIRA, F. 2005. TiO_2 Photocatalysis: A Historical Overview and Future Prospects. *Japanese journal of applied physics. Part. 1, Regular papers, brief communications & review papers : JJAP*.

KIRK, R. E., OTHMER, D. F., KROSCHWITZ, J. I. & HOWE-GRANT, M. 1991. *Encyclopedia of chemical technology*, New York : Wiley, c1991-<c1996> 4th ed.

KIWI, J. & NADTOCHENKO, V. 2005. Evidence for the mechanism of photocatalytic degradation of the bacterial wall membrane at the TiO2 interface by ATR-FTIR and laser kinetic spectroscopy. *Langmuir,* 21**,** 4631-4641.

KLAEWKLA, R., AREND, M. & HÖLDERICH, W. 2011. *A Review of Mass Transfer Controlling the Reaction Rate in Heterogeneous Catalytic Systems*.

KOJIMA, S., SAKATA, N. & KANDA, T. 2004. *Application of direct sprayed ECC for retrofitting dam structure surface application for mitaka-dam.*

KRISHNAN, P., ZHANG, M.-H., YU, L. & FENG, H. 2013. Photocatalytic degradation of particulate pollutants and self-cleaning performance of TiO2-containing silicate coating and mortar. *Construction and Building Materials,* 44**,** 309-316.

KUBACKA, A., DIEZ, M. S., ROJO, D., BARGIELA, R., CIORDIA, S., ZAPICO, I., ALBAR, J. P., BARBAS, C., MARTINS DOS SANTOS, V. A. P., FERNÁNDEZ-GARCÍA, M. & FERRER, M. 2014. Understanding the antimicrobial mechanism of TiO2-based nanocomposite films in a pathogenic bacterium. *Scientific Reports,* 4**,** 4134.

LACKHOFF, M., PRIETO, X., NESTLE, N., DEHN, F. & NIESSNER, R. 2003. Photocatalytic activity of semiconductor-modified cement—influence of semiconductor type and cement ageing. *Applied Catalysis B, Environmental,* 43**,** 205-216.

LEE, B. Y., JAYAPALAN, A. R., BERGIN, M. H. & KURTIS, K. E. 2014. Photocatalytic cement exposed to nitrogen oxides: Effect of oxidation and binding. *Cement and Concrete Research***,** 30.

LEMIRE, J. A., HARRISON, J. J. & TURNER, R. J. 2013. Antimicrobial activity of metals: mechanisms, molecular targets and applications. *Nature Reviews Microbiology,* 11**,** 371.

LEPECH, M. D. & LI, V. C. 2006. Long term durability performance of engineered cementitious composites. *Journal of Restoration of Buildings and Monuments,* 12**,** 119-132.

LETTMANN, C., HILDENBRAND, K., KISCH, H., MACYK, W. & MAIER, W. F. 2001. Visible light photodegradation of 4-chlorophenol with a coke-containing titanium dioxide photocatalyst. *Applied Catalysis B, Environmental,* 32**,** 215-227.

LEUNG, M. & CHAN, A. H. S. 2006. Control and management of hospital indoor air quality. *Medical Science Monitor,* 12**,** Sr17-Sr23.

LEWIN, R. 1984. Microbial adhesion is a sticky problem. *Science,* 224**,** 375-377.

LI, V. 2008. Engineered Cementitious Composites (ECC) – Material, Structural, and Durability Performance. *In:* NAWY, E. G. (ed.) *Concrete Construction Engineering Handbook.* Boca Raton: CRC Press.

LI, V. C. 1998. Engineered Cementitious Composites - Tailored Composites Through Micromechanical Modeling. *In:* N. BANTHIA, A. B., AND A. MUFTI (ed.) *Fiber Reinforced Concrete: Present and the Future.* Canadian Society for Civil Engineering, Montreal.

LI, V. C. 2003. On Engineered Cementitious Composites (ECC) A Review of the Material and Its Applications. *Journal of Advanced Concrete Technology,* 1**,** 215-230.

LI, V. C., WANG, S. & WU, C. 2001. Tensile strain-hardening behavior or polyvinyl alcohol engineered cementitious composite (PVA-ECC). *ACI Materials Journal,* 98**,** 483-492.

LI, W., WANG, F., FENG, S., WANG, J., SUN, Z., LI, B., LI, Y., YANG, J., ELZATAHRY, A. A., XIA, Y. & ZHAO, D. 2013. Sol–Gel Design Strategy for Ultradispersed TiO2 Nanoparticles on Graphene for High-Performance Lithium Ion Batteries. *Journal of the American Chemical Society,* 135**,** 18300-18303.

LI, Y., YAN, J., SU, Q., XIE, E. & LAN, W. 2014. Preparation of Graphene–TiO2 nanotubes/nanofibers composites as an enhanced visible light photocatalyst using a hybrid synthetic strategy. *Materials Science in Semiconductor Processing,* 27**,** 695-701.

LINSEBIGLER, A. L., LU, G. & YATES, J. T., JR. 1995. Photocatalysis on TiO_2 surfaces: principles, mechanisms, and selected results. *Chemical Reviews***,** 735.

LIU, J., ZHU, W., YU, S. & YAN, X. 2014. Three dimensional carbogenic dots/TiO2 nanoheterojunctions with enhanced visible light-driven photocatalytic activity. *Carbon,* 79**,** 369-379.

LORENZETTI, M., DOGŠA, I., STOŠICKI, T., STOPAR, D., KALIN, M., KOBE, S. & NOVAK, S. 2015. The Influence of Surface Modification on Bacterial Adhesion to Titanium-Based Substrates. *ACS Applied Materials & Interfaces,* 7**,** 1644-1651.

LOWER, B. H., LOWER, S. K., YONGSUNTHON, R., SHI, L., REARDON, C. L., PINCHUK, G. E., UBAY, T. C. D., WILDLING, L., GRUBER, H. J., WIGGINTON, N. S. & BOILY, J. F. 2009. Antibody recognition force microscopy shows that outer membrane cytochromes OmcA and MtrC are expressed on the exterior surface of Shewanella oneidensis MR-1. *Applied and Environmental Microbiology,* 75**,** 2931-2935.

LUCAS, S. S., FERREIRA, V. M. & DE AGUIAR, J. L. B. 2013. Incorporation of titanium dioxide nanoparticles in mortars — Influence of microstructure in the hardened state properties and photocatalytic activity. *Cement and Concrete Research,* 43**,** 112-120.

LUSHCHAK, V. 2010. *Adaptive response to oxidative stress: Bacteria, fungi, plants and animals*.

MACKENZIE, J. D. 1988. Applications of the sol-gel process. *Journal of Non-Crystalline Solids,* 100**,** 162-168.

MAMBA, G., MBIANDA, X. Y. & MISHRA, A. K. 2014. Gadolinium nanoparticle-decorated multiwalled carbon nanotube/titania nanocomposites for degradation of methylene blue in water under simulated solar light. *Environmental Science and Pollution Research,* 21**,** 5597-5609.

MARTINEZ, T., BERTRON, A., ESCADEILLAS, G. & RINGOT, E. 2014a. Algal growth inhibition on cement mortar: Efficiency of water repellent and photocatalytic treatments under UV/VIS illumination. *International Biodeterioration & Biodegradation,* 89**,** 115-125.

MARTINEZ, T., BERTRON, A., ESCADEILLAS, G., RINGOT, E. & SIMON, V. 2014b. BTEX abatement by photocatalytic TiO_2-bearing coatings applied to cement mortars. *Building and Environment,* 71**,** 186-192.

MARUTA, M., KANDA, T., NAGAI, S. & YAMAMOTO, Y. 2005. *New high-rise RC structure using pre-cast ECC coupling beam*.

MAURY-RAMIREZ, A., DE MUYNCK, W., STEVENS, R., DEMEESTERE, K. & DE BELIE, N. 2013. Titanium dioxide based strategies to prevent algal fouling on cementitious materials. *Cement and Concrete Composites,* 36**,** 93-100.

MAURY, A. & DE BELIE, N. 2010. State of the art of TiO_2 containing cementitious materials: self-cleaning properties. *MATERIALES DE CONSTRUCCION,* 60**,** 33-50.

MAURYA, I. C., NEETU, GUPTA, A. K., SRIVASTAVA, P. & BAHADUR, L. 2016. Natural Dye Extracted From Saraca asoca Flowers as Sensitizer for TiO2-Based Dye-Sensitized Solar Cell. *Journal of Solar Energy Engineering,* 138**,** 051006-051006-6.

MEILLE, S., LOMBARDI, M., CHEVALIER, J. & MONTANARO, L. 2012. Mechanical properties of porous ceramics in compression: On the transition between elastic, brittle, and cellular behavior. *Journal of the European Ceramic Society,* 32**,** 3959-3967.

MÉNDEZ-ROMÁN, R. & CARDONA-MARTINEZ, N. 1998. Relationship between the formation of surface species and catalyst deactivation during the gas-phase photocatalytic oxidation of toluene. *Catalysis Today,* 40**,** 353-365.

MIESSLER, G. L., FISCHER, P. J. & TARR, D. A. 2014. *Inorganic chemistry*, Boston, Pearson.

MILLS, A., HILL, C. & ROBERTSON, P. K. J. 2012. Overview of the current ISO tests for photocatalytic materials. *Journal of Photochemistry & Photobiology A: Chemistry,* 237**,** 7-23.

MILLS, A. & LE HUNTE, S. 1997. An overview of semiconductor photocatalysis. *Journal of Photochemistry & Photobiology, A: Chemistry,* 108**,** 1-35.

MORALES-TORRES, S., PASTRANA-MARTÍNEZ, L. M., FIGUEIREDO, J. L., FARIA, J. L. & SILVA, A. M. T. 2012. Design of graphene-based TiO2 photocatalysts--a review. *Environmental Science And Pollution Research International,* 19**,** 3676-3687.

MORITZ, M. & GESZKE-MORITZ, M. 2013. The newest achievements in synthesis, immobilization and practical applications of antibacterial nanoparticles. *Chemical Engineering Journal,* 228**,** 596-613.

MURATA, Y., TAWARA, H., OBATA, H. & TAKEUCHI, K. 1999. Air Purifying Pavement: Development of Photocatalytic Concrete Blocks. *Journal of Advanced Oxidation Technologies,* 4**,** 227-230.

NETHRAVATHI, C. & RAJAMATHI, M. 2008. Chemically modified graphene sheets produced by the solvothermal reduction of colloidal dispersions of graphite oxide. *Carbon,* 46**,** 1994-1998.

NEWMAN, J. & OWENS, P. 2003. *Properties of lightweight concrete*.

NGUYEN-PHAN, T.-D., PHAM, V. H., SHIN, E. W., PHAM, H.-D., KIM, S., CHUNG, J. S., KIM, E. J. & HUR, S. H. 2011. The role of graphene oxide content on the adsorption-enhanced photocatalysis of titanium

dioxide/graphene oxide composites. *Chemical Engineering Journal*, 170**,** 226-232.

NICHOLS, G., BYARD, S., BLOXHAM, M. J., BOTTERILL, J., DAWSON, N. J., DENNIS, A., DIART, V., NORTH, N. C. & SHERWOOD, J. D. 2002. A review of the terms agglomerate and aggregate with a recommendation for nomenclature used in powder and particle characterization. *Journal of Pharmaceutical Sciences,* 91**,** 2103-2109.

OBEE, T. N. & HAY, S. O. 1997. Effects of Moisture and Temperature on the Photooxidation of Ethylene on Titania. *Environmental Science & Technology,* 31**,** 2034-2038.

OHAMA, Y. & VAN GEMERT, D. 2011. *Applications of Titanium Dioxide Photocatalysis to Construction Materials. [electronic resource] : State-of-the-Art Report of the RILEM Technical Committee 194-TDP*, Dordrecht : Springer Science+Business Media B.V., 2011.

OHNO, T., SARUKAWA, K., TOKIEDA, K. & MATSUMURA, M. 2001. Morphology of a TiO_2 Photocatalyst (Degussa, P-25) Consisting of Anatase and Rutile Crystalline Phases. *Journal of Catalysis,* 203**,** 82.

PARKER, C. D. 1945. THE CORROSION OF CONCRETE. *Australian Journal Of Experimental Biology And Medical Science,* 23**,** 81.

PASTRANA-MARTÍNEZ, L. M., MORALES-TORRES, S., LIKODIMOS, V., FIGUEIREDO, J. L., FARIA, J. L., FALARAS, P. & SILVA, A. M. T. 2012. Advanced nanostructured photocatalysts based on reduced graphene oxide–TiO2 composites for degradation of diphenhydramine pharmaceutical and methyl orange dye. *Applied Catalysis B: Environmental,* 123-124**,** 241-256.

PENG, Z., NI, J., ZHENG, K., SHEN, Y., WANG, X., HE, G., JIN, S. & TANG, T. 2013. Dual effects and mechanism of TiO(2) nanotube arrays in reducing bacterial colonization and enhancing C3H10T1/2 cell adhesion. *International Journal of Nanomedicine,* 8**,** 3093-3105.

PÉREZ-NICOLÁS, M., BALBUENA, J., CRUZ-YUSTA, M., SÁNCHEZ, L., NAVARRO-BLASCO, I., FERNÁNDEZ, J. M. & ALVAREZ, J. I. 2015. Photocatalytic NO_X abatement by calcium aluminate cements modified with TiO_2: Improved NO_2 conversion. *Cement and Concrete Research,* 70**,** 67-76.

PESTANA, C. J., EDWARDS, C., PRABHU, R., ROBERTSON, P. K. J. & LAWTON, L. A. 2015. Photocatalytic degradation of eleven microcystin variants and nodularin by TiO2 coated glass microspheres. *Journal Of Hazardous Materials,* 300**,** 347-353.

POON, C. S. & CHEUNG, E. 2007. NO removal efficiency of photocatalytic paving blocks prepared with recycled materials. *Construction and Building Materials,* 21**,** 1746-1753.

RACHEL, A., SUBRAHMANYAM, M. & BOULE, P. 2002. Comparison of photocatalytic efficiencies of TiO_2 in suspended and immobilised form for the photocatalytic degradation of nitrobenzenesulfonic acids. *Applied Catalysis B, Environmental,* 37**,** 301-308.

RAMIREZ, A. M., DEMEESTERE, K., DE BELIE, N., MÄNTYLÄ, T. & LEVÄNEN, E. 2010. Titanium dioxide coated cementitious materials for air purifying purposes: Preparation, characterization and toluene removal potential. *Building and Environment,* 45**,** 832-838.

RASTOGI, M. & VAISH, R. 2016. Visible light induced water detoxification through Portland cement composites reinforced with photocatalytic filler: A leap away from TiO2. *Construction and Building Materials,* 120**,** 364-372.

REARDON, C. L., DOHNALKOVA, A. C., NACHIMUTHU, P., KENNEDY, D. W., AREY, B. W., SHI, L., WANG, Z., MOORE, D., MCLEAN, J. S., MARSHALL, M. J., ZACHARA, J. M., FREDRICKSON, J. K., BELIAEV, A. S., SAFFARINI, D. A. & MOYLES, D. 2010. Role of outer-membrane cytochromes MtrC and OmcA in the biomineralization of ferrihydrite by Shewanella oneidensis MR-1. *Geobiology,* 8**,** 56-68.

RIVEIRO, A., MAÇON, A. L. B., DEL VAL, J., COMESAÑA, R. & POU, J. 2018. Laser Surface Texturing of Polymers for Biomedical Applications. *Frontiers in Physics,* 6.

RIVERA, V. A. G., LEDEMI, Y., PEREIRA-DA-SILVA, M. A., MESSADDEQ, Y. & MAREGA JR, E. 2016. Plasmon-photon conversion to near-infrared emission from Yb3+: (Au/Ag-nanoparticles) in tungsten-tellurite glasses. *Scientific Reports,* 6**,** 18464.

RUDOLPH, C. V. 1980. Calculations of U-Values of Hollow Concrete Masonry. *Concrete International,* 2.

RUOT, B., PLASSAIS, A., OLIVE, F., GUILLOT, L. & BONAFOUS, L. 2009. TiO_2-containing cement pastes and mortars: Measurements of the photocatalytic efficiency using a rhodamine B-based colourimetric test. *Solar Energy,* 83**,** 1794-1801.

SAKKA, S. 2013. Chapter 11.1.2 - Sol–Gel Process and Applications. *In:* SOMIYA, S. (ed.) *Handbook of Advanced Ceramics (Second Edition)*. Oxford: Academic Press.

SAKTHIVEL, S. & KISCH, H. 2003. Daylight photocatalysis by carbon-modified titanium dioxide. *Angewandte Chemie (International Ed. In English),* 42**,** 4908-4911.

SAUER, M. L. & OLLIS, D. F. 1996. Catalyst Deactivation in Gas–Solid Photocatalysis. *Journal of Catalysis,* 163**,** 215-217.

SCHAKENRAAD, J. M., BUSSCHER, H. J., WILDEVUUR, C. R. H. & ARENDS, J. 1986. The influence of substratum surface free energy on growth and spreading of human fibroblasts in the presence and absence of serum proteins. *Journal of Biomedical Materials Research,* 20**,** 773-784.

SI, Y. & SAMULSKI, E. T. 2008. Synthesis of water soluble graphene. *Nano Letters,* 8**,** 1679-1682.

SIKORA, P., CENDROWSKI, K., MARKOWSKA-SZCZUPAK, A., HORSZCZARUK, E. & MIJOWSKA, E. 2017. The effects of silica/titania nanocomposite on the mechanical and bactericidal properties of cement mortars. *Construction and Building Materials,* 150**,** 738-746.

SIMONSEN, M. E. 2014. Chapter 4 - Heterogeneous Photocatalysis. *In:* SØGAARD, E. G. (ed.) *Chemistry of Advanced Environmental Purification Processes of Water*. Amsterdam: Elsevier.

SIMONSEN, M. E., MUFF, J., BENNEDSEN, L. R., KOWALSKI, K. P. & SØGAARD, E. G. 2010. Photocatalytic bleaching of p-nitrosodimethylaniline and a comparison to the performance of other AOP technologies. *Journal of Photochemistry and Photobiology A: Chemistry,* 216**,** 244-249.

SINGH, V. P., SANDEEP, K., KUSHWAHA, H. S., POWAR, S. & VAISH, R. 2018. Photocatalytic, hydrophobic and antimicrobial characteristics of ZnO nano needle embedded cement composites. *Construction and Building Materials,* 158**,** 285-294.

STRINI, A., CASSESE, S. & SCHIAVI, L. 2005. Measurement of benzene, toluene, ethylbenzene and o-xylene gas phase photodegradation by titanium dioxide dispersed in cementitious materials using a mixed flow reactor. *Applied Catalysis B, Environmental,* 61**,** 90-97.

SUCHANEK, W. L. & RIMAN, R. E. 2006. Hydrothermal Synthesis of Advanced Ceramic Powders. *Advances in Science and Technology,* 45**,** 184-193.

SUGRAÑEZ, R., ÁLVAREZ, J. I., CRUZ-YUSTA, M., MÁRMOL, I., MORALES, J., VILA, J. & SÁNCHEZ, L. 2013. Enhanced photocatalytic degradation of NOx gases by regulating the microstructure of mortar cement modified with titanium dioxide. *Building and Environment,* 69**,** 55-63.

TORGAL, F. P. 2013. *Nanotechnology in eco-efficient construction*, Cambridge, UK ; Philadelphia, PA : Woodhead Publishing, c2013.

UMEBAYASHI, T., YAMAKI, T., ITOH, H. & ASAI, K. 2002. Analysis of electronic structures of 3d transition metal-doped TiO2 based on band calculations. *Journal of Physics and Chemistry of Solids,* 63**,** 1909-1920.

VALLEJO, W., DIAZ-URIBE, C. & CANTILLO, Á. 2015. Methylene blue photocatalytic degradation under visible irradiation on TiO2 thin films sensitized with Cu and Zn tetracarboxy-phthalocyanines. *Journal of Photochemistry and Photobiology A: Chemistry,* 299**,** 80-86.

VINODGOPAL, K., HUA, X., DAHLGREN, R. L., LAPPIN, A. G., PATTERSON, L. K. & KAMAT, P. V. 1995. Photochemistry of Ru(bpy){sub 2}(dcbpy){sup 2+} on Al{sub 2}O{sub 3} and TiO{sub 2} surfaces. An insight into the mechanism of photosensitization. *Journal of Physical Chemistry***,** 10883.

WAGNER, V. E. & IGLEWSKI, B. H. 2008. P. aeruginosa biofilms in CF infection. *Clinical Reviews in Allergy and Immunology,* 35**,** 124-134.

WANG, F. & ZHANG, K. 2011. Reduced graphene oxide–TiO2 nanocomposite with high photocatalystic activity for the degradation of rhodamine B. *Journal of Molecular Catalysis. A, Chemical,* 345**,** 101-107.

WANG, J.-Y., ZHANG, M.-H., LI, W., CHIA, K.-S. & LIEW, R. J. Y. 2012. Stability of cenospheres in lightweight cement composites in terms of alkali–silica reaction. *Cement and Concrete Research,* 42**,** 721-727.

WANG, M.-R., JIA, D.-C., HE, P.-G. & ZHOU, Y. 2011. Microstructural and mechanical characterization of fly ash cenosphere/metakaolin-based geopolymeric composites. *Ceramics International,* 37**,** 1661-1666.

WANG, S. & LI, V. C. 2003. Lightweight engineered cementitious composites (ECC). *RILEM workshop on high performance fiber reinforced cement composites (HPFRCC 4).* Ann Arbor, USA.

WANG, Z., LIU, C., WANG, X., MARSHALL, M. J., ZACHARA, J. M., ROSSO, K. M., DUPUIS, M., FREDRICKSON, J. K., SHI, L. & HEALD, S. 2008. Kinetics of reduction of Fe(III) complexes by outer membrane cytochromes MtrC and OmcA of Shewanella oneidensis MR-1. *Applied and Environmental Microbiology,* 74**,** 6746-6755.

WHO. 2017. The cost of a polluted environment: 1.7 million child deaths a year, says WHO. Available: http://www.who.int/mediacentre/news/releases/2017/pollution-child-death/en/.

XIA, C., XU, Z., YU, J., SUN, Y. & JING, W. 2018. Fabrication of microporous GO-TiO2 membrane via an improved weak alkaline sol–gel method. *Journal of Membrane Science,* 561**,** 10-18.

XIANG, Q., YU, J. & WONG, P. K. 2011. Quantitative characterization of hydroxyl radicals produced by various photocatalysts. *Journal of Colloid and Interface Science,* 357**,** 163-167.

XIAO, Q. & OUYANG, L. 2009. Photocatalytic activity and hydroxyl radical formation of carbon-doped TiO2 nanocrystalline: Effect of calcination temperature. *Chemical Engineering Journal,* 148**,** 248-253.

XIAOBO, C. & MAO, S. S. 2007. Titanium dioxide nanomaterials: Synthesis, properties, modifications, and applications. *Chemical Reviews***,** 2891.

YANG, E.-H., GARCEZ, E. O. & LI, V. C. 2014. Micromechanics-Based Optimization of Pigmentable Strain-Hardening Cementitious Composites. *Journal of Materials in Civil Engineering,* 26**,** 04014017.

YANG, L., HAAGENSEN, J. A. J., JELSBAK, L., JOHANSEN, H. K., STERNBERG, C., HØIBY, N. & MOLIN, S. 2008. In situ growth rates and biofilm development of Pseudomonas aeruginosa populations in chronic lung infections. *Journal of Bacteriology*. Washington; USA: American Society for Microbiology (ASM).

YANG, L., WANG, F., SHU, C., LIU, P., ZHANG, W. & HU, S. 2017. TiO2/porous cementitious composites: Influences of porosities and TiO2 loading levels on photocatalytic degradation of gaseous benzene. *Construction and Building Materials,* 150**,** 774-780.

YOUSEFI, A., ALLAHVERDI, A. & HEJAZI, P. 2013. Effective dispersion of nano-TiO_2 powder for enhancement of photocatalytic properties in cement mixes. *Construction and Building Materials,* 41**,** 224-230.

YU, Q. L., HENDRIX, Y., LORENCIK, S. & BROUWERS, H. J. H. 2018. Field study of NOx degradation by a mineral-based air purifying paint. *Building and Environment,* 142**,** 70-82.

ZANG, L., QU, P., ZHAO, J., SHEN, T. & HIDAKA, H. 1997. Photocatalytic bleaching of p-nitrosodimethylaniline in TiO2 aqueous suspensions: A kinetic treatment involving some primary events photoinduced on the particle surface. *Journal of Molecular Catalysis A: Chemical,* 120**,** 235-245.

ZHANG, H., LV, X., LI, Y., WANG, Y. & LI, J. 2010a. P25-graphene composite as a high performance photocatalyst. *ACS Nano,* 4**,** 380-386.

ZHANG, J., PAN, C., FANG, P., WEI, J. & XIONG, R. 2010b. Mo + C Codoped TiO2 Using Thermal Oxidation for Enhancing Photocatalytic Activity. *ACS Applied Materials & Interfaces,* 2**,** 1173-1176.

ZHANG, Q. & LI, V. C. 2015. Development of durable spray-applied fire-resistive Engineered Cementitious Composites (SFR-ECC). *Cement and Concrete Composites,* 60**,** 10-16.

ZHANG, Y. & PAN, C. 2011. TiO_2/graphene composite from thermal reaction of graphene oxide and its photocatalytic activity in visible light. *JOURNAL OF MATERIALS SCIENCE,* 46**,** 2622-2626.

ZHAO, A., YANG, J. & YANG, E.-H. 2015. Self-cleaning engineered cementitious composites. *Cement and Concrete Composites,* 64**,** 74-83.

ZHU, W., BARTOS, P. & PORRO, A. 2004. Application of nanotechnology in construction. Summary of a state-of-the-art report. *MATERIALS AND STRUCTURES*, 37**,** 649-658.

ZIMBONE, M., BUCCHERI, M. A., CACCIATO, G., SANZ, R., RAPPAZZO, G., BONINELLI, S., REITANO, R., ROMANO, L., PRIVITERA, V. & GRIMALDI, M. G. 2015. Photocatalytical and antibacterial activity of TiO2 nanoparticles obtained by laser ablation in water. *Applied Catalysis B-Environmental*, 165**,** 487-494.

ZOUZELKA, R. & RATHOUSKY, J. 2017. Photocatalytic abatement of NOx pollutants in the air using commercial functional coating with porous morphology. *Applied Catalysis B: Environmental*, 217**,** 466-476.